

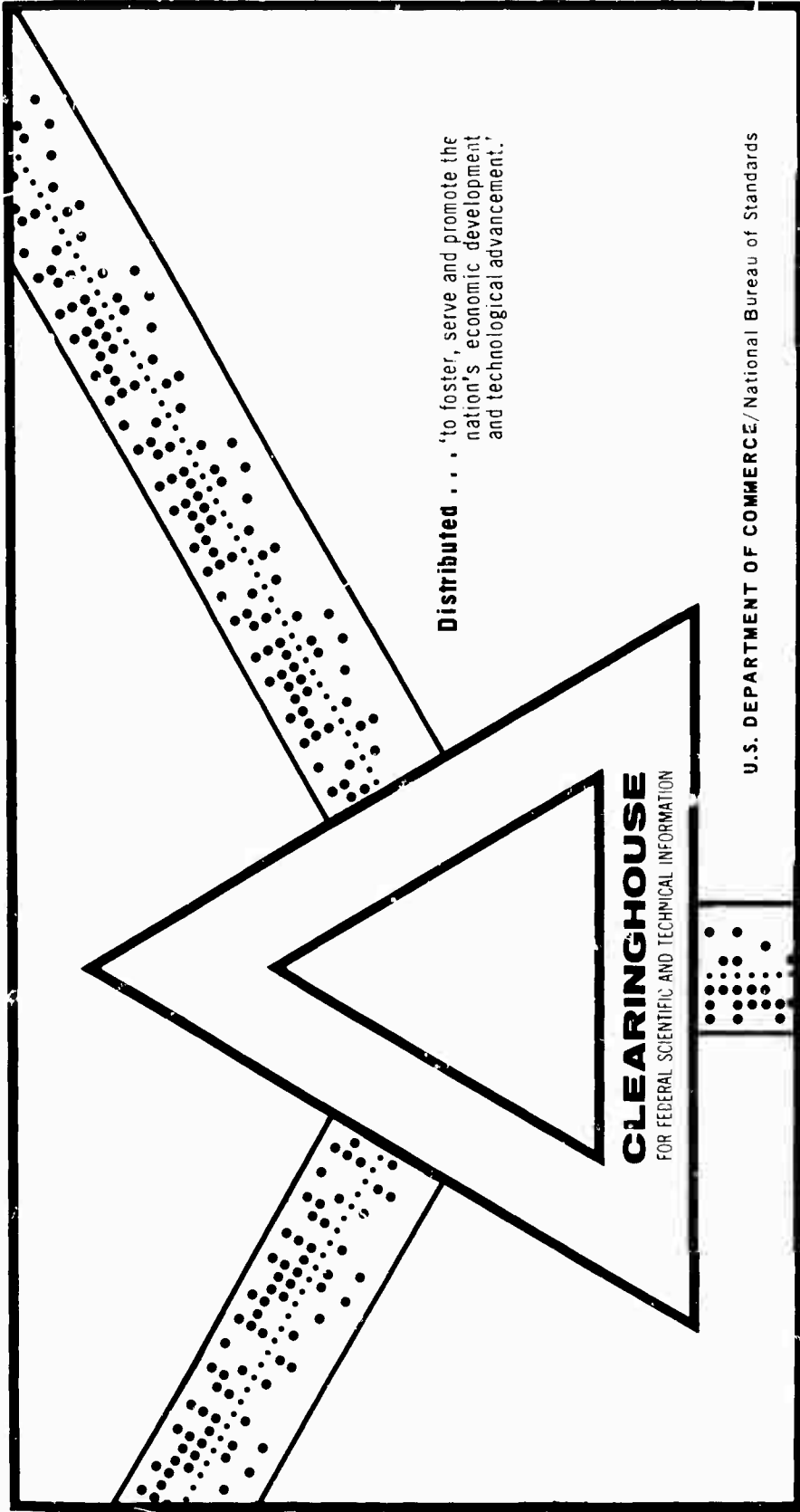
AD 702 693

INTERGRANULAR FRACTURE IN AN A1-15 WT. % Zn ALLOY

William J. Kovacs, et al

Carnegie-Mellon University
Pittsburgh, Pennsylvania

February 1970



U.S. DEPARTMENT OF COMMERCE/National Bureau of Standards

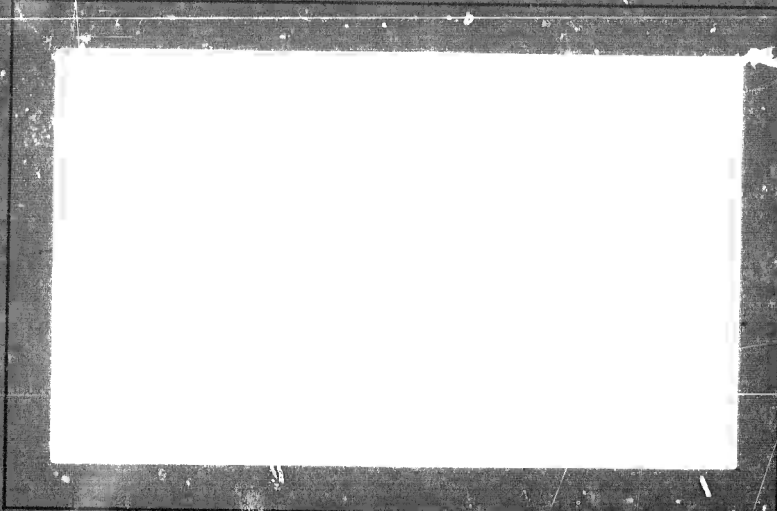
This document has been approved for public release and sale.

DISCLAIMER NOTICE

THIS DOCUMENT IS THE BEST
QUALITY AVAILABLE.

COPY FURNISHED CONTAINED
A SIGNIFICANT NUMBER OF
PAGES WHICH DO NOT
REPRODUCE LEGIBLY.

AD202693



METALS RESEARCH LABORATORY
CARNEGIE INSTITUTE OF TECHNOLOGY

Carnegie -Mellon University



PITTSBURGH, PENNSYLVANIA

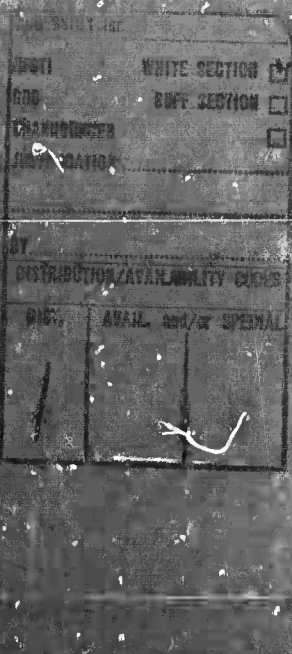
Reproduced by the
CLEARINGHOUSE
for Federal Scientific & Technical
Information Springfield Va. 22151

This document has been approved
for public release and its
distribution is unlimited



3

132



Intergranular Fracture in an
Al-15 wt. % Zn Alloy

by
W. J. Kovacs* and J. R. Low, Jr.

Metallurgy & Materials Science
Carnegie-Mellon University
Pittsburgh, Pennsylvania 15213

February 1970

(To be submitted in part for publication)

* Presently at: Kawecki Berylco Industries, Inc., Research Laboratory,
Reading, Pennsylvania

This research was supported by the Advanced Research Project Agency,
Order #878, Department of Defense under Nonr-760(31).
Distribution of this document is unlimited and reproduction in whole or
in part is permitted for any purpose of the U. S. Government.

TABLE OF CONTENTS

	<u>Page Number</u>
Dedication	i
Acknowledgments	i
List of Figures	ii
Abstract	viii
INTRODUCTION.....	1
I. ENVIRONMENTAL EFFECTS ON THE FRACTURE OF MATERIALS.....	3
A. Brittle Crack Nucleation Fracture: Cleavage & Inter-granular.....	4
B. Crack Propagation.....	7
C. Liquid Metal Embrittlement.....	9
D. Complex-Ion Embrittlement.....	11
E. Stress Corrosion Cracking (SCC) of Precipitation Hardened Aluminum Alloys.....	13
II. EXPERIMENTAL PROCEDURES.....	18
A. Experimental Material.....	18
B. Specimen Preparation.....	19
1. Polycrystal Specimens.....	19
2. Bi-crystal Specimens.....	20
C. Thermal History.....	21
D. Transmission Electron Microscopy.....	22
E. Bi-crystal Orientations.....	22
F. Testing Procedure for Double Cantilever Beam (DCB) Geometry.....	23
G. Measurement of Crack Extension & Load Relaxation.....	26
H. Supplementary Test Procedures.....	27
III. THEORY.....	29
A. Experimental Techniques Used to Measure Stress Intensity Factor & Elastic Strain Energy Release Rate.....	29
B. The Equations Used to Calculate Elastic Strain Energy Released (G) and Stress Intensity Factor (K).....	35
1. Elastic Strain Energy Released (G) During Crack Propagation.....	36
2. Relation Between Elastic Strain Energy Release Rate (G) and Stress Intensity Factor (K).....	39
(i) (Stress Intensity Factor K).....	40
(ii) (Griffith Analysis Describing Fracture Instability).....	41
(iii) (The Dependence of K on G).....	42
C. Effect of Slide Grooves In Promoting Strain.....	43
D. Stress Analysis of DCB Geometry.....	45
IV. DATA.....	49
A. Raw Data.....	49
B. Reduced Data.....	50
1. Polycrystal Data.....	50
2. Bi-crystal Data.....	53
C. Bi-crystal Orientations.....	54
D. Source of Error.....	55

<u>Table of Contents (Cont'd)</u>		<u>Page Number</u>
V.	RESULTS.....	57
A.	Plane Strain DCB Test Geometry.....	57
B.	Slow Crack Growth In Air, Distilled H_2O , and 0.5 Molar NaCl.....	62
C.	The Influence of Microstructure on "Threshold-Toughness" K_{Ic} ($V = 0$).....	65
D.	The Influence of Microstructure on Stress Corrosion Cracking Susceptibility.....	67
E.	A Comparison of the Cracking Kinetics Between Intergranular Fracture in Air and in 0.5M NaCl.....	69
F.	Corrosion in the Absence of Stress.....	70
G.	The Dependence of Stress Corrosion Cracking Susceptibility on Bi-crystal Orientation.....	71
H.	A Comparison of Bi-crystal to Polycrystal Susceptibility in 0.5M NaCl.....	74
VI.	DISCUSSION OF RESULTS.....	76
A.	Physical Metallurgy of the Al-Zn System.....	76
B.	Metallographic Observations.....	78
C.	Surface Topograph of Intergranular Fracture In Air and In 0.5M NaCl.....	81
1.	Faceting.....	82
2.	Slip Line Patterns.....	84
3.	Stress Corrosion Pitting.....	87
D.	Movement of Crack Front During Fracture.....	88
E.	Influence of Microstructure on the Slip Band Structure.....	89
F.	Interpretation of Dependence of Fracture Toughness on Microstructure.....	93
G.	Interpretation of the Dependence of Stress-Corrosion Cracking Susceptibility on Microstructure.....	96
H.	Bi-crystal Susceptibility to Stress-Corrosion Cracking.....	101
VII.	THEORETICAL FORMALISM FOR INTERGRANULAR FRACTURE IN AIR & IN A CORROSIVE ENVIRONMENT.....	107
A.	Introduction.....	107
B.	Crack Initiation In Air.....	109
1.	Description of σ_{yy} Time Dependent.....	110
C.	Time Dependence of Dislocation Pile-Ups.....	114
D.	Crack Propagation.....	115
E.	Theoretical Simulation of Intergranular Fracture In Air.....	117
F.	Application of Formalism to Intergranular Fracture In a Corrosive Environment.....	120
G.	Summary.....	121
(i)	Stress State & Intergranular Cracking Kinetics	122
(ii)	Microstructural Affects on Intergranular Fracture.....	122
(iii)	Galvanic Attack.....	123
(iv)	The Affects of Grain Boundary Orientation on Intergranular Fracture.....	123
(v)	Theoretical Formalism for Intergranular Fracture in Air and in a Corrosive Environment....	123

Table of Contents (Cont'd)

Page Number

General Bibliography.....	124
Appendix I-A	Tables 1 thru 30
Appendix I-B	Polycrystal Specimens 1 thru 13
Appendix I-C	Bi-crystal Data
Appendix I-D	Sample Calculations
Appendix II-A	Time Dependent Slip Blockage
Appendix II-B	Material & Microstructural Constants Used in Computer Program to Simulate Intergranular Fracture In Air.

Dedication

The author dedicates this work to the Woman's Auxiliary to the American Institute of Mining, Metallurgical and Petroleum Engineers, Incorporated. A particular debt of gratitude is due Mr. and Mrs. R. Rowen and Mrs. I. Kissock who expressed an initial interest in the author and supported his request for scholarship aid during undergraduate study.

Acknowledgments

The author is obligated and grateful to Professor Jack Low Jr. for his continuous guidance through most of the author's graduate study. Also, a debt of gratitude is due Dr. G. Groves for his encouragement and help during the initial phases of this investigation.

The author also wishes to thank Professors R. W. Dunlap, H. R. Piehler, and R. D. Townsend for an interest in this work followed by critical discussions and Messrs. G. G. Biddle, E. L. Fraticelli, and A. M. Walan for their help in constructing equipment. Thanks are also due many of the author's fellow graduate students, amongst them, Messers. S. Lewis, A. DeArdo, C. Smith, A. Stavros, R. Sun, for their fellowship and stimulating discussions on various phases of this investigation. Sincere appreciation is extended to Mr. Francis J. Samuels for his patience and time in typing and editing the thesis draft and final copy.

List of Figures

<u>Figure No.</u>	<u>Caption</u>	<u>Page No.</u>
1.	Cleavage microcracks nucleated at slip bands blocked by the grain boundary in a MgO bi-crystal (Johnston, Stokes, and Li ⁽⁶²⁾).	6A
2.	Polarized transmitted light photomicrograph of MgO bi-crystal showing stress concentrations at ends of slip bands, 78X (Johnston and Parker ⁽⁶⁸⁾).	6B
3.	Polycrystalline silver chloride deformed in 6N sodium chloride solution presaturated with AgCl_4^{3-} complexes; strain increasing progressively from sections (a) to (e): note that cracks are initiated only where slip bands are arrested at the grain boundary. The last three sections (c), (d), and (e) show microcracks combining and forming a continuous intergranular fracture path. (Westwood ⁽⁸⁵⁾).	12A
4.	Polycrystal DCB specimen loaded up to a fixed-deflection δ for a force F and an initial crack length L ; the side-groove depth, $(W-B)/2$, promotes a plane strain stress state and confines intergranular crack advance to the mid-beam height H .	19A
5.	Bi-crystal DCB specimen loaded up to a fixed-deflection δ for a force F and an initial crack length L ; the grain boundary at the mid-beam height H is the intergranular fracture path.	20A
6.	Schematic drawing showing solution anneal at 540°C followed by a direct quench to 155°C; progressive aging at 155°C is followed by a direct quench to room temperature (25°C) and aging at 25°C for different times.	22A
7.	Elastic stress distribution at the base of a stationary crack; Part A is the resulting stress distribution due to Irwin ⁽³⁾ , Part B shows the first term in a series solution for the stress distribution (different coordinate system than Part A) due to Williams ⁽⁹⁾ .	33A

<u>Figure No.</u>	<u>Caption</u>	<u>Page No.</u>
8.	Incremental elastic strain energy released, dU , for crack extension, dL , under fixed-grip conditions or at a constant deflection, δ .	37A
9.	Energy criterion for crack instability showing a crack length L^* which can propagate with a decrease in energy.	42A
10.	The effect of side-grooves in promoting plane strain across crack front B, i.e. superposition of the plane stress states in the x-y and y-z planes.	45A
11.	Yield strength versus aging time at 155°C prior to a quench and further age at room temperature, 25°C, for 2 hrs, 20 hrs and 100 hrs; the micro-structures tested are labeled in Roman Numerals.	49A
12.	Yield strength versus aging at room temperature, 25°C, following an aging treatment at 155°C for different times; 50 min., 500 min., and 5000 min.	49B
13.	Load relaxation F versus crack length L during crack propagation in DCB specimen No. 7 polycrystal.	51A
14.	Crack length L versus cracking time t for crack propagation in DCB specimen No. 7 polycrystal.	51B
15.	Specifying bi-crystal orientation with five angles; $\alpha_{100}, \beta_{100}, \gamma_{111}, \epsilon, \Delta$.	55A
16.	Fracture toughness G versus depth of side groove (B/W) for a commercial Al-5.6% Zn - 2.3% Mg alloy; plane strain fracture toughness is ≈ 50 lbs/in.	57A
17.	Crack velocity for intergranular fracture in air versus apparent plane strain stress intensity factory; three side-groove geometries, i.e. $B/W = .33, .52, .62$, are plotted with the transition point for plane strain at $B/W \approx .52$.	58A

<u>Figure No.</u>	<u>Caption</u>	<u>Page No.</u>
18.	Crack velocity versus stress intensity factor for intergranular fracture in stress environments (Air, Distilled H_2O , and .5M NaCl); all points in this figure are for Microstructure No. I, age 50 min. at 155°C prior to a 100 hr. age at room temperature.	63A
19.	Crack velocity versus the square of the stress intensity factor for intergranular fracture in Air, Distilled H_2O , and .5M NaCl; test Microstructure, No. I, for each environment is held constant.	64A
20.	Crack velocity versus stress intensity factor for intergranular fracture in air; Microstructures: No. I polycrystal, aged 50 min. at 155°C prior to 100 hr age at room temperature and No. III polycrystal aged 15 min. at 155°C prior to 100 hr. age at room temperature.	65A
21.	Crack velocity versus stress intensity factor for intergranular fracture in air; Microstructure No. 9 polycrystal, aged 500 min. at 155°C prior to 100 hrs. age at room temperature.	66A
22.	Crack velocity versus stress intensity factor for intergranular fracture in 0.5M NaCl; Four test microstructures: (see section VI.A for full description of Microstructures Nos. I, II, III, and IV corresponding to polycrystal tests in this figure).	67A
23.	10,000X. Two stage carbon-platinum replica of a corrosion surface; shadowing angle of approximately 45° shows the extent of localized pitting at zinc precipitates.	71A
24.	Average crack velocity versus average elastic strain energy released for intergranular fracture of bi-crystals in 0.5M NaCl; all bi-crystals tested have the same microstructure (50 min. age at 155°C prior to a 100 hr. age at room temperature.	72A
25.	Stereographic projection of bi-crystal No. 31 in Region C of Fig. (24), with four coincident sets of slip systems: highly resistant to intergranular fracture in 0.5M NaCl.	73A

<u>Figure No.</u>	<u>Caption</u>	<u>Page No.</u>
26.	Stereographic projection of bi-crystal No. 32 in Region B of Fig. (21), with two coincident sets of slip systems; slightly less resistant to intergranular fracture than No. 31 bi-crystal.	73B
27.	Stereographic projection of bi-crystal No. 4 in Region A of Fig. (24), with no coincident sets of slip systems; highly susceptible to intergranular fracture in 0.5M NaCl.	73C
28.	Top view of DCB No. 7 polycrystal fracture surface; equi-axed intergranular fracture surface. Profile view of intergranular fracture in DCB specimen; total crack length is approximately 1.35 times measured crack length.	74A
29.	Part A: 22,000X, Microstructure No. I showing α' Zn precipitate at grain boundary and not at dislocations. Part B: 60,000X, Microstructure No. I showing G.P. zones in the matrix.	78A
30.	Part A: 60,000X, Microstructure No. II showing α' Zn precipitate at dislocations. Part B: 48,000X, Microstructure No. III showing α' Zn precipitate at dislocations.	79A
31.	40,000X, Microstructure No. II showing extent of Zn precipitate at grain boundary.	79B
32.	400X, No. 2 bi-crystal fracture surface showing facets (step-like appearance), slip traces on facets (fine striations), and localized pitting at Zn precipitate; Fracture on 0.5M NaCl for Microstructure No. I.	82A
33.	1000X, profile view of grain boundary on bi-crystal surface prior to fracture; remnants of serrated grain boundary profile are present after electropolishing preferential attacked the boundary.	82B
34.	Part A: 450X, three distinct slip trace patterns on No. 3 bi-crystal fracture surface; Microstructure No. I fractured in 0.5M NaCl. Part B: 1000X, blow up of Part A showing planar slip band spacing of approximately .1 to 1μ .	84A

<u>Figure No.</u>	<u>Caption</u>	<u>Page No.</u>
35.	Matching up traces on No. 3 bi-crystal fracture surface with {111} slip planes for the known orientation of the bi-crystal.	84B
36.	Part A: 450X, Fracture surface of No. 5 polycrystal tested in 0.5M NaCl; Microstructure No. I shows planar slip and pitting. Part B: 1100X, blow-up of Part A showing localized attack at Zn precipitate.	85A
37.	Part A: 275X, Fracture surface of No. 7 polycrystal tested in air; Microstructure No. II shows fine-wavy slip. Part B: 1100X, blow-up of Part A showing details of wavy slip.	86A
38.	300X, slip traces for Microstructure No. III shown on the polished surface of a bi-crystal deformed in air; wavy slip lines.	86B
39.	Load relaxation trace of a bi-crystal DCB specimen tested in 0.5M NaCl; the trace shows the periodic occurrence of horizontal steps, i.e., $dF/dt \approx 0$.	88A
40.	Load relaxation trace of a polycrystal DCB specimen tested in air; the trace shows irregular changes in the slope, dF/dt , attributed to the equi-axed grain size of the test specimens.	89A
41.	450X, polished bi-crystal surface for Microstructure No. I showing planar slip coincidence across grain boundary; one set of slip systems {111} planes and <110> directions in each grain adjacent to the grain boundary are parallel.	101A
42.	Schematic drawing showing the total normal stress across a fracture plane ahead of a macroscopic crack.	110A
43.	Stroh's model showing the normal tensile stress concentration ahead of a blocked slip band.	111A

<u>Figure No.</u>	<u>Caption</u>	<u>Page No.</u>
44.	Superposition of a static stress state, i.e. at the crack tip, and a time dependent stress state, i.e. at the blocked slip band, over a distance S .	116A
45.	Crack velocity for intergranular fracture in air versus stress intensity factor; for No. 3 polycrystal and for assumed values S , τ_o' , V_o' , and m .	117A

CARNEGIE-MELLON UNIVERSITY

Intergranular Fracture in an Al-15 wt % Zn Alloy

William J. Kovacs

Abstract

Cracking kinetics involved in the intergranular fracture of an Al-15 wt % Zn alloy tested in air, distilled H_2O , and 0.5M NaCl have been studied by means of the elastic strain energy released during crack propagation in a double cantilever beam specimen. This technique has been applied to two different types of specimens: polycrystals with equi-axed grains and bi-crystals with crack propagation confined to the grain boundary. By varying the microstructure through selective aging treatments, a wide range of cracking susceptibility has been observed.

The results show that the fracture toughness of this alloy increases with a decreasing volume fraction of G.P. zones in the matrix. A similar trend in the stress corrosion cracking tests in 0.5M NaCl is noted, and the susceptibility to fracture increases as the volume fraction of G.P. zones in the matrix increases. The microstructure highly susceptible to fracture exhibits planar slip traces while the more resistant microstructures show a dispersed type surface slip pattern. The dependence of cracking rates on the microstructure is explained in terms of inhomogeneous plastic flow in the matrix being blocked by grain boundaries and leading to severe stress concentrations at the boundaries. The bi-crystal tests substantiate these results and show that orientations favoring partial continuity of slip bands across grain boundaries are less

susceptible to stress corrosion cracking than arbitrarily oriented boundaries with no slip continuity.

BLANK PAGE

Introduction

The detrimental and occasionally devastating effects of environments on the mechanical properties of many commercial materials have inspired vast numbers of investigators to probe for underlying mechanisms in hopes of gaining a measure of control of the phenomena. However, the phenomena is still far from well understood.

This thesis deals with a small aspect of this broad and important subject. In particular, the scope of this work relates to the effects of microstructure, a grain boundary orientation, and environment (i.e., air, distilled H_2O , and 0.5M NaCl) on the cracking kinetics of an Al-15 wt % Zn alloy. Emphasis has been placed on the energy requirements and the stress states necessary to cause crack extension at different velocities.

Though technologically uninteresting at present, an Al-15 wt % Zn alloy offers a number of advantages for fundamental studies into mechanism responsible for environment sensitive fracture behavior. In the first place, the microstructural variations of a wide range of alloy compositions in the Al-Zn system have been investigated. These studies describe the aging behavior (i.e., the kinetics and sequence of the formation of different phases as a function of temperature) and offer a strong base to relate microstructural affects to fracture behavior. Secondly, the Al-15 wt % Zn is highly susceptible to intergranular fracture in air over a wide range of microstructures i.e., different volume fractions of G.P. zones and zinc precipitate in the matrix.

The hope is that processes occurring in commercially important age-hardenable aluminum alloys can be controlled through the understanding

2.

obtained by basic research on more simple, but more easily studied materials such as an Al-15 wt % Zn alloy.

The objectives of this work are to determine: (i) microstructural affects on intergranular cracking kinetics (rate of crack advance) in different environments, (ii) the dependence of cracking kinetics on grain boundary orientation for intergranular fracture in 0.5M NaCl, (iii) a theoretical formalism which explains the observations in (i) and (ii). The combination of these objectives should extend the understanding of intergranular fracture processes in aluminum alloys and thus supplement our present knowledge of environment sensitive fracture.

This thesis is divided into seven major sections as follows:

I - Environment Sensitive Fracture Behavior

II - Experimental Procedures

III - Theory

IV - Data

V - Results

VI - Discussion of Results

VII - Theoretical Formalism

I. Environmental Effects on the Fracture of Materials

In this introductory section the principal microscopic observations concerning the nucleation and propagation of fracture in metal and non-metal systems will be reviewed. In addition, the affects of certain environments on the fracture behavior of crystalline materials will be discussed and particular emphasis will be placed on the stress corrosion cracking process in aluminum alloys. For the purposes of this general introduction, the more complicated phenomenon of stress corrosion cracking will be approached by first describing brittle crack nucleation in the absence of any corrosive or embrittling environment. Secondly, some mention will be made of the propagation stage as opposed to the nucleation stage in the fracture process. It is inherently assumed in the discussion on crack nucleation and propagation that the fracture process takes place under ambient conditions, i.e., room temperature and atmospheric pressure. However, to extend this review to cover environment - sensitive fracture behavior, the specific cases of liquid-metal and complex-ion embrittlement and the stress corrosion cracking of aluminum alloys will be discussed. The less complicated phenomena of liquid-metal and complex-ion embrittlement offer a gradual introduction into the more complicated electrochemical affects present in the stress corrosion fracture of metal systems.

The scope of this thesis deals with the brittle, intergranular fracture of an aluminum-zinc alloy tested in air, distilled H_2O , and 0.5M NaCl under fixed-grip conditions. Thus, this review will be directed toward the specific fracture processes which are possibly operating in the system studied. The most important generalization which results from a survey of this type is that

in all of the cases considered fracture is nucleated by plastic deformation and, because plastic deformation is inhomogeneous, on a microscopic scale. The final results and conclusions of this study on an aluminum-zinc system will bear out this basic generalization of all fracture processes.

A. Brittle Crack Nucleation Fracture: Cleavage and Intergranular

The fracture process may be considered in terms of its component processes: crack initiation and propagation. Sometimes cracks are present in the material prior to testing, for example, in cleaved magnesium oxide⁽⁶⁵⁾ or Glass⁽⁶⁶⁾, but otherwise it is generally agreed that the fracture of crystalline materials occur only after some measure of plastic deformation⁽⁶⁷⁾. In a brittle material or one of low stacking fault energy, (i.e., restricts cross slip and favors inhomogeneous plastic flow), crack initiation is considered to be the result of dislocation pile-up and coalescence⁽⁶⁷⁾ at some stable obstacle such as another array of dislocations⁽⁶⁸⁾, a twin boundary⁽⁶⁹⁾, sub-boundary⁽⁷⁰⁾, grain boundary⁽⁶²⁾, or surface film⁽⁷¹⁾.

In metals, the most detailed investigation for relating microcracks to the deformation mechanisms responsible for their nucleation, are Hull⁽⁷²⁾, Honda⁽⁷³⁾, and Tetelman⁽⁷⁴⁾ using silicon-iron single crystals, and Hornbogen⁽⁷⁵⁾ using an iron-phosphorous alloy. Hull observed crack initiation at a twin intersection for which the plane of intersection was a cleavage plane. Similarly, Honda observed crack nucleation at twin intersection; but also when the deforming mode was that of slip, microcracks were observed to form at regions where slip bands on two different systems intersected. Hornbogen inferred that the sudden formation of a twin can produce stress waves which

if reflected as a tension wave could produce cleavage cracks. Tetelman has reported the deformation patterns produced by microcracks in an Fe-3% Si single crystal. Also, he has developed a theoretical analysis to explain the slip patterns accompanying plastic deformation at the tip of a moving crack.

For non-metallic materials, the most detailed investigations of crack nucleation by slip are those of Johnston, Stokes and Li^(62,68) using MgO crystals. These studies showed that MgO crystals were brittle or ductile depending upon the slip distribution, and that cracks were nucleated at slip band intersections. If these intersections were prevented by deforming the crystal in single slip only, then ductile behavior was observed.

The above observations have been made on single crystals; however, the introduction of a grain boundary to form a bi-crystal specimen complicates the deformation and fracture processes. Generally, the interaction of slip with the grain boundary and slip compatibility across the boundary must be considered. Most of the detailed intergranular fracture studies have been performed on ionic materials because of their inherent notch sensitivity, i.e., insufficient number of slip systems to accommodate an arbitrary strain. It has been shown⁽⁷⁶⁾ that grain boundaries affect the mechanical behavior of AgCl to a degree which depends upon the mode of slip. At temperatures where cross slip becomes easier, plastic deformation occurs in a more homogeneous manner, and as a result grain boundaries are not effective obstacles to slip blockage and have only a slight influence on the flow stress. However, at temperatures where plastic deformation is confined to planar slip on {110}<110> systems, intergranular cracking invariably results. This embrittling effect of grain boundaries, when planar

slip is operative, appears to have general significance for ionic solids having the rock salt structure. It can be demonstrated in AgCl , LiF , NaCl , and MgO .

Johnston⁽⁶²⁾ has investigated the role of grain boundaries in crack nucleation by loading bi-crystals of MgO in such a way that slip bands originating in the crystal impinged on the boundary. The boundary misorientation was varied and the probability of crack nucleation at the boundary due to blocking of the slip band was found to depend on the degree of misorientation at the boundary. The loading arrangement at the grain boundary was compressive, and thus the crack was arrested in the nucleation stage without producing complete fracture.

These microcracks are seen at a number of points in Figure (1). This figure shows two distinct cleavage cracks being associated with planar slip band impingement (as outlined by etch-pits) at a grain boundary. The cleavage cracks appear to be nucleated in the second grain of the MgO bi-crystal because of stress concentrations resulting from slip band blockage at the grain boundary.

The stress concentration effect of blocked inhomogeneous plastic flow leading to micro-crack formation was first postulated by Zener⁽⁶⁷⁾ and Stroh⁽⁷⁷⁾. They predicted high tensile and shear stress concentrations ahead of a blocked slip band. The resulting stress concentrations, from slip band impingement on a grain boundary, which cause cleavage are shown in Figure (2), taken of a MgO bi-crystal with transmitted light. It is likely stress concentrations similar to those shown in Figure (2) caused the cleavage cracks apparent in Figure (1).

Presumably the crack nucleation mechanism of blocked inhomogeneous plastic flow leading to cleavage can apply to intergranular crack nucleation provided the cohesive strength of the grain boundary is less than the cleavage strength

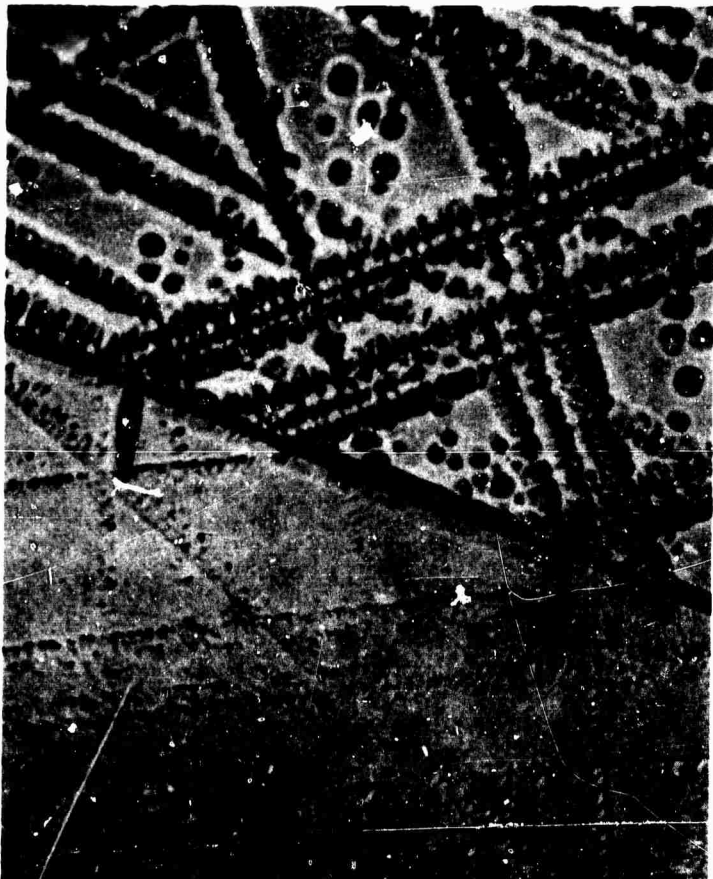


Figure 1. Cleavage microcracks nucleated at slip bands blocked by the grain boundary in a MgO Bi-crystal (Johnston, Stokes, and Li⁽⁶²⁾).



Figure 2. Polarized transmitted light photomicrograph of MgO Bi-crystal showing stress concentrations at ends of slip bands, 78X (Johnston and Parker⁽⁶⁸⁾).

of the adjacent grain.

B. Crack Propagation:

The fracture process of a crystalline material is a two stage process, and the previous discussion has been centered on crack nucleation with no consideration given to the propagation stage. However, an important step is to decide whether the critical event in the fracture process is the nucleation of a crack or its subsequent growth. For example, if the nucleation stage of fracture is assumed to be critical then once a crack has started to spread it will continue expanding until fracture is complete provided the external stress is maintained. The criterion used for deciding which stage is controlling is a comparison of whether the fracture energy for growth is greater or less than the free surface energy associated with nucleation⁽⁷⁸⁾. One way for growth to become rate controlling is if a crack is nucleated in a brittle second phase particle (presumably of a low free surface energy) and then requires a higher energy to propagate into a surrounding ductile matrix. However, if crack propagation is confined to a brittle phase, then the isolated dislocation pile-up models show^(67,77) that nucleation is the critical event provided the fracture energy for growth retains the free surface energy appropriate to the nucleation stage. Generally, the plastic flow involved in metals precludes this assumption, and a theoretical investigation by Tetelmar⁽⁷⁴⁾ has shown possible contributions to the energy for crack propagation. This investigation showed a marked dependence of the fracture energy on crack velocity, which was attributed to differences in plastic flow. This work combined with that of Hahn⁽⁷⁹⁾

suggests that there is a connection between stress sensitivity of dislocation velocity and brittle behavior: materials in which dislocation velocities are most sensitive to stress tend to be ductile and brittle behavior is related to a low stress sensitivity of dislocation velocity. Rosenfield and Hahn⁽⁸⁰⁾ have used this idea to develop a theoretical treatment for describing the effect of stress sensitivity of dislocation velocity on pile-up formation. In essence, their treatment is a kinetic one, whereas previous pile-up calculations represent equilibrium positions. Their results approach those of Eshelby⁽⁶¹⁾ as time approaches infinity (i.e., equilibrium is reached at sufficiently long times). In terms of crack nucleation, the theory calculates the time dependence of the stress concentration ahead of a blocked slip band. Thus, if crack nucleation is rate controlling, this theory offers a means for calculating cracking rates and comparing them to observed values.

In summary, the first part of this survey has been restricted to plausible explanations for crack initiation and propagation based on experimental observations mainly in ionic materials. Because of the restricted number of slip systems in ionic materials, the stress concentration resulting from blocked inhomogeneous plastic flow would be expected to be higher and more effective in causing fracture than in metallic systems with fcc or bcc slip systems. However, similar trends should be apparent between the intergranular brittle fracture of ionic and metallic systems when considering the influence of slip on the fracture process.

If the generalization holds that most fracture processes are nucleated

by inhomogeneous plastic flow then a natural foundation to expand our understanding to environment-sensitive fracture behavior is the previous discussion of the observations on cleavage crack nucleation and propagation. Since the addition of different environments complicates the fracture process, the topic of environment-sensitive fracture will be introduced by liquid-metal embrittlement. An understanding of this phenomenon offers a bridge to relate to more complicated environment induced fracture processes.

C. Liquid Metal Embrittlement:

There is no *a priori* reason why we cannot regard a specific phenomenon such as liquid metal embrittlement as one aspect of the broader problem of brittle fracture, and thereby assume that cracks are also initiated by deformation processes in the presence of the environment. This argument precludes any systems which fail without the application of a sufficient stress to cause plastic flow i.e., the intergranular penetration and failure of polycrystalline aluminum by liquid gallium⁽⁸¹⁾. Using this argument as a building block for environmental induced fracture, the characteristics which influence liquid metal embrittlement will be discussed prior to the more complicated phenomenon of stress corrosion cracking. The validity of the assumption concerning environmental induced fracture is substantiated⁽⁸²⁾ by the prerequisites for embrittlement of an otherwise ductile solid metal by an active liquid metal: (i) some plastic deformation (ii) the existence in the specimen of some stable obstacle to dislocation motion, and (iii) adsorption of the active embrittling species specifically at this obstacle, and subsequently at the propagating crack tip. However, the factors which

determine which liquid metal will actually embrittle which solid metal, and the actual mechanism of embrittlement remain unclear. Current thinking on the mechanism of embrittlement has been based on the hypothesis that embrittlement results from a localized decrease in cohesion associated with adsorption of the liquid metal⁽⁸²⁾. Unfortunately, cohesion in metals is not well understood, and it is difficult to devise experiments to evaluate such a possibility directly. However, it has been demonstrated that approximately 90 ergs/cm² is required to propagate a cleavage crack in zinc immersed in liquid nitrogen and only 50 ergs/cm² is required to propagate a similar crack at room temperature in the presence of mercury⁽⁸³⁾. The value of 90 ergs/cm² is considered to be the true surface energy of the basal plane in zinc, and this suggests a genuine reduction in the cohesive strength of the bonds across the basal plane occurs in the presence of mercury.

Generally, it appears that the susceptibility of a given metal to embrittlement by liquid metals can be significantly influenced by the number of slip systems available, and the ease with which cross slip can occur. This is exemplified in copper base solid solutions where the degree of intergranular embrittlement by mercury increased as the stacking fault energy and ease of cross slip decreased⁽³⁹⁾. This result is similar to the previous effects described on AgCl, where crack nucleation depended to a large extent on the type of slip which in turn was controlled by temperature instead of through the microstructure, or stacking fault energy. Such observations support the view that embrittlement occurs only when a significant stress concentration can be built up and

maintained in the vicinity of some obstacle to slip. Once a crack is initiated, the concentration of stress at its tip is usually sufficient to allow brittle propagation, providing the embrittling species are present in sufficient quantity and are sufficiently mobile to keep up with the propagating crack front.

In summary, two conditions are necessary for liquid-metal embrittlement to occur:

1. Blocked plastic flow.
2. A lowering of the cohesive strength along the fracture path (cleavage plane, or grain boundary).

Also it should be noted that the phenomenon of liquid metal embrittlement leading to fracture is analogous to the segregation of solute atoms to grain boundaries and the subsequent failure of the boundaries. The argument for intergranular fracture is based on the reduction of the cohesive strength of the grain boundary due to the segregated species. The real extent of this type of segregation in solids and the magnitude of the interfacial energy reduction has been reviewed by Hondros⁽⁸⁴⁾. This review shows the embrittling effects of solute or impurity segregation to interfaces for several metallic systems (i.e., Fe-P, Fe-N, Fe-Si, Fe-Cr, and Cu-Bi, Cu-Sb, Cu-Au), and the results appear to be quite general.

D. Complex-Ion Embrittlement:

Prior to a discussion of stress corrosion cracking, the last phenomena to be mentioned is the environment sensitive mechanical behavior of crystalline non-metals. Recent studies have shown that such materials can exhibit

characteristics similar to liquid metal embrittlement and stress corrosion cracking. For example, when polycrystalline AgCl is exposed to environments containing highly charged complex ions, its fracture mode changes from ductile and transcrystalline to brittle and intercrystalline⁽⁸⁵⁾. Both positively and negatively charged complexes can cause brittle behavior, and it has been found that the degree of embrittlement (i) increases with concentration of the critical complex species present in the environment (ii) increases with charge on the complex ion (iii) is a function of the distribution of charge on the complex, and (iv) for negatively charged complexes, is very sensitive to the applied stress⁽⁸⁵⁾. Metallographic studies of this phenomenon reveal interesting features representative of crack nucleation and propagation. Figure (3) demonstrates that in an embrittling environment, micro-cracks are formed in polycrystalline AgCl only where slip bands are arrested at a grain boundary, and that they propagate by joining up to form macroscopic cracks. The successive stages of Figure (3) show that with increasing strain, a greater number of microcracks are nucleated and subsequently combine to complete a continuous fracture path. Also, studies on AgCl reveal that cracks are not formed when the stress field associated with an arrested slip band is relieved by slip into the neighboring grain. On this basis, it appears that the embrittlement of AgCl is associated with the adsorption of complex ions in the presence of an applied tensile stress.

In summary, several general embrittling phenomena have been discussed, and it is now possible to state that an intergranular fracture path may become

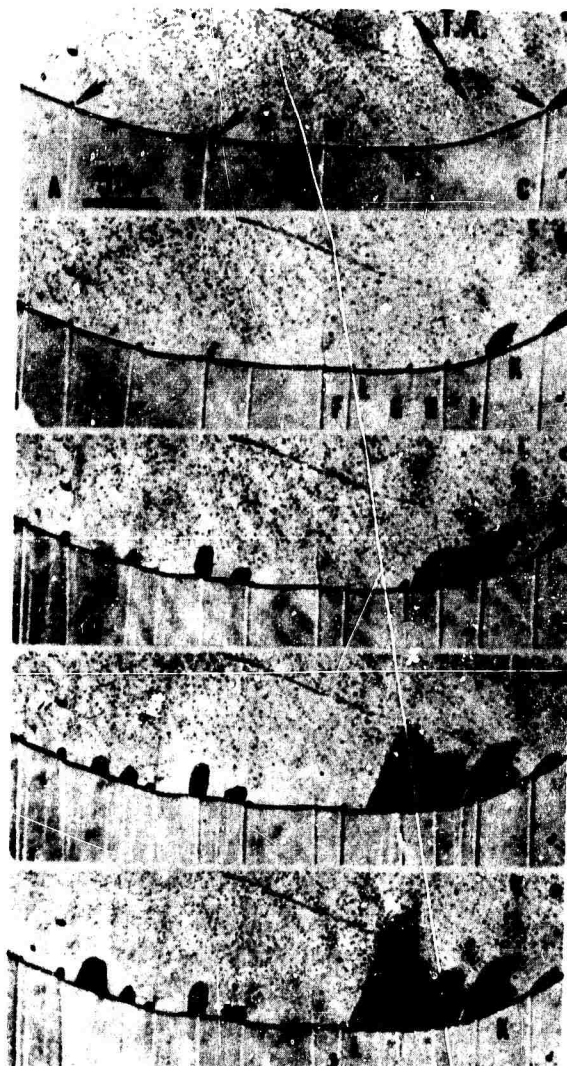


Figure 3. Polycrystalline silver chloride deformed in 6 N sodium chloride solution presaturated with AgCl_4^{3-} complexes; strain increasing progressively from sections (a) to (e): note that cracks are initiated only where slip bands are arrested at the grain boundary. The last three sections (c), (d), and (e) show microcracks combining and forming a continuous intergranular fracture path. (Westwood⁽⁸⁵⁾).

embrittled in two ways:

1. Solid solution (precipitation of second phase or solute segregation to the grain boundary).
2. Adsorbed species from the environment.

Both of these effects may act separately or combine to cause a decrease in the cohesive strength of the grain boundary. The explanation of how adsorbed species decrease the bond strength at localized sites is far from complete; however, the variables influencing intergranular brittle fracture are well defined for the phenomena of localized adsorption.

E. Stress Corrosion Cracking (SCC) of Precipitation Hardened Al Alloys:

The final section in this review will deal with the specific topic of SCC of age hardenable aluminum alloys. The characteristics of the phenomenon encompass most of the previous observations on crack nucleation and growth in the presence of adsorbed species. However, the specification of the conditions that are necessary and sufficient for stress corrosion cracking does not explain how the process occurs, and a major divergence of opinion exists in this area. Many of the mechanisms that have been proposed fall into two groups: those in which cracking involves mechanical failure steps and those in which the crack process along a path where electrochemical dissolution has occurred.

Evidence for an electrochemical dissolution feature of the SCC process seems irrefutable. The process can be both slowed down by cathodic polarization⁽⁴³⁾ and accelerated by anodic polarization⁽⁸⁶⁾. The simplest mechanism

of SCC is one whereby the crack consists of a path where nothing but electrochemical dissolution has occurred. A major objection usually raised to this mechanism is that corrosion rates would have to be prohibitively high in order to account for observed rates of crack propagation. Work by several authors including Nielsen⁽⁸⁷⁾ and Edeleanu⁽⁸⁸⁾ demonstrate that high corrosion rates can occur along localized paths, i.e., grain boundaries and planar dislocation networks in the matrix. This so-called tunneling corrosion has been proposed as the basis of a SCC mechanism⁽⁸⁹⁾.

In general, simple models of electrochemical dissolution do not explain adequately the specific nature of an environment affecting SCC. Such models would predict similar stress corrosion behavior in related electrolytes of comparable ionic strengths, i.e., equivalent electrochemical properties such as the conductance of the electrolyte. This isn't generally observed, and hence the applicability of such models is restricted. To account for the specific nature of such ions as chloride, hydroxide, and nitrate, Uhlig⁽⁹⁰⁾ has suggested that interfacial cracking, i.e., intergranular fracture, occurs with the adsorption along the fracture path of select species acting conjointly with electrochemical action to cause SCC. This description would be analogous to grain boundary embrittlement with the accelerating influence of galvanic action on the intergranular fracture.

According to the electrochemical concept, a stress corrosion crack should initiate at any site where galvanic relationships lead to selective corrosion.

In aluminum-copper alloys, a suitable site for selective corrosion is the region adjacent to a grain boundary, because this region is depleted in copper in solid solution and, therefore, anodic both to precipitate in the boundary and to the precipitate free matrix. In aluminum-magnesium alloys, an anodic site suitable for selective corrosion is the equilibrium precipitate along a grain boundary. With these alloys, maximum susceptibility to SCC might be expected where grain boundary precipitate is continuous. However, investigations on an Al-Zn-Mg alloy indicate that maximum susceptibility occurs at the first sign of grain boundary precipitate⁽⁹³⁾.

The dependence of stress corrosion cracking on microstructure in age-hardenable aluminum alloys has received little attention. Early investigations of Meikle⁽⁵³⁾ and Pugh⁽⁵²⁾ determined that the stress corrosion life of these alloys is known to decrease with increasing aging time to a minimum value, after which it progressively increases. Aside from this work little else is known about the microstructural dependence, and as a result a great deal of speculation exists in this area. It has been claimed that minimum stress corrosion life occurs at maximum hardness, because the difference in hardness between the grains and the precipitate-free zones i.e., soft denuded zone, is thought to be greatest at this stage. The argument follows that the soft denuded zone adjacent to the grain boundary deforms to fracture at a lower stress level than the matrix. However, studies of high purity alloys containing 5.5% Zn, 2.5% Mg, and separate additions of small amounts of either copper, manganese, chromium,

silicon, or ion, have indicated that minimum life occurs considerably earlier in the aging process than peak hardness⁽⁵²⁾. Recent work by Jacobs⁽⁹¹⁾ and Speidel⁽⁹²⁾ on an aluminum 7.3% Zn - 2.5% Mg alloy suggest that susceptibility in this alloy can be correlated with the presence of dislocation networks. Speidel infers that a planar dislocation network in the matrix corresponds to maximum SCC susceptibility, and a dispersed type dislocation network renders the material more resistant to SCC.

Tromans and Nutting⁽⁹⁴⁾, using electron microscopy attempted to consolidate the work of various investigators on crack initiation in face centered cubic metals. They conclude that the principal sites of crack initiation in both intergranular and transgranular modes of failure are dislocations. Preferential dissolution of dislocations in continuous regions of high dislocation density produces a series of microcracks (pits) which link to form macrocracks. The continuous regions are grain boundaries for intergranular failure, and octahedral planes containing planar arrays of dislocations for transgranular failure. The process of intergranular SCC as proposed by Tromans and Nutting might appear as the embrittlement and fracture of AgCl, shown in Figure (3). These authors also point out that, while many features of SCC may be explained in terms of dislocation distributions, another apparently basic requirement for initiation is solute segregation. Accepting that solute segregation is necessary for production of SCC sites, then differences in susceptibility to SCC can be accounted for which could not be explained solely by dislocation configurations. For

example, ultra pure materials are apparently immune to SCC, but the addition of impurities may render the material susceptible to SCC. Thompson and Tracy⁽¹⁰¹⁾ have shown this in high purity copper where a phosphorous content as low as 0.004% renders the material susceptible to SCC in an ammonia atmosphere.

Brief mention should be made of the mechanism proposed by Forty and Humble⁽⁹⁵⁾. These authors propose that SCC, at least in the particular system they studied (brass-ammonia), occurs not in the metal but in the surface film itself. The crack is propagated by repeated formation and rupture of a tarnish film.

In summary, it is the author's opinion that all environmental fracture mechanisms previously discussed have a thread of continuity based on dislocation mobility and configuration in the matrix microstructure. This opinion is that inhomogeneous plastic flow in the matrix leading to banded slip networks creates a condition which is much more susceptible to fracture than a matrix with a more dispersed, or homogeneous slip. Also, the mobility or velocity of dislocations in the banded structure would determine the degree (time involved) for fracture to occur. This argument is substantiated by the present work on the intergranular fracture processes in the Al-Zn system.

II. Experimental Procedures

A. Experimental Material:

The original objective of this experimental program was to determine the influence of microstructure on the stress corrosion cracking susceptibility of age hardenable aluminum alloys. Initial experiments which were performed on commercial aluminum alloys, i.e., Al - 4.3% Cu - 1.5% Mg and Al - 1.6% Cu - 2.5% Mg - 5.6% Zn, showed them to be unsuitable for the type of experiments planned. Apart from their complex compositions, a large amount of insoluble constituents, i.e., Si, Fe, and Cr complexes, were present in the microstructure. Also, a preferred elongated grain structure resulting from the rolling of plate to sheet existed after thermal treatments, and in general, both commercial alloys were not sufficiently susceptible to stress corrosion cracking. The selection of an appropriate aluminum system to study was aided by previous work in high purity Al-Zn and Al-Zn-Mg alloys^(14,15). The study of these systems showed them to be much more susceptible to stress corrosion cracking than the commercial alloys. As a result of these investigations, a special cast of high purity aluminum alloys was obtained from the Aluminum Company of America (New Kensington Research Laboratories). The nominal compositions of these alloys are listed below: (wt %)

Al - 4% Cu

Al - 7% Zn - 23% Mg

Al - 15% Zn

Al - 7% Zn - 1% Mg

The selection of the binary Al-Zn alloy over the other alloys cast was

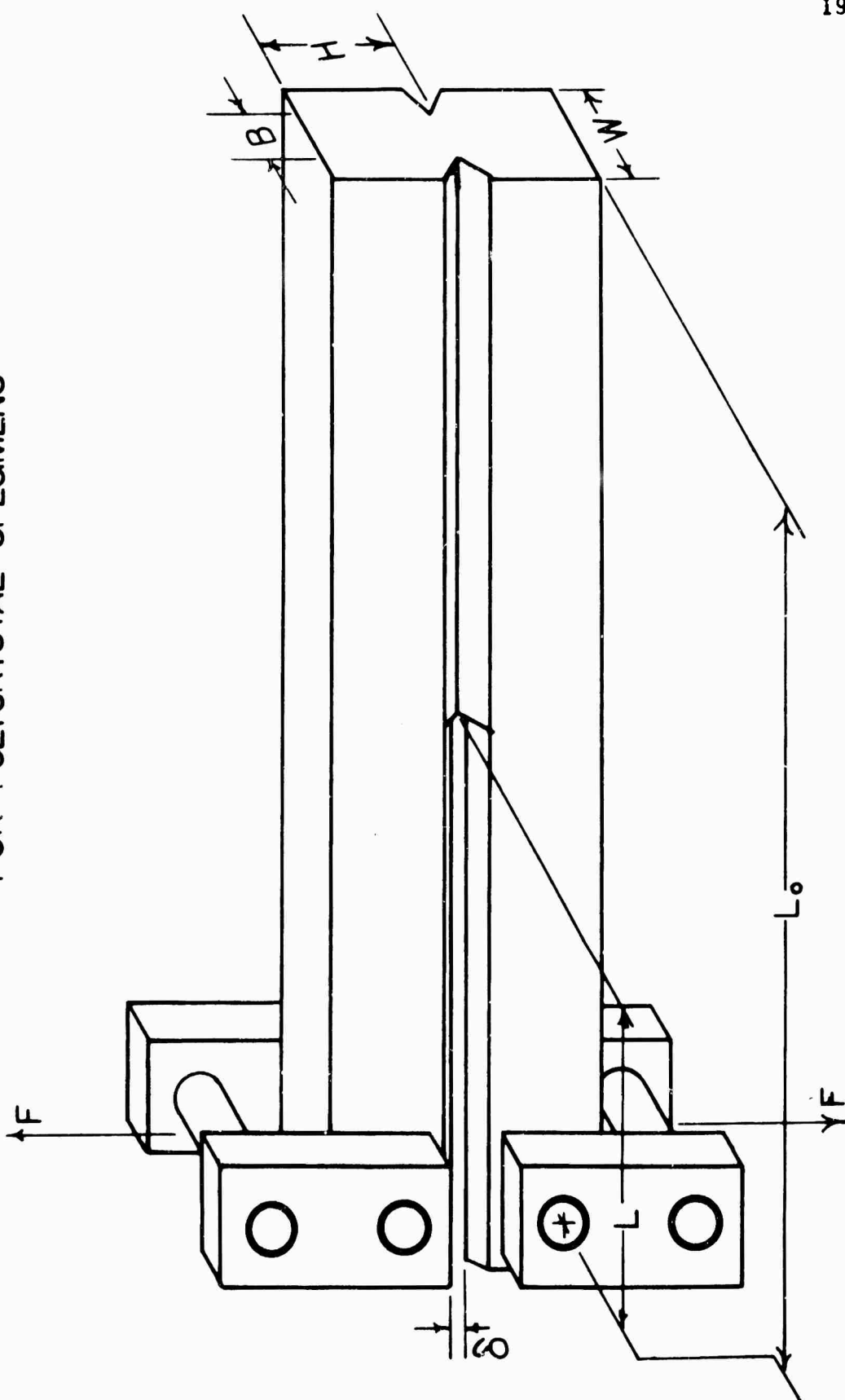
based on its indicated high degree of stress corrosion susceptibility. Also, this binary alloy possesses a wide range of microstructural changes, (different volume fractions of coherent, semi-coherent, and incoherent precipitates) and at the inception of this program, characterization of the Al-Zn microstructure had been previously investigated^(16,17). Thus, a detailed investigation of the microstructure was not necessary and full attention could be devoted to the cracking phenomena. The as received material was in the form of 0.040 inch thick sheet and 0.50 inch thick plate, and the actual composition of the Al-Zn alloy used was 14.8 wt % Zn and less than 0.001 wt % (Fe + Si). This composition was independently verified by spectroscopic and wet chemical analysis.

B. Specimen Preparation.

1. Polycrystal Specimens:

Physical limitations on specimen test pieces are imposed by the as received material (plate and sheet). The as received plate stock was machined to the double cantilever beam, DCB, geometry depicted in Figure (4) with constant dimensions $W = 0.50$ in., $L_o = 3.25$ in., and $H \approx 0.50$ in. The other critical dimensions (L , B) for each plate specimen are listed in Appendix I-A (tabulated data). The side groove geometry of these DCB specimens consists of a notch depth equal to $(\frac{W - B}{2})$ and a notch radius of approximately 0.010 in. These notched DCB specimens will be referred to in future discussions as polycrystal test specimens. After appropriate heat treating conditions these specimens possess an equi-axed grain structure with a mean grain diameter of approximately 1mm.

DOUBLE CANTILEVER BEAM GEOMETRY
FOR POLYCRYSTAL SPECIMENS



19A

Figure 4. Polycrystal DCB specimen loaded up to a fixed-deflection δ for force F and an initial crack length L ; the side-groove depth, $(W-B)/2$, promotes a plane strain stress state and confines intergranular crack advance to the mid-beam height H .

2. Bi-crystal Specimens:

In a study of intergranular fracture, the testing of bi-crystals offers a well defined crack path when compared to arbitrarily oriented grains in the polycrystal specimens. The DCB test geometry for bi-crystals is shown in Figure (5), and the actual values of (H, G, L_o, L) for each bi-crystal specimen are listed in Appendix I-A. The bi-crystal specimens were obtained by two methods:

- (a) Bulk strain anneal.
- (b) Growth through a gradient furnace.

Initially, a 6 in. \times 3/4 in. \times 0.040 in. tensile specimen was cut from the sheet material. This specimen was then solution heat treated at 530°C and quenched into an ice-bath. Subsequently, the specimen was given a 2% critical plastic strain. This critical strain was pre-determined by solution heat treating a number of specimens and straining them to successive strain increments. The optimum strain was then determined by measuring the recrystallized grain size. Once these tensile specimens received the critical strain, they were either annealed for 10 days at 585°C or passed through a gradient furnace. The gradient furnace consisted of a copper-coil cold trap adjacent to a hot zone in a resistance wound furnace. A temperature gradient of 650°C/in. existed between the cold and hot zone, and through this gradient the tensile specimens were drawn at 3mm/hr. After the specimens were annealed for 10 days or pulled through the gradient furnace, they were etched with Keller's etch, i.e., 2% HNO_3 , 1.5% HCl , and 1% HF . Provided a straight grain boundary greater than

DOUBLE CANTILEVER BEAM
GEOMETRY FOR BI-CRYSTAL
SPECIMENS

20A

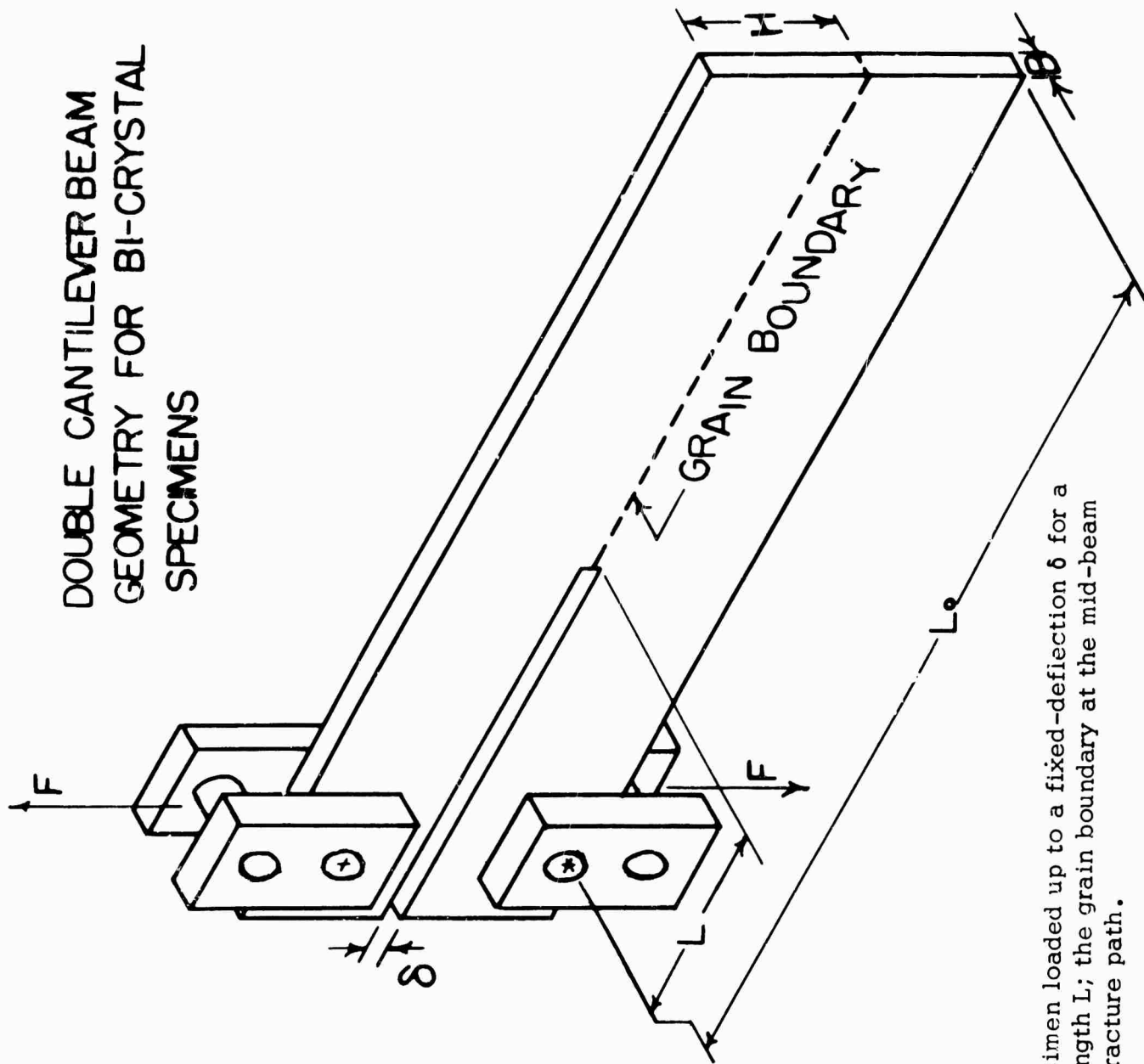


Figure 5. Bi-crystal DCB specimen loaded up to a fixed-deflection δ for a force F and an initial crack length L ; the grain boundary at the mid-beam height H is the intergranular fracture path.

8 mm in length was found, a bi-crystal DCB specimen is cut with a jeweler's saw according to Figure (5). The exact dimensions of each bi-crystal tested are listed in Appendix I-A. It was found that both methods of growing bi-crystals were equally favorable, and both methods were used to obtain bi-crystal specimens.

C. Thermal History:

After the machining of polycrystal specimens and cutting of bi-crystal specimens, appropriate heat treatments were performed on the test pieces. The thermal treatments carried out in this program were initially developed to study the effects of grain boundary precipitates, in the Al-15 wt % Zn system, on the intergranular fracture process in a corrosive environment. On this basis, an aging temperature of 155°C was selected after a solution anneal. The aging temperature (155°C) was chosen above the G.P. zone solvus line, i.e., the extrapolated metastable phase boundary for the existence of a coherent zinc precipitate in solid solution⁽¹⁶⁾. This was to insure heterogeneous nucleation and growth at grain boundaries and prevent homogeneous nucleation of the coherent precipitate in the matrix. Thus, it was reasoned successive aging times at 155°C would tend to coarsen grain boundary precipitates. To achieve this type of heat treatment, a vertical-drop furnace (glow bar and resistance wound) was constructed with a controlled silicone oil bath situated beneath the furnace. A specimen annealed in the furnace could be instantly dropped into the silicone oil bath at 155°C without reaching ambient temperature. A schematic drawing

of the heat treating conditions is shown in Figure (6), and a complete description of the microstructures tested is discussed in sections VI-A and B.

D. Transmission Electron Microscopy:

The characterization of microstructures resulting from the heat treatments depicted in Figure (6) was done by standard thin film transmission electron microscopy. In this work the Phillips 200 (Electron Microscope) was used, and thin film specimens were prepared by a jet polishing technique (Electrolyte, 33% Nitric - 67% methanol; temperature - 30°C and 10 volts). In addition to these specimens, acetate replicas shadowed with platinum (approximately 45° shadow angle) were made of intergranular fracture surfaces and pitted corrosion surfaces. Thus, topographic features involved on these surfaces were studied at high magnification (approximately 10,000X). All the replica and thin film work was supplemented by light-microscope work (up to 1500X on a Zeiss-Microscope).

E. Bi-crystal Orientations:

The bi-crystal double cantilever beam test specimens afford a way of experimentally evaluating the effects of grain boundary orientation, i.e., the crystallographic orientation of the adjacent grains forming the boundary, on the intergranular fracture process. Initially, all bi-crystal specimens were polished to a high finish either mechanically or electrolytically. The specimens were then heat treated at 450°C for approximately 1 hour to anneal out residual cold work. Following the thermal treatment, the grain boundary orientation was

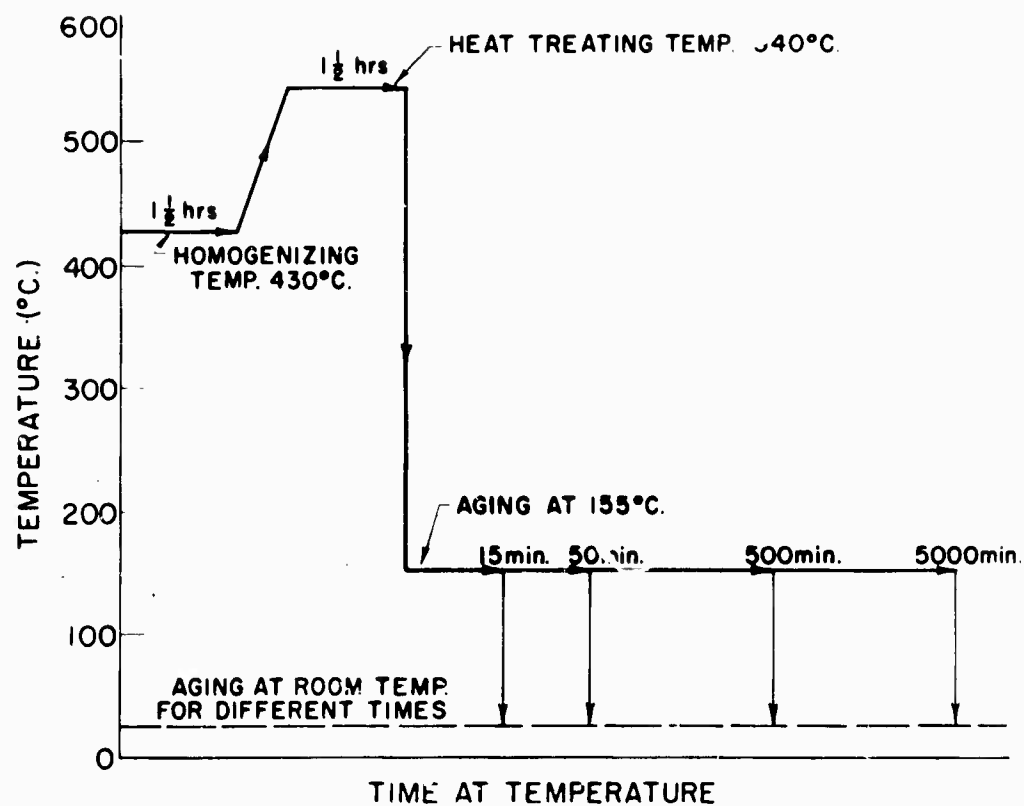


Figure 6. Schematic drawing showing solution anneal at 540°C followed by a direct quench to 155°C; progressive aging at 155°C is followed by a direct quench to room temperature (25°C) and aging at 25°C for different times.

determined by taking back reflection laue pictures of the two grains adjacent to the boundary. To facilitate the indexing of bi-crystal specimens, polaroid film was used, and this cut exposure times to 3 minutes. All bi-crystal specimens had to meet two requirements:

1. Straight grain boundary perpendicular to free surfaces (perpendicular to both grains), see Figure (5).
2. No intersecting sub-boundaries over a tested fracture path of approximately 4 to 5 mm.

The method of characterizing the orientations tested is discussed in section IV-C, Reduced Data.

F. Testing Procedure for Double Cantilever Beam (DCB) Geometry:

A description of the testing procedure for the DCB geometry of polycrystall and bi-crystal specimens will be divided into two categories:

- I. Loading DCB specimens to fixed-grip conditions.
- II. Measurements of crack extension and load relaxation.

Fixed Grip Conditions: The complete test geometry of the polycrystal and bi-crystal specimens is shown in Figures (4) and (5). These two figures show the DCB geometry loaded to a fixed deflection, δ . The load is applied to the specimen through a pair of stainless-steel grips by pins passing through to the cantilever arms of the specimen. The stainless-steel grips are self aligning to achieve a symmetric load application to both cantilever arms without introducing a bending moment about the grips. The pin-holes for gripping the polycrystal

DCB specimens are $1/4$ " in diameter and are centered approximately $1/4$ " from each free surface of the cantilever arms. Similarly, the bi-crystal specimens have pin-holes $1/16$ " in diameter which are centered about $1/16$ " from each free surface of the moment arms. Since the DCB specimens were tested both in air and in a corrosive environment of 0.5 molar NaCl, a loading arrangement had to be devised whereby the specimen could be loaded under a tensile force, F , (see Figures (4) or (5)) and simultaneously be accessible to the corrosive environment. This type of loading arrangement was accomplished by fixing a stain-less-steel compressive jig to the bottom side of the moving cross-head on an Instron machine. The tensile load is applied to the specimen by having one set of DCB-specimen grips affixed to the bottom of the compressive jig while the other set of grips is attached through linkage to the Instron load-cell. A downward motion of the Instron cross-head is transmitted as a tensile force F and deflection δ to the DCB specimen. This applied load through the DCB grips is shown in Figure (4). In conjunction with this loading arrangement, a square plexi-glass container was mounted on a mechanical jack under the compressive loading jig. This arrangement gives flexibility for testing in air without the container or jacking the container up under the compressive jig and testing the specimen in 0.5 molar NaCl.

The testing procedure discussed is applicable to both polycrystal and bi-crystal specimens. However, because of the difference in the size of the polycrystal and bi-crystal specimens, a corresponding difference in the load

range or Instron scale had to be used. Typically, bi-crystals were tested in the load range (1 to 15 lbs) while polycrystals were tested from (100 to 500 lbs). Thus, to achieve full sensitivity in testing polycrystals, a D load-cell (1000 lbs max. load) was used with a 50 lb suppression increment set on the Instron. The sensitivity of load relaxation for polycrystal specimens, i.e., ± 0.5 lbs., is much smaller than the typical reproducibility of ± 10.0 lbs for load relaxations between different polycrystal specimens with the same geometry. Bi-crystals were tested with a C load-cell (50 lbs max. load) and a 2 lb suppression increment. The ultimate load sensitivity of the Instron for these tests is then the suppression increment multiplied by the smallest fractional division of the Instron chart-scale, i.e., (1/100). Thus, an extremely high sensitivity of ± 0.01 lb could be achieved when monitoring load relaxation in bi-crystals. This high sensitivity in monitoring load relaxation in bi-crystal tests exceeds the reproducibility in experimental measurements, i.e., typically ± 0.2 lb load relaxation, from one specimen to the next. However, a sensitivity of $\pm .01$ lbs was used on some bi-crystal tests to determine if a discontinuous load drop, i.e., no change in load over a small finite time, was present during crack extension.

The loading up of the DCB specimens was done with a deflection rate, or cross-head motion, of 0.02 in./min. and an Instron chart speed of 10 in./min. At a predetermined load, the cross-head was stopped and fixed to maintain a constant deflected throughout the entire test. The amount of deflection between

pin-holes, or loading points, was measured optically, and this deflection could also be calculated from the Instron chart knowing the chart speed and deflection rate. The difference between the calculated and measured deflection was within $\pm 5\%$. This difference was attributed to the test linkage or machine stiffness (approximately $5 \sim 9 \times 10^4$ lbs/in.), which took up a small part of the total deflection resulting from the downward displacement of the cross-head. Consequently, the high machine stiffness reduces any change in deflection within $\pm 5\%$ of measured deflection in the Instron linkage during load relaxation in the DCB specimen. This leads to a negligible change in deflection at the free ends of the DCB specimen, and the test is carried out under essentially fixed-grip conditions, i.e., constant deflection of DCB specimen arms.

G. Measurement of Crack Extension and Load Relaxation:

When the polycrystal and bi-crystal specimens are loaded up to a constant deflection, load relaxation can occur only if it is accompanied by crack extension in the DCB specimen. This statement implies that localized plastic flow, i.e., creep at room temperature, at the crack tip and in the cantilever arms of the DCB specimen is exceedingly small and does not contribute to an observable load relaxation. To assure the suppression of bulk plastic flow, all DCB specimens are loaded in the linear elastic range, and any creep effects present are confined to load relaxations of approximately 10^{-2} lbs/min (well within the reproducibility of the experiment). Thus, the rates of load relaxation and crack extension are related through the constraint of constant deflection.

The load on a DCB specimen is continuously monitored by an Instron chart, with a chart speed of either (0.2 or 0.5 in/min.). Distance on the chart can be converted to time knowing the chart speed, and thus, the Instron chart records load versus time during crack propagation. Simultaneously, a mounted cathetometer (10X magnification) is used to take crack length readings. The sequence for taking measurements is first an optical crack length reading followed by a position mark on the Instron chart to denote load and time.

In summary, the testing procedure for each DCB specimen consists of four quantities to be measured:

1. Deflection, δ , which is constant throughout the test.
2. Instantaneous crack length, L .
3. Instantaneous load, F .
4. Time, t .

These experimental quantities can then be used to calculate an average crack velocity corresponding to either a stress intensity factor or an average rate of elastic strain energy released.

H. Supplementary Test Procedures:

In addition to the intergranular fracture studies of DCB specimens in air and in 0.5 molar NaCl, direct corrosion studies were preformed on the microstructures of interest. These studies entailed the preparation and heat treating of tensile specimens which were then placed in a 0.5M NaCl solution for various times in the absence of stress. The tensile specimens were then examined

optically and by replication for signs of general corrosion. Also, the tensile specimens were pulled to fracture and the yield strengths determined. This was done to ascertain if a general degradation in bulk mechanical properties resulted from exposure to the corrosive environment without application of stress. These supplementary tests were performed in the hopes of correlating general corrosion for a particular microstructure to the results obtained in the stress corrosion cracking tests of the DCB specimens.

III. Theory

A. Experimental Technique Used to Measure Stress Intensity Factor and Elastic Strain Energy Release Rate:

The fracture toughness of a material can be defined as the elastic strain energy released in extending a crack an incremental unit area during propagation. Provided fracture occurs in a brittle manner, i.e., suppression of bulk plastic flow, the fracture toughness is found to be an inherent property of the material. To evaluate the fracture toughness of a material in terms of the energy loss in the system, use is made of the fact that the crack and plastically strained area in its vicinity are surrounded by an elastic stress field. The total energy stored in the stress field is found by utilizing elasticity theory, and the change in elastic strain energy per unit area of crack advance is equal to the fracture toughness.

An experimental determination of the elastic strain energy release rate can be accomplished by various geometries and loading conditions. A selection of the optimum test conditions depends on the desired accuracy and reproducibility of the parameters to be measured. With this in mind, Figures (4) and (5) show the appropriate geometry and loading condition decided on to obtain valid measurements of elastic strain energy release rate and crack velocity. The specimen design shown in these figures is commonly referred to as a double cantilever beam specimen, DCB, and derives its name from the symmetry of two cantilever beams involved about the mid-beam height of the crack tip. During testing, DCB specimens are loaded to an applied force, F , corresponding to a

crack length, L , and a deflection, δ (see Figure (4)). The first constraint imposed on this loading arrangement is that a linear relation between force and deflection be obeyed.

This implies that the DCB specimen is tested in the elastic range, with only localized plasticity at the crack tip. Provided the plastic energy dissipated at the crack tip during loading is sufficiently small compared to the stored elastic energy, a meaningful elastic analysis can be applied to the DCB geometry.

The second constraint on the test geometry is that crack propagation be confined to the mid-beam height, H , of the DCB specimen. This criterion is necessary to preserve the symmetry of the specimen and yield valid results on the elastic energy release rate. As discussed in the section entitled "Source of Errors", IV-D, deviations out of the mid-beam height during crack propagation can lead to significant errors in measurements of both crack velocity and elastic strain energy. Also, too great a deviation of the crack front from mid-beam symmetry will eventually lead to failure of the DCB specimen through one of the cantilever arms and render the test piece and analysis useless.

The third and last constraint on the DCB specimen results from the type of loading condition selected. When analyzing the loading possibilities available to the DCB geometry, it becomes apparent that three distinct loading arrangements exist in storing sufficient elastic strain energy for crack propagation. These different load applications are:

I. Fixed-Grip or Constant Deflection: The deflection, δ , at the point of load application remains constant and independent of crack length during crack propagation. Thus, provided there is sufficient stored elastic energy when the initial load is applied, crack propagation will occur with a decrease in the applied load and no change in the deflection at the point of loading.

II. Constant Force or Load Application: This condition is met by applying a constant weight or load at the free ends of the cantilever arms. This type of arrangement insures crack extension under an increasing deflection while the applied force remains constant.

III. Continuously Increasing Load Application: This type of loading is accomplished by imposing on the DCB geometry a rate of separation of the free ends of the cantilever arms. If linearity exists between the applied load and the deflection at all times, then the imposed rate of deflection will cause a corresponding increase in the applied load.

The inherent advantages or disadvantages of these different loading conditions will not be discussed, but the underlying basic difference will be mentioned. Intuitively, the reader may observe that as crack extension occurs, the increasing length of the cantilever arm acts as an effective moment arm and thus, tends to magnify the applied load at the crack tip. When analyzing for the amount of available elastic strain energy between the three loading arrangements, it can be shown that load conditions (Nos. II and III) give a constant of continuously increasing amount of stored elastic strain energy available

during crack extension. However, during crack propagation under fixed-grip conditions, the amount of available energy to propagate the crack continues to decrease as the crack grows. This results because of load relaxation off-setting the increase in the length of the cantilever arms during crack extension.

The attractive feature of the fixed-grip geometry is the continuously decreasing amount of energy available to cause crack growth. Thus, if a continuous function exists between the amount of stored elastic strain energy and the crack velocity, a continuous deceleration of the crack front during propagation would be expected. As a consequence of this, the loading condition readily lends itself to setting test limits on the DCB specimen. The upper limit, or maximum amount of stored energy, is fixed by the point where linear elasticity ends and gross plasticity begins. The lower testing limit for this geometry and loading condition is fixed when the stored elastic strain energy has decreased to such an extent it is unable to propagate the crack further. These physical constraints make testing of the DCB geometry under a constant deflection an ideal way of measuring the dependence of crack velocity on the rate of elastic strain energy released.

In the preceding discussion of the test geometry and loading condition, no mention was made of the stress field distribution around the crack tip. Rather than discussing the stress field as the cause of crack propagation, an alternate viewpoint was taken where cracking is controlled by the rate at which the stored strain energy can be supplied to the propagating crack. Originally, this

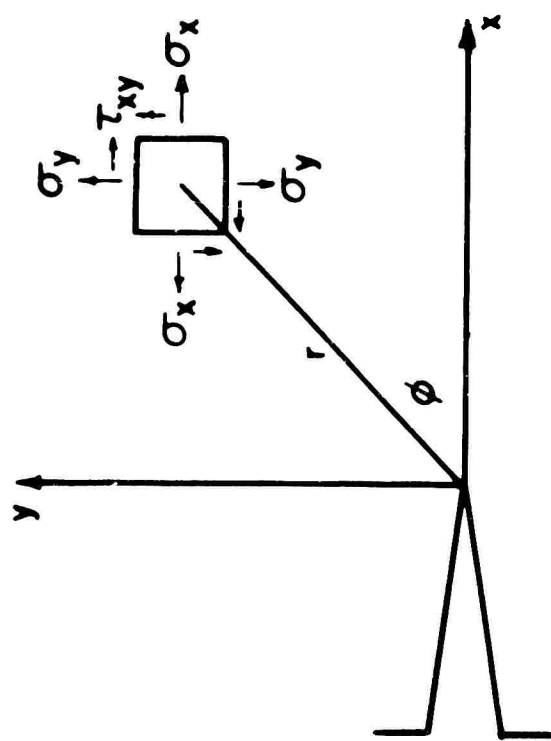
approach was taken by Griffith⁽¹⁾ who set up an energy criterion for crack instability. However, a stress analysis approach where the intensity of the stress field at the crack tip determines whether or not a crack will run is compatible with the energy criterion. Since both methods are equally valid in describing brittle crack propagation, they have been grouped under the general title of "Fracture Mechanics".

Many previous investigators studied the elastic stress distributions around cracks with some of the earliest contributions being from Inglis⁽²⁾ who studied an internal crack using elliptical bounding surfaces.

Recently, Irwin, Kies, and Smith⁽⁹⁷⁾ formulated a closed form expression for the elastic stress distribution at the base of a stationary crack. The results of their analysis, i.e., equations showing stress distribution around crack tip, are shown in Figure (7), part A. This figure shows a unit area element a distance, r , away from the crack tip and an angle ϕ away from the crack plane. The appropriate stress states on the elemental area are labeled, and the equations describing these stress states are shown below the figure. A more refined analysis of the elastic stress state ahead of the crack was developed by Williams⁽⁹⁾. The results of his analysis are shown in Figure (7), part B. The results in part B only apply for a symmetric stress distribution, i.e., loading of a DCB specimen. Also, the stress states are expressed in polar coordinates, and represent a rotation of the unit element in part A by ϕ degrees. Finally, the analysis by Williams yields a series solution for σ_{rr} , $\sigma_{\varphi\varphi}$, and $\sigma_{r\varphi}$, and

Elastic Stress State at Crack Tip

Part A



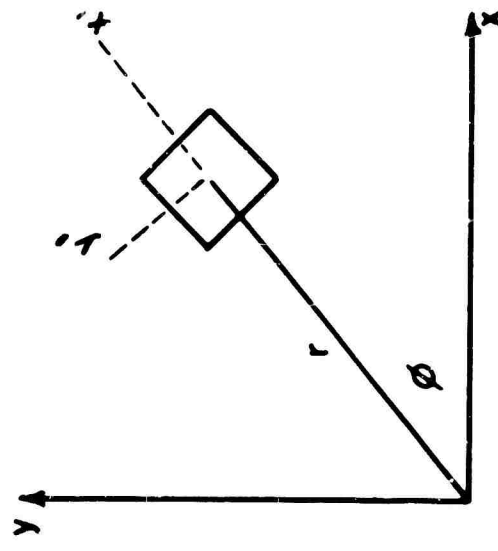
Transformation

$x' \equiv$ Radial Axis
 $y' \equiv \phi$ Axis

$$\sigma_{rr} \equiv \sigma_{xx}'$$

$$\sigma_{\phi\phi} \equiv \sigma_{yy}'$$

Part B



$$\sigma_{yy} = \frac{K}{(2\pi r)^{\frac{1}{2}}} \cos \frac{\phi}{2} \left[1 - \sin \frac{\phi}{2} \quad \sin \frac{3\phi}{2} \right]$$

$$\sigma_{xx} = \frac{K}{(2\pi r)^{\frac{1}{2}}} \cos \frac{\phi}{2} \left[1 + \sin \frac{\phi}{2} \quad \sin \frac{3\phi}{2} \right]$$

$$\sigma_{rr} = \frac{K}{(2\pi r)^{\frac{1}{2}}} \left[\frac{5}{4} \cos \frac{\phi}{2} - \frac{1}{4} \cos 3\frac{\phi}{2} \right] + \dots$$

$$\sigma_{\phi\phi} = \frac{K}{(2\pi r)^{\frac{1}{2}}} \left[\frac{3}{4} \cos \frac{\phi}{2} + \frac{1}{4} \cos 3\frac{\phi}{2} \right] + \dots$$

$$\sigma_{xy} = \frac{K}{(2\pi r)^{\frac{1}{2}}} \cos \frac{\phi}{2} \left[1 + \sin \frac{\phi}{2} \quad \cos \frac{\phi}{2} \right]$$

Figure 7. Elastic stress distribution at the base of a stationary crack; Part A is the resulting stress distribution due to Irwin⁽³⁾, Part B shows the first term in a series solution for the stress distribution (different coordinate system than Part A), due to Williams⁽⁹⁾.

these stresses don't increase without limit as the radial distance approaches the crack tip.

The general result of the elastic stress analyses shown in Figure (7) is that the stress state at any distance from the crack tip is directly proportional to a geometric factor and inversely proportional to the square root of 2π times the radial distance from the crack tip. The constant in the stress equations, K , converting the above mentioned proportionality to an equality is called the stress intensity factor. The name of the constant is appropriate since it indicates the strength of the principal stress fields. A direct evaluation of the stress intensity factor depends on the geometry of the specimen and crack and the type of imposed stress state. The closed form expression relating the stress intensity factor to the DCB geometry under various loading conditions will be discussed in the next section.

The experimental technique discussed to this point makes mention of employing the DCB geometry under constant deflection conditions to actually measure the rate of elastic strain release for a given crack velocity. Alternately, the elastic stress field distribution at the crack tip can be determined by calculating, K , for the experimental test geometry. A thorough discussion will follow of the mathematical expressions applicable to the DCB geometry in determining the rate of elastic energy released and the stress intensity factor.

B. The Equations Used to Calculate Elastic Strain Energy Released (G) and Stress Intensity Factor (K):

The objective of this section is to describe the appropriate equations for calculating both the elastic strain energy released, G , during crack extension and the stress intensity factor, K , causing crack propagation in a DCB specimen under fixed-grip conditions. The development of equations for calculating G will show the inherent assumptions made in setting up a reversible elastic energy balance during crack extension.

The concepts of "Fracture Mechanics", i.e., the extension of continuum elasticity theory to describe the stress state at a crack tip and the conservation of energy during fracture, is used to relate, G , to the stress intensity factor, K . The significance of K to the elastic stresses at a crack tip is discussed with particular emphasis on the type of stress state; bi-axial plane-stress or tri-axial plane-strain. The stress state present in a test specimen determines the relationship between K and G , and thus, the appropriate dependence of K on G is discussed for a notched, DCB test geometry shown in Figure (4).

The final results of this section are closed form expressions for G and K in terms of the experimentally measured quantities: deflection (δ), crack length (L), and force (F). Also, a crack velocity V corresponding to either G or K can be calculated from crack length (L) and time (t). The expressions developed in this section are then used to obtain the dependence of crack velocity on G for bi-crystal specimens and the velocity dependence on K for polycrystal specimens.

1. Elastic Strain Energy Released (G) During Crack Propagation.

The energy balance treatment of fracture that originated by Griffith⁽¹⁾ is the basis of this discussion on fracture mechanics. The toughness of a material can be defined as the elastic strain energy release rate needed to propagate a crack in the material. The energy release per unit area of new crack face can be regarded as an apparent surface energy. If fracture is carried out in a reversible fashion, the work of fracture is equal to the intrinsic surface energy of the material. Aside from the creation of new surfaces during fracture, the predominant energy absorbtion process is plastic deformation. In most cases, the apparent surface energy, γ_A , is the sum of the true surface energy, γ , plus the energy dissipated through plastic deformation, γ_p . The subsequent treatment relates the intrinsic material quantity, γ_A , to measurable experimental quantities in a DCB test geometry.

Originally, Irwin and Kies⁽³⁾ derived the general expression relating the tensile force F applied to a specimen containing a crack of length L to the amount of elastic energy released, dU , when the crack propagates and increases its length by dL . The equation is:

$$\frac{dU}{dL} = \frac{F^2}{2} \frac{d(1/M)}{dL} , \quad (III.1)$$

where $(1/M)$ is the compliance of the specimen. This general equation can be further reduced if we impose the constraint of a "dead-grip", or constant deflection, condition on crack propagation. If the DCB test geometry in Figures (4) and (5) is linearly elastic in the applied load range, the following relation between

force and deflection is valid; $F = M \times \delta$, where F is the applied load, M is the specimen stiffness, and δ is the deflection. Thus, for a constant deflection,

$$\frac{d(1/M)}{dL} = - \frac{\delta}{F^2} \times \frac{dF}{dL} . \text{ Combining this derivative of compliance with Eq. (III.1)}$$

$$\frac{dU}{dL} = - \frac{\delta}{2} \times \frac{dF}{dL} . \quad (\text{III.2})$$

The physical significance of Eq. (III.2) is shown graphically in Figure (8) where the cross-hatched area represents the elastic strain energy released for a crack extension, dL . A crack will continue to advance in a material if the elastic energy released can supply both the surface energy, γ , of the new crack faces and the energy dissipated through plastic flow, γ_p , i.e., when

$$dU = (2\gamma + 2\gamma_p) \times B \times dL , \quad (\text{III.3})$$

where B is the width of the specimen. From Eqs. (III.2) and (III.3)

$$G = - \delta/2B \times dF/dL , \quad (\text{III.4})$$

where $G = 2\gamma + 2\gamma_p$ or the sum of all processes liberating energy during fracture. The value of dF/dL may be determined experimentally or calculated from elasticity theory knowing the geometry of the specimen. The calculation can be made if complete elasticity is assumed or $\gamma_p = 0$ and $G = 2\gamma$. For a DCB specimen, Figure (5), Gilman⁽⁴⁾ used the calculated value of compliance and dF/dL and derived the equation

$$G = 12 F^2 L^2 / E_{(y)} B^2 H^3 , \quad (\text{III.5})$$

where $2H$ is the height of the specimen and $E_{(y)}$ is Young's Modulus. Westwood and Hitch⁽⁵⁾ improved the accuracy of Eq. (III.5) by allowing for a shear

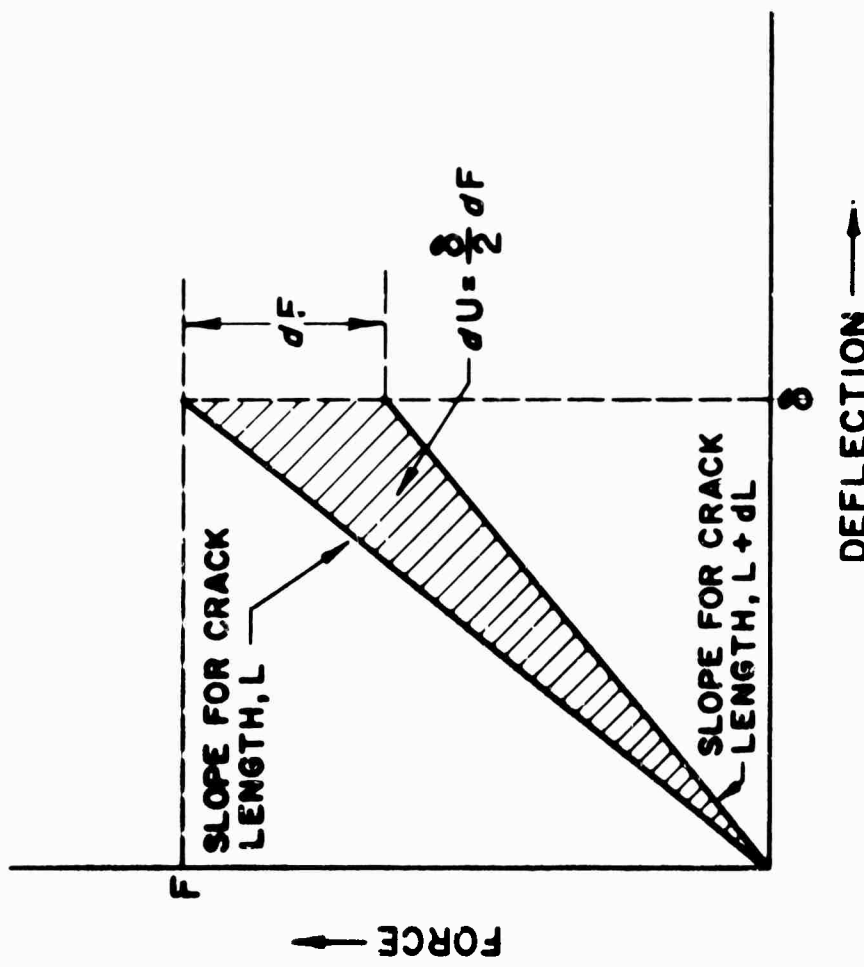


Figure 8. Incremental elastic strain energy released, dU , for crack extension, dL , under fixed-grip conditions or at a constant deflection, δ .

deflection of the beams and obtained

$$G = \frac{12F^2 L^2}{E(y) B^2 H^3} \left(1 + \frac{\beta E(y) H^2}{4\mu L^2} \right) \quad (\text{III.6})$$

where μ is the shear modulus and β is a constant. The form of Eq. (III.6) was further improved by Gillis and Gilman⁽⁶⁾ who obtained

$$G = \frac{12F^2 L^2}{E(y) B^2 H^3} \left[1 + (n + 1) c \left(\frac{H}{L} \right)^{2-n} + \frac{\beta E(y)}{4\mu} \left(\frac{H}{L} \right)^2 \right]. \quad (\text{III.7})$$

By taking into account the contribution to specimen compliance of deformation in the uncracked portion of the specimen, Wiederhorn and Shorb⁽⁷⁾ found the quantities n, c , and β , which are constants depending on the conditions at the fixed end of the cantilevers, to be practically independent of the elastic constants of the specimen material. Substituting their numerical values for n, c , and β into Eq. (III.7), Wiederhorn and Shorb obtained

$$G = \frac{12F^2 L^2}{E(y) B^2 H^3} \left[1 + 1.32 \left(\frac{H}{L} \right) + 0.542 \left(\frac{H}{L} \right)^2 \right], \quad (\text{III.8})$$

which they note is in excellent agreement with the expression Srawley and Gross⁽⁸⁾ derived by calculating the stresses at the crack tip of a DCB specimen using an elastic stress analysis independent of any energy considerations during the fracture process, namely;

$$G = \frac{12.02F^2 L^2}{E(y) B^2 H^3} \left[1 + 1.335 \left(\frac{H}{L} \right) + 0.446 \left(\frac{H}{L} \right)^2 \right]. \quad (\text{III.9})$$

The pronounced similarity of Eqs. (III.8) and (III.9) is strong evidence for their validity, because they were derived through completely independent approaches. Also, the validity of these equations shows the applicability of using either a stress analysis or energy approach in describing crack propagation. However, it should be mentioned again that the stress and energy analyses are based on linear elasticity, and it is assumed that no general plastic flow occurs. Thus, it is not obvious that Eqs. (III.6) and (III.8), derived for a material exhibiting no plastic flow during fracture, $\gamma_p = 0$, should apply when $G = 2\gamma + 2\gamma_p$ and $\gamma_p \neq 0$. But by measuring the slope dF/dL of the applied force versus crack length during crack propagation, Eq. (III.4) could be used directly, and incidentally, the applicability of Eqs. (III.6), (III.8), and (III.9) could be checked. Thus, the determination of the elastic strain energy released, G , during crack propagation can be done experimentally by measurements of: deflection (δ), cross-section thickness (B), force (F), and crack length (L). A graph of F versus L can be used to determine slopes, dF/dL , which in turn are used to calculate the corresponding values of G .

2. Relation Between Elastic Strain Energy Release Rate (G) and Stress Intensity Factor (K).

The previous discussion has fixed the expression relating experimental quantities to the elastic strain energy released during crack propagation. It now remains to describe the equivalence of G to an elastic stress field at a crack tip. With a knowledge of the dependence of this stress field on G , it is

possible to describe the fracture process in terms of the tensile and shear stresses, i.e., σ_{rr} , $\sigma_{\varphi\varphi}$, $\sigma_{r\varphi}$ shown in Figure (7), at the crack tip. These stresses may then be used quantitatively to describe microscopic affects which contribute to the fracture process in crystalline materials.

The concepts of "Fracture Mechanics", i.e., listed in (i), (ii), and (iii) below, will be used to describe the dependence of the elastic stress state at a crack tip on G . The concepts are categorized as:

- (i) A description of the dependence of the elastic stress state at a crack tip on the stress intensity factor, K .
- (ii) Reversible energy balance, i.e., Griffith analysis, describing a criterion for fracture instability.
- (iii) The dependence of the stress intensity factor, K , on G at the onset of fracture.

These concepts offer a way of describing the fracture process from two viewpoints; strain energy released, G , or stress state at crack tip.

(i) (Stress Intensity Factor K)

Originally, the treatment of the elastic stress state at a crack tip was dealt with by Inglis⁽²⁾ with a more recent and refined treatment by Williams⁽⁹⁾. The equations defining the local elastic stress field near a crack depend on the product of the nominal stress σ on the specimen and the square root of the crack depth, L . The importance of this fact was first appreciated by Irwin⁽¹⁰⁾ who coined the term "Stress Intensity Factor" to emphasize this

fundamental relation. In all cases, the general form of the stress intensity factor, K , is:

$$K = \sigma (\alpha \pi L)^{1/2}, \quad (\text{III.10})$$

where α is a parameter depending on the specimen and crack geometry. A complete listing of expressions for K involving various types of deformation applied to cracks of complicated shapes, in structures of finite width, can be found in the excellent review paper by Paris and Sih⁽¹¹⁾. The local elastic stresses near the crack tip are then written as:

$$\begin{aligned} \text{A. } \sigma_{rr} &= K/(2\pi r)^{1/2} \times F(\varphi) \\ \text{B. } \sigma_{\varphi\varphi} &= K/(2\pi r)^{1/2} \times F'(\varphi) \\ \text{C. } \sigma_{r\varphi} &= K/(2\pi r)^{1/2} \times F''(\varphi) \end{aligned} \quad (\text{III.11})$$

where the angular functions, i.e., $F(\varphi)$, $F'(\varphi)$, and $F''(\varphi)$, depend on the loading or boundary conditions. A description of the variables r and φ in Eqs. (III.11) A, B, and C is shown in Figure (7). Also, the exact angular relationships in these equations can be found in a paper by Williams⁽⁹⁾, and they have been discussed to some extent earlier on page 33 and are listed explicitly in Figure (7). These expressions for the elastic stress state can be used to describe the fracture process if a criterion for crack instability is stated.

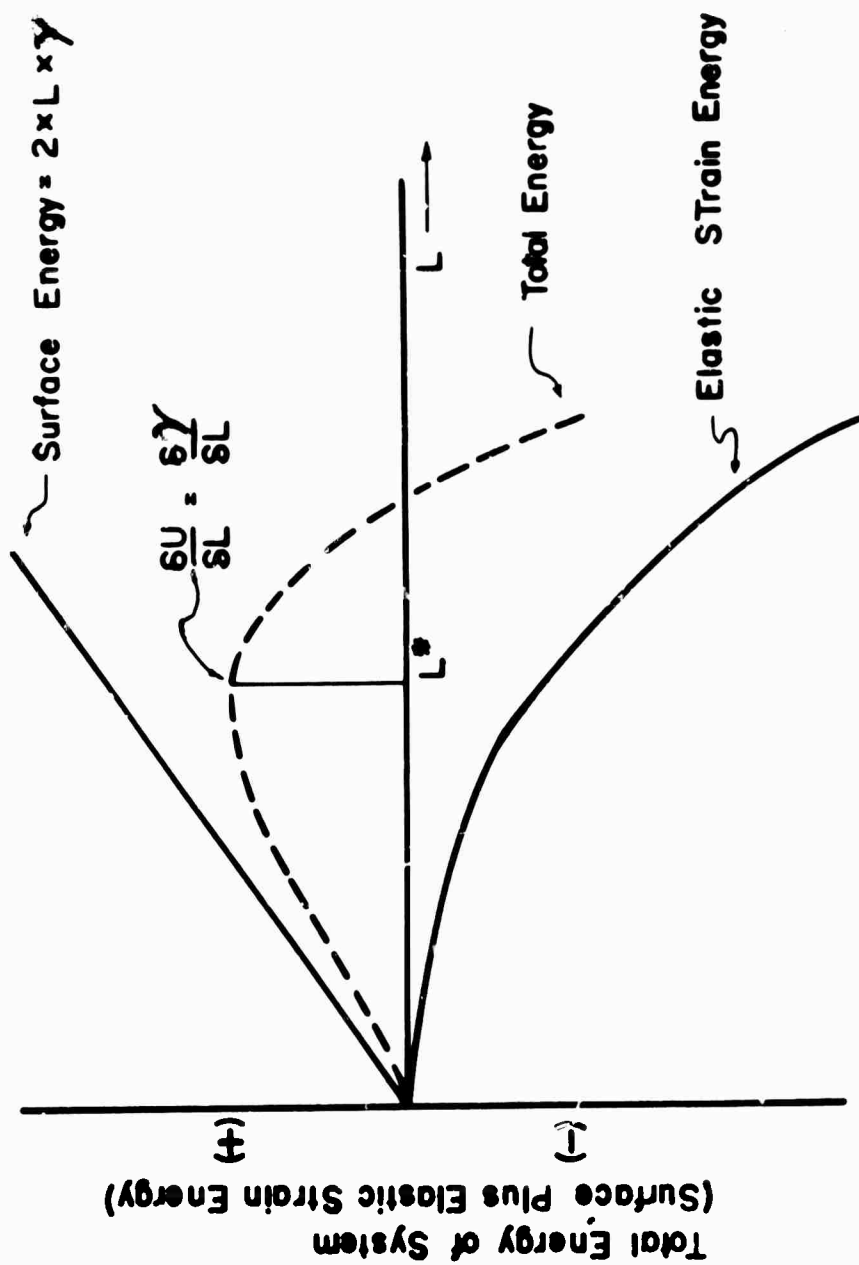
(ii) (Griffith Analysis Describing Fracture Instability)

The relationship between the stress intensity factor and the rate of elastic energy released requires a definition of the stress state prior to the

onset of fracture. The Irwin analysis⁽¹⁰⁾ of fracture proposes that crack propagation of an elliptical elastic crack occurs when the nominal tensile stress σ on the specimen produces a sufficient tensile stress level at the crack tip equal to the inherent fracture stress, σ_F , of the material. The attainment of a critical value σ_F for one of the principal stresses at the crack tip is necessary but not sufficient to cause fracture. In addition, another concept of fracture is needed and was originally derived by Griffith⁽¹²⁾ on the basis of thermodynamic considerations, i.e., first law of thermodynamics. He reasoned that the unstable propagation of a crack must result in a decrease in free energy of the system, i.e., cracked plate under stress with fixed grips, and proposed that a crack would advance when the incremental release or stored elastic strain energy, dU , in a body became greater than the incremental increase of surface energy, $d\gamma$, as new crack surface is created. Thus, fracture instability can occur when the inherent fracture stress, σ_F , is reached with the addition of a simultaneous decrease in energy, i.e., $\frac{\delta U}{\delta L} > \frac{\delta \gamma}{\delta L}$. The graphical representation of this energy criterion is shown in Figure (9), a plot of total energy, i.e., elastic strain energy and surface energy versus crack length L where L^* represents the critical crack length and $L \geq L^*$ results in a decrease in the energy of the system leading to unstable crack propagation.

(iii) (The Dependence of K on G)

The energy balance leading to crack instability at $L = L^*$ can be used to relate the elastic strain energy released, G , and the stress intensity



(Griffith Criterion) Plot of Total Energy Versus Crack Length

Figure 9. Energy criterion for crack instability showing a crack length L^* which can propagate with a decrease in energy.

factor, K . If the functional dependence between U and the nominal stress σ and the crack geometry is known, then the equality $\frac{\delta U}{\delta L} = \frac{\delta \gamma}{\delta L}$ can be combined with Eq. (III.10) to yield the dependence of K on G at the point of fracture.

The stress intensity factor, K , assumes a critical value, K_c , i.e., referred to as "Fracture Toughness" when it is applied at the point of crack instability, and the expression for K_c is

$$K_c = (\alpha \times G \times E_{(y)})^{1/2} \quad (\text{III.12})$$

where $\alpha = 1$ for Plane Stress

$\alpha = 1/(1 - \nu^2)$ for Plane Strain

and ν is Poisson's ratio, i.e., approximately 0.33, and $E_{(y)}$ is Young's Modulus and it is approximately equal to 7.1×10^5 kgms/cm² for aluminum alloys⁽¹⁰³⁾.

Either G or K_c is taken as a measure of the fracture toughness of the material at the point of crack instability. Equation (III.12) shows that an unambiguous determination of K_c from G must be accompanied by a knowledge of the stress state, i.e., plane stress or plane strain, prior to fracture in the test specimen.

The determination of the stress state present in the polycrystal DCB test geometry will be discussed next.

C. Effect of Side Grooves in Promoting Plane Strain Fracture for the DCB Test Geometry:

The plane strain stress state represents the easiest mode for crack propagation. This results because of the tri-axial stress state, i.e. principal stresses are tensile, at the crack tip which suppresses plastic flow compared to the plane stress state by reducing the maximum shear stress. For plane

stress, a bi-axial stress state (tension) exists near the free surface and results in a higher maximum shear stress compared to the plane strain case. This higher shear stress causes a progressive increase in the amount of plastic flow and the extent of plasticity from the free surfaces. This increased plasticity leads to a higher amount of energy released, G , during crack extension and a corresponding increase in the fracture toughness.

Because of the dependence of K_c on geometry, it is advantageous to select K_c in plane strain. This eliminates discrepancies between different test geometries and above all represents a minimum value in G for crack instability. To achieve plane strain in the DCB specimen two alternate geometries are possible:

1. Wide cross-section, B , during fracture.
2. Deep side-grooves down mid-DCB height (see Figure 4) with narrow cross section, B .

Generally, a wide cross-section, B , is employed on test specimens to promote plane strain for the opening mode loading shown in Figure (4). However, to optimize test material use and more importantly to confine crack propagation to the mid-beam height of the DCB specimen, side grooves of various geometries are machined in the specimens. The effect of side grooves on the state of stress at the crack tip and in turn on the fracture toughness has been investigated by Freed and Krafft⁽¹³⁾. They have shown that side grooving promotes plane strain, and also, from fracture mechanics they show K_c to be proportional

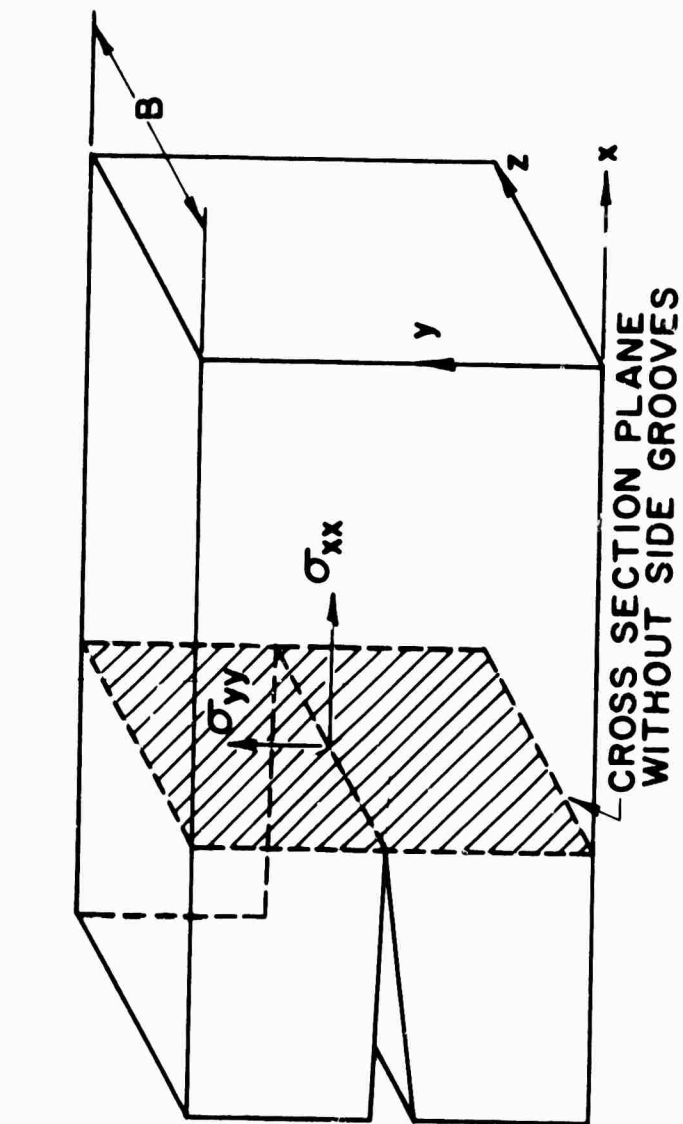
to $(W/B)^m$, a correction factor, where $1/2 \leq m \leq 1$. The acuity of the side groove, up to a radius of curvature of 0.02 in., appears to have little effect on the value of m or on K_c . Logically, it would appear that the presence of side grooves causes a local stress state dependent on the groove geometry which suppresses plastic flow near the free surface and promotes plane strain. The stress states resulting from the side grooves are shown schematically in Figure (10), both cross section and profile views of the polycrystal test geometry depicted in Figure (4). A superposition of the two plane stress states in each of these views leads to a complex tri-axial stress state at the crack tip. This stress state results in a lower maximum shear stress compared to plane stress, and tends to keep elastic contraction in the z direction small, i.e., $\epsilon_{zz} \approx 0$. Thus, the presence of slide grooves $\frac{(W-B)}{2}$ in a cross-section W promote plane strain in the cross-section B .

To insure a plane strain stress state of the DCB test geometry with side grooves, it is necessary to evaluate the fracture toughness, i.e., G corresponding to K_c , as a function of W and B . When G becomes independent of the depth of side grooves $\frac{(W-B)}{2}$, a minimum value of G is reached, and the stress state is plane strain. This approach has been used experimentally to optimize material and determine the exact geometry of a DCB specimen for plane strain fracture toughness testing.

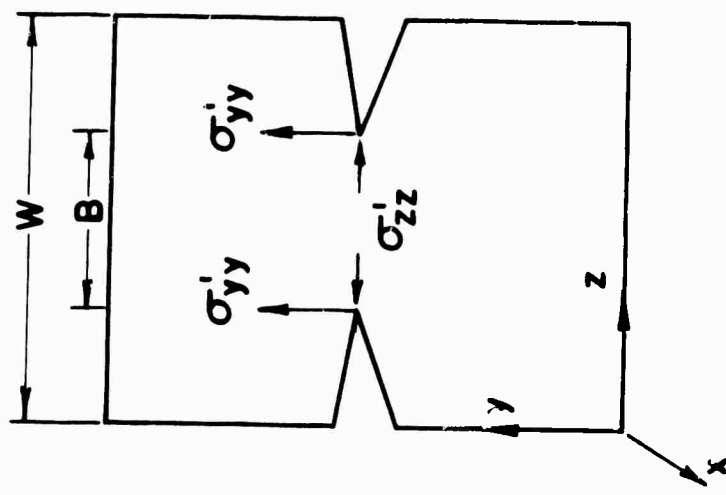
D. Stress Analysis of DCB Geometry:

Having fixed the stress state (plane strain) for crack instability, a

PROFILE VIEW OF DCB GEOMETRY



CROSS SECTION PLANE
WITH SIDE GROOVES



PLANE STRESS IN X-Y PLANE

PLANE STRESS IN Y-Z PLANE

Figure 10. The effect of side-grooves in promoting plane strain across crack front B, i.e. superposition of the plane stress states in the x-y and y-z planes.

determination of the stress intensity factor K at the point of fracture, unambiguously defines the fracture toughness K_c . As mentioned earlier, Srawley and Gross⁽⁸⁾ used an elastic stress analysis to determine the stress field at the crack tip in a DCB specimen. Their analysis yields the following expression for the stress intensity factor which produces fracture under an applied force F for a crack length L :

$$K_{cc} = 3.46 \frac{F}{B \cdot H^{3/2}} [L + 0.7 \times H] . \quad (\text{III.13})$$

Equation (III.13) is applicable to a uniform DCB specimen, i.e., shown in Figure (5), without the presence of side grooves. The addition of side grooves to a DCB specimen should not change the functional dependence of G or K_c on the parameters force F and crack length L in Eqs. (III.8), (III.9), or (III.13). The functional dependence will remain invariant in these equations, but the equality of these equations (involving G and K_c) will depend on a constant. The constant in turn is related directly to the side groove geometry (discussed by Freed and Krafft⁽¹³⁾). Provided a geometric constant is evaluated, the equations developed for plane DCB specimens without side grooves are also applicable to DCB specimens with side grooves. For a fixed side groove geometry, the geometric constant can be determined by finding the ratio of K_c/K_{cc} from Eqs. (III.12) and (III.13) -

$$\frac{K_c \text{ (Energy Analysis)}}{K_{cc} \text{ (Stress Analysis)}} = \Delta \text{ (Geometric Constant)} . \quad (\text{III.14})$$

Knowing the stress state (plane strain), an experimental determination of the fracture toughness, K_c , is made through Eq. (III.12). The calculated value of K_c from G is based on the energy approach, i.e., Eqs. (III.4) and (III.12), and takes into account the specimen test geometry (side grooves). Corresponding to this experimental value of K_c , a stress intensity factor is calculated from Eq. (III.13). This calculated value of fracture toughness, K_{cc} , is for a DCB cross section B, and doesn't take side grooves into account. The geometric constant, Δ , Eq. (III.14), is a ratio of fracture toughness values determined with and without side grooves in the DCB geometry. The Srawley-Gross⁽⁸⁾ expression, Eq. (III.13), for the stress intensity factor can be modified for side grooves and takes the form

$$K'_{(cc)} = 3.46 \times \frac{F \cdot \Delta}{B \cdot H^{3/2}} [L + 0.7 \times H]. \quad (\text{III.15})$$

Knowing the constant, Δ , for the side-notched, DCB test geometry, Eq. (III.15) can be used to calculate successive values of K'_{cc} during crack propagation by continuously monitoring load F and crack length L . Thus, two Eqs. (III.12) and (III.15) can be used to determine equivalent stress intensity factors, i.e., K_c or K'_{cc} , causing fracture at a crack velocity, V .

The concepts and equations discussed in this section have shown that the elastic solutions to crack instability based on either an energy or stress analysis are equally valid. The energy approach lends itself to an experimental determination of the quantities G and K_c (Eqs. (III.4) and (III.12)), while

the stress analysis (Eq. (III.15)) is directly applicable to calculating K'_{cc} in the DCB geometry. Equation (III.15) gives a continuous measure of the decreasing stress state at the crack tip for crack extension under fixed grip conditions in the side-grooved DCB geometry. The actual experimental determination of the quantities G , K_c' , and $K'_{(cc)}$ will be discussed in the next section, entitled Data.

IV. DataA. Raw Data:

Tensile tests were used to characterize the bulk mechanical properties of different microstructures in the Al-15 wt % Zn system. Standard tensile specimens with a 2.5 in. gage length and 0.5 in. by 0.040 in. cross-section were used in the mechanical tests. A 0.2% offset in strain was used to determine the yield stress of a particular microstructure. Figures (11) and (12) are plots of these results, and yield stress versus aging time at 155°C and at 25°C (Room Temperature) is shown in both plots. Figure (6) shows the thermal history, i.e., heat treating and aging conditions, of the microstructures tested. These tensile tests for characterizing microstructure were a prelude to the more important mechanical DCB tests, which related cracking kinetics to the elastic stress field parameter, K_c or K'_{cc} , i.e., Eqs. (III.12) and (III.15). The material constants, ν , Poisson's ratio, and $E_{(y)}$, Young's Modulus necessary in calculations involving K_c and K'_{cc} were not measured experimentally. The values of $\nu = 0.33$ and $E_{(y)} = 7.1 \times 10^5$ kgs/cm² are referenced for Al alloys⁽¹⁰³⁾. These values are insensitive to microstructural changes and are assumed to apply to the microstructures tested in the Al-15 wt % Zn system.

As previously mentioned, the experimental parameters measured in the DCB test are force F , crack length L , time t , and deflection δ . These quantities with the exception of deflection ($\delta = \text{constant}$) are continuously monitored during the polycrystal (Figure (4)) and bi-crystal (Figure (5)) tests. The

tabulation of this data for each of the polycrystal and bi-crystal tests is shown in Appendix I-A. The heat treatment and critical dimensions of the DCB geometry (H , B , W , δ) are listed above the tabulated values (F , L , t). The results for polycrystal tests are included in Table Nos. 1 to 20 inclusive. Bi-crystal results start in Table 21 and run through Table 30. The experimental parameters listed in these tables represent distinct values for the different microstructures tested and can be reduced to meaningful values of fracture toughness K_c , elastic strain energy released G , and crack velocity, V . It should be emphasized that the tabulated values of F , L , and δ represent possible calibration curves for G versus L which are independent of the cracking mechanism, i.e., dF/dL versus L at a constant δ for the DCB specimens shown in Figures (4) and (5). Thus, provided the appropriate geometry is maintained, this tabulated data is equally valid for calculating G or K_c in any material that is linearly elastic.

B. Reduced Data:

1. Polycrystal Data

The reduction of the raw data for polycrystal specimens to values of G , K_c and cracking velocity V is shown in Appendix I-B. In addition, the tables in Appendix I-B have column headings of K_{cc} , a calculated fracture toughness Eq. (III.13), and Δ , the geometric constant for a notched DCB specimen Eq. (III.14). The amount of raw data in Appendix I-A is too great to consider individual calculations of G , K_c , K_{cc} , and V for each microstructure tested.

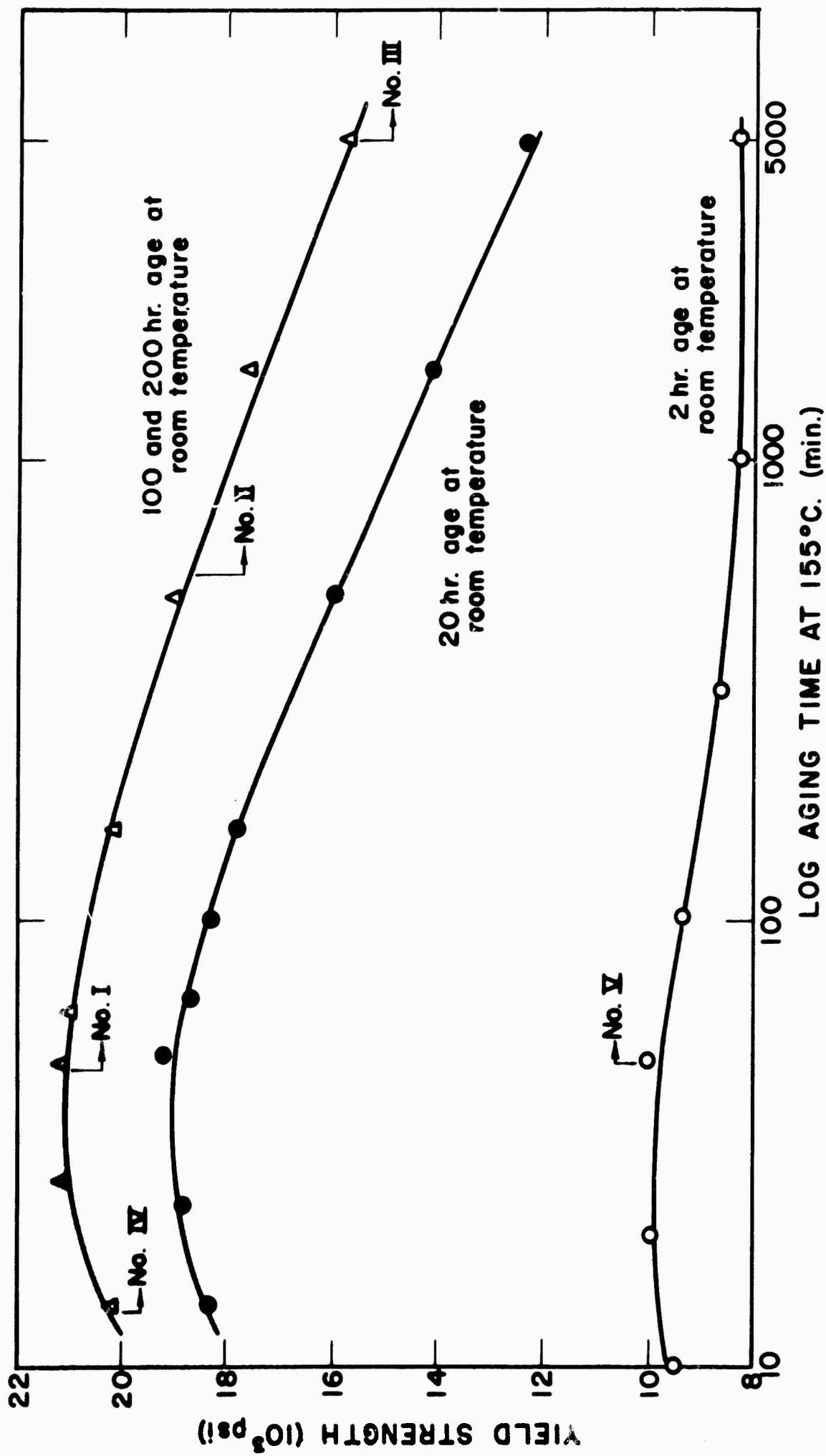


Figure 11. Yield strength versus aging time at 155°C prior to a quench and further age at room temperature, 25°C, for 2 hrs., 20 hrs. and 100 hrs.; the microstructures tested are labeled in Roman Numerals.

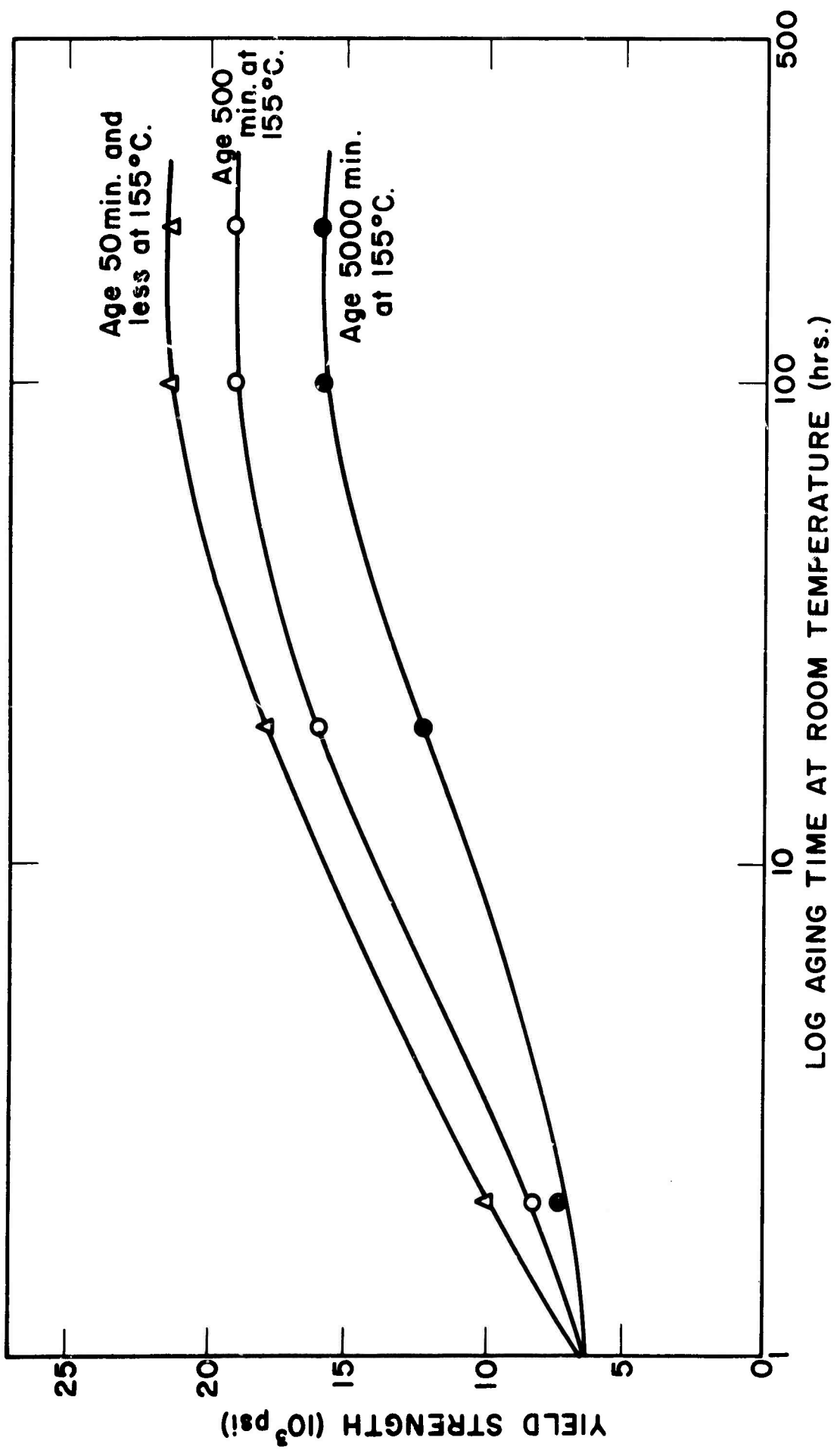


Figure 12. Yield strength versus aging at room temperature, 25°C, following an aging treatment at 155°C for different times; 50 min., 500 min., and 5000 min.

As a result, the method of reducing the data to the values tabulated in Appendix I-B will be described by analyzing typical raw data for DCB specimen No. 7 polycrystal (Table 10). Figures (13) and (14) are plots of F versus L and L versus t for number 7 polycrystal. It is immediately apparent from these figures that a large number of experimental points is necessary in order to draw smooth curves. All curves as exemplified by Figures (13) and (14) were traced by hand and slopes, $(dF/dL)_L$ and $(dL/dt)_L$, were drawn manually as averages over an incremental crack advance length, $dL \approx 0.3$ cm. This increment was chosen to average the irregular motion of crack extension resulting from the intergranular fracture of the equi-axed grain structure, i.e. grain diameter of approximately 1 mm. can lead to an error in the measurement of crack length by approximately $\pm .05$ cm. An exception to averaging the data over a crack increment of .3 cm was made when the crack velocity, $(dL/dt)_L$, became small, i.e., $(dL/dt)_L \lesssim 10^{-3}$ cm/min. At these small crack velocities an average increment of .1 or .2 cm was used, and the experimental uncertainty in crack velocity was greater than data averaged over an increment of .3 cm.

This method of measuring the slopes $(dF/dL)_L$ and $(dL/dt)_L$ led to an experimental uncertainty in the calculated value of G by approximately $\pm 20\%$. Calculated values of crack velocity, V , were uncertain to approximately $\pm 15\%$ of the measured value when an averaging increment of 0.3 cm was used. However, the uncertainty in V increased to $\pm 25\% - \pm 50\%$ when velocities $\lesssim 10^{-3}$ cm/min were measured. When analyzing Figure (13), two features are noticed:

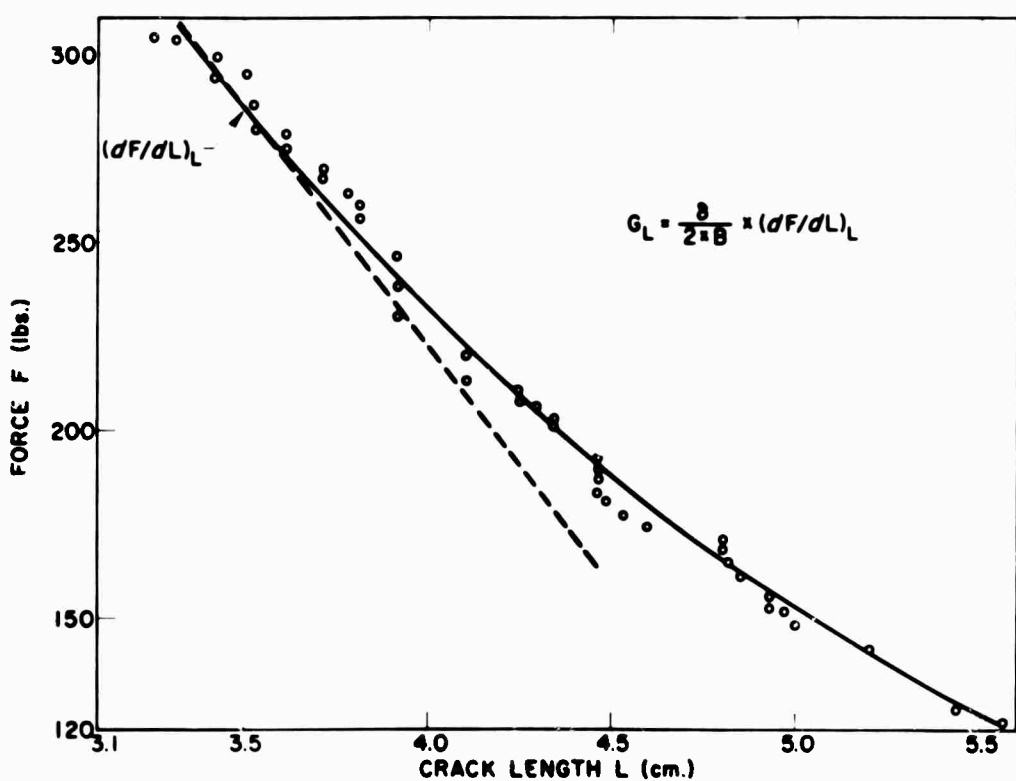


Figure 13: Load relaxation F versus cracking length L during crack propagation in DCB specimen No. 7 polycrystal.

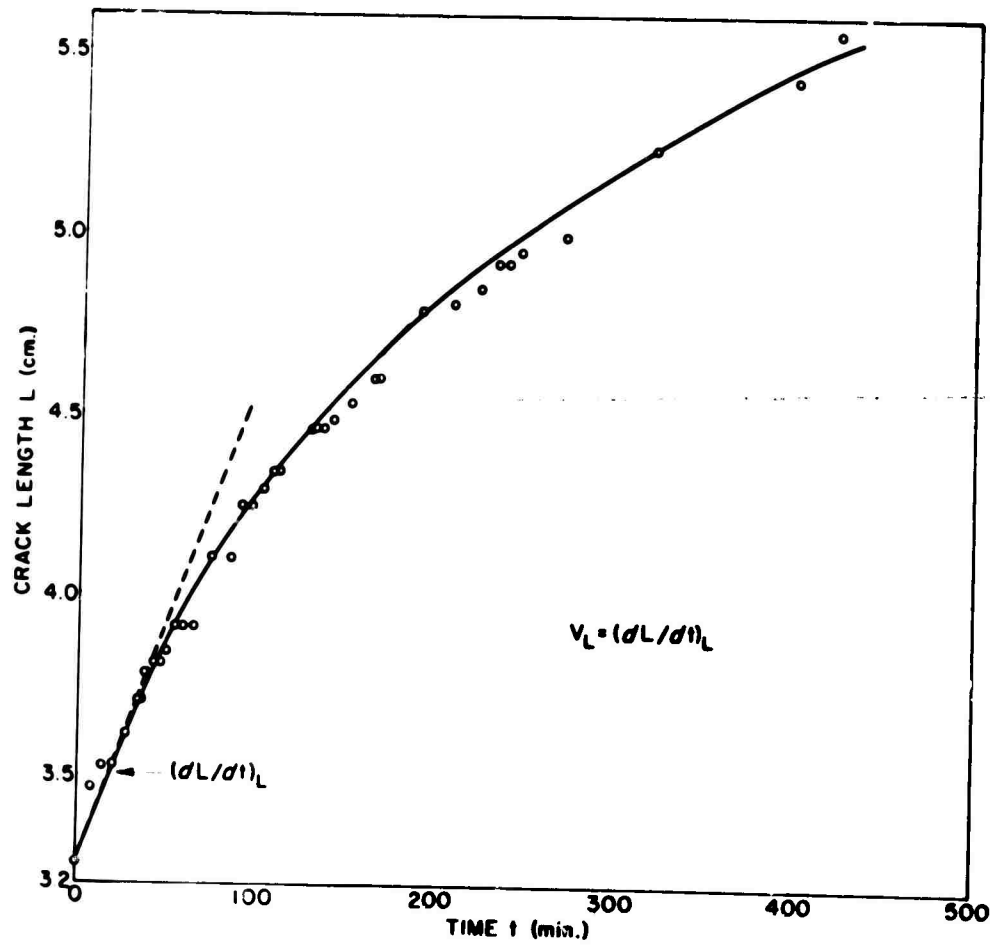


Figure 14. Crack length L versus cracking time t for crack propagation in DCB specimen No. 7 polycrystal.

$dF/dL < 0$ (negative slope) and $d^2F/dL^2 > 0$ (concave up). Both of these trends can be predicted from linear elasticity⁽¹⁸⁾, and $d^2F/dL^2 > 0$ indicates that G and K_C (see Eqs. (III.4) and (III.12)) decrease with an increasing crack length L . Thus, as crack extension occurs the driving force G for crack propagation decreases, and a decreasing crack velocity should be observed. This is indeed the case in Figure (14), where $d^2L/dt^2 = dV/dt < 0$ (deceleration).

The determination of G is found through Eq. (III.4), i.e., shown in Figure (13). The experimental value of K_C corresponding to $(dF/dL)_L$ is then calculated through Eq. (III.12), i.e. the plane strain value. At this point of crack extension, L , in the DCB specimen, Figure (14) can be used to compute crack velocity $(dL/dt)_L$. Thus, in principle three experimental parameters G , K_C , and V can be continuously calculated during crack propagation. However, it is difficult to experimentally determine continuous corresponding slopes, $(dF/dL)_L$ and $(dL/dt)_L$, from Figures (13) and (14), and for this reason it is desirable to have a closed form expression (in terms of F and L) for G or K_C . With a closed form expression, i.e., $K_C = \text{Function}[F, L]$, the crack velocity $(dL/dt)_L$ from Figure (14) could be related to a force F and crack length L in Figure (13) and thereby to K_C . Knowing F and L would be sufficient to calculating K_C , and a direct determination of the slope $(dF/dL)_L$ would be eliminated. The procedure for calculating $K_C = \text{Function}[F, L]$ is outlined as:

- (1) Calculation of G_L from $(dF/dL)_L$; see Figure (13).
- (2) Calculation of K_C from G_L ; Eq. (III.12).

is minimized. From this basis it can be shown that if the crack remains within the central tenth of the specimen, the error in the elastic strain energy release rate, G , will not exceed 6%^(f). Typically, for the geometry used in this problem, a crack deviation of ± 0.12 cm from the mid-beam height could be tolerated with the error in G not exceeding 6%. It should also be noted that aside from causing an error in G , a sufficient deviation will cause the crack to veer completely out of the desired mid-plane for extension and break off one of the DCB specimen arms. A complete understanding of this tendency requires an analysis of the stresses that are perpendicular and parallel to the crack plane. This will not be discussed, but the dimensions of the DCB specimens in this experimental program represent optimum values for minimizing crack deviation and DCB failure through the arms.

The other major source of error is introduced when the advancing crack encounters the effect of the free surface at $L = L_o$ (Figure (4)). Anomalous measurements of G in Appendix I-B are denoted by an asterisk, and it is noted that these values occur at $L/L_o \approx 0.8$. These values indicate that at approximately 1.2 cm, or the width of the un-notched DCB specimen, the free surface is influencing values of F and L ⁽⁸⁾. The data indicates that dF/dL tends to increase as $L \rightarrow L_o$, and the corresponding crack velocity V decreases. Because of this effect, measurements of G and V were not considered valid after $L/L_o \approx 0.8$.

V. Results

A. Plane Strain DCB Test Geometry:

The measured value of fracture toughness, i.e., G or K_c , is very much dependent on the stress state (bi-axial or tri-axial) at the crack tip of the DCB test specimen. Whether fracture occurs under plane stress or plane strain depends on the specimen thickness B (cross section at advancing crack front shown in Figures (4) and (5)). If the specimen is thin cracking occurs under a condition of plane stress, i.e. principal stress normal to surface in thickness direction is approximately zero, and for a thick specimen contraction in the thickness direction is constrained by the surrounding elastic material. The change from plane stress to plane strain occurs abruptly as the specimen thickness is increased, leading to the concept of a thickness transition when G is plotted against thickness, B . With the presence of side grooves the transition becomes a function of (B/W) , i.e., the ratio of notched to un-notched thickness. Within this transition range, the material toughness, G , undergoes a sharp change, corresponding to plastic versus brittle fracture behavior. A minimum value of G is then associated with the specimen geometry, (B/W) , corresponding to brittle behavior, and the plane strain stress state in Eq. (III.12) is used to relate this G to K_c .

The effect of side groove depth on this transition range for the measured value of G is shown for a commercial (Al-Zn-Mg alloy) 7075-T651 in Figure (16). It is apparent from this figure that even very modest side grooves

(3) Calculation of K_{cc} for a given F and L using DCB geometry without side-grooves; Eq. (III.13).

(4) Finding geometric constant, $\Delta = K_c / K_{cc}$ Eq. (III.14).

(5) $K'_{cc} = K_c = \Delta \times K_{cc}$ Eq. (III.15).

Sample calculations of these five steps and the additional calculation of crack velocity $(dL/dt)_L$ are shown in Appendix I-D. These calculations were carried out for all the DCB specimens tested and are listed in separate columns in Appendix I-B. From these calculations the geometric constant Δ was found to be $0.64 \pm .08$ for $B = 0.42$ cm. This value of Δ was used in Eq. (III.15) to determine the dependence of K_c on F and L for the side-notched DCB test geometry.

$$K'_{cc} = K_c = \frac{2.22 \times F}{B \times H^{3/2}} [L + 0.7 \times H] \quad (IV.1)$$

Eq. (IV.1), for $K'_{cc} = K_c$, was then used to calculate values of K'_{cc} when the curvature, i.e., d^2F/dL^2 , was small for a plot of F versus L , and the change in slope, dF/dL , was difficult to measure experimentally. Thus, both Eqs. (III.12) and (IV.1) were used to calculate the stress intensity factor, K_c or K'_{cc} , causing fracture at a crack velocity, V .

2. Bi-crystal Data

The reduced bi-crystal data, i.e. G and V , shown in Appendix I-C follows a similar format to the polycrystal data shown in Appendix I-B. The difference between the polycrystal and bi-crystal data is that only one value

of elastic strain energy released, G , and crack velocity, V , is calculated during a bi-crystal test. Because of a total fracture length between 0.3 to 0.5 cm., plots of F versus L and L versus t for bi-crystal tests are essentially linear. Thus, an average G value over the entire fracture length may be computed from Eq. (III.4), where $(dF/dL) \approx (\Delta F/\Delta L)$. Similary, an average crack velocity V is calculated as $(\Delta L/\Delta t)$ over the same fracture increment as the average G .

The thickness, B , of all bi-crystal specimens was less than 0.040 in., and no attempt was made to calculate a K_c value. This thickness indicates a probable state of plane stress at the bi-crystal crack tip, and comparisons of K_c value to plane strain polycrystal tests would not be valid. However, the average G and V values for the different bi-crystal tests can be compared among the different bi-crystal orientations (Appendix I-C). These values can also be used when comparing cracking susceptibility between bi-crystal and polycrystal specimens.

C. Bi-crystal Orientations:

The added benefit in studying bi-crystal specimens over polycrystal specimens is the well defined intergranular fracture path. The crystallographic orientation of the grain boundary in a bi-crystal is well known when compared to arbitrarily oriented grains in a polycrystallizing aggregate. To define this added variable of grain boundary orientation, five unique angles are needed (5 degrees of freedom), (Ref. 27). Three of the degrees of freedom are associated with the relative orientations of the two lattices on either side of the boundary,

and two degrees are required to specify the local inclination of the boundary surface relative to one of these lattices. The angles selected to define grain boundary orientations in the bi-crystals tested are: $\alpha_{(100)}$, $\beta_{(100)}$, $\gamma_{(111)}$, Δ , and ϵ . Figure (15) is a stereographic plot of these five angles and may be used as a visual aid with the following description. The first two, $\alpha_{(100)}$ and $\beta_{(100)}$, are the angles necessary to bring the (100) pole of one grain into coincidence with the other grain's (100) pole. $\gamma_{(111)}$ is then the measured angle between (111) poles in each grain when (100) poles are coincident. The last two angles, Δ and ϵ , are necessary to bring the grain boundary normal into coincidence with the (100) poles. These five angles have been measured from the plotted bi-crystal orientations on stereographic projections and are listed in Appendix I-C along with the corresponding average V and G values.

D. Source of Error:

Having discussed the reduction of data, brief mention will be made as to the criteria adopted in discriminating between valid data points and errors introduced through the test geometry. Aside from errors introduced through measuring the DCB parameters (δ , F, L, t), the major error is introduced by deviations of the crack from the center, or mid-beam height (Figure (4)). For a given δ , the stored strain energy for a given crack length in the DCB specimen is a maximum if the crack runs in the center. However, if the crack divides the specimen into beams of unequal height, then these beams will take up unequal parts of the total separation δ , in such a way that the sum of the strain energies

Characterizing Bi Crystal Orientation

Five Degrees of Freedom

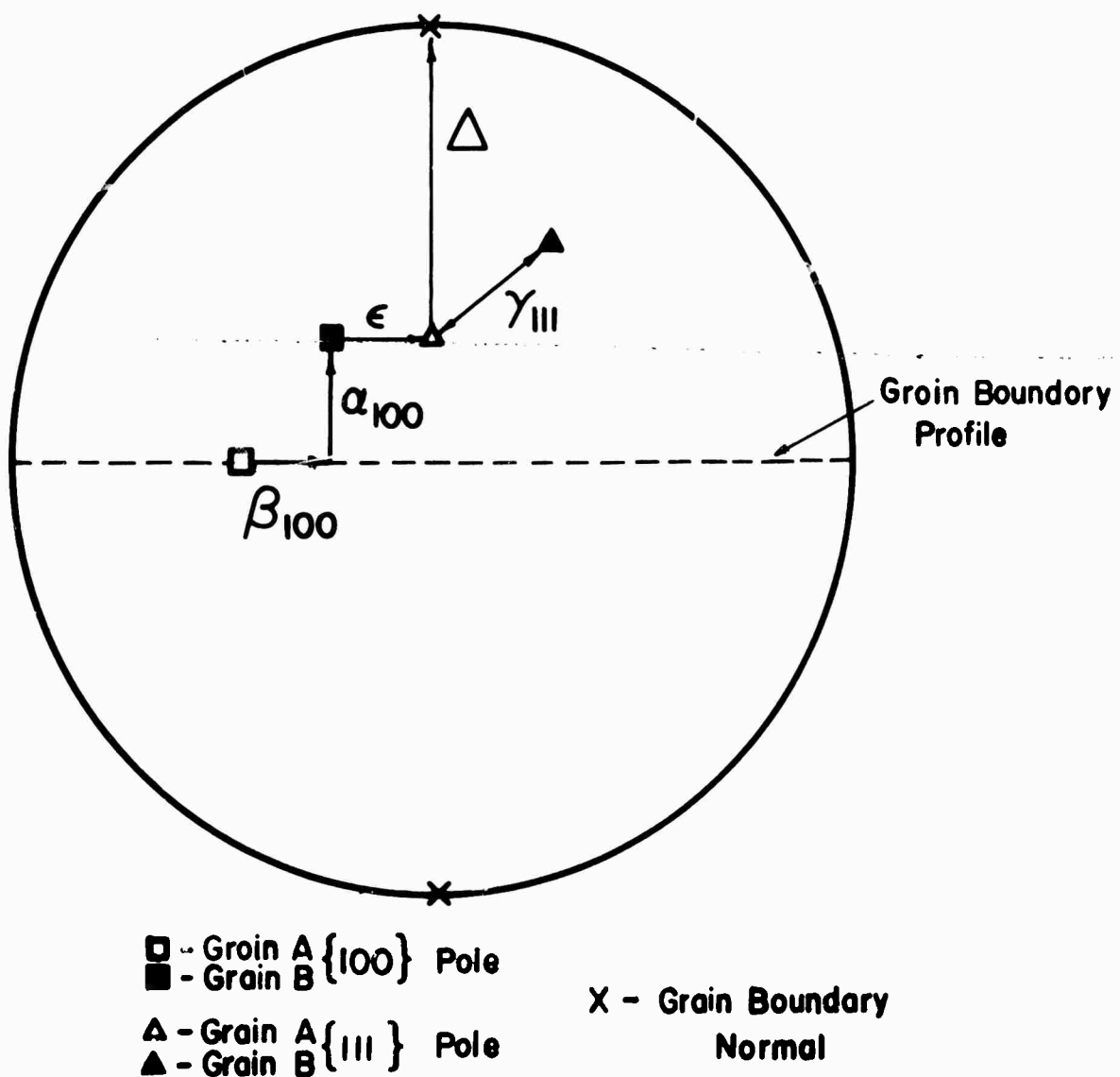


Figure 15. Specifying bi-crystal orientation with five angles; $\alpha_{100}, \beta_{100}, \gamma_{111}, \epsilon, \Delta$.

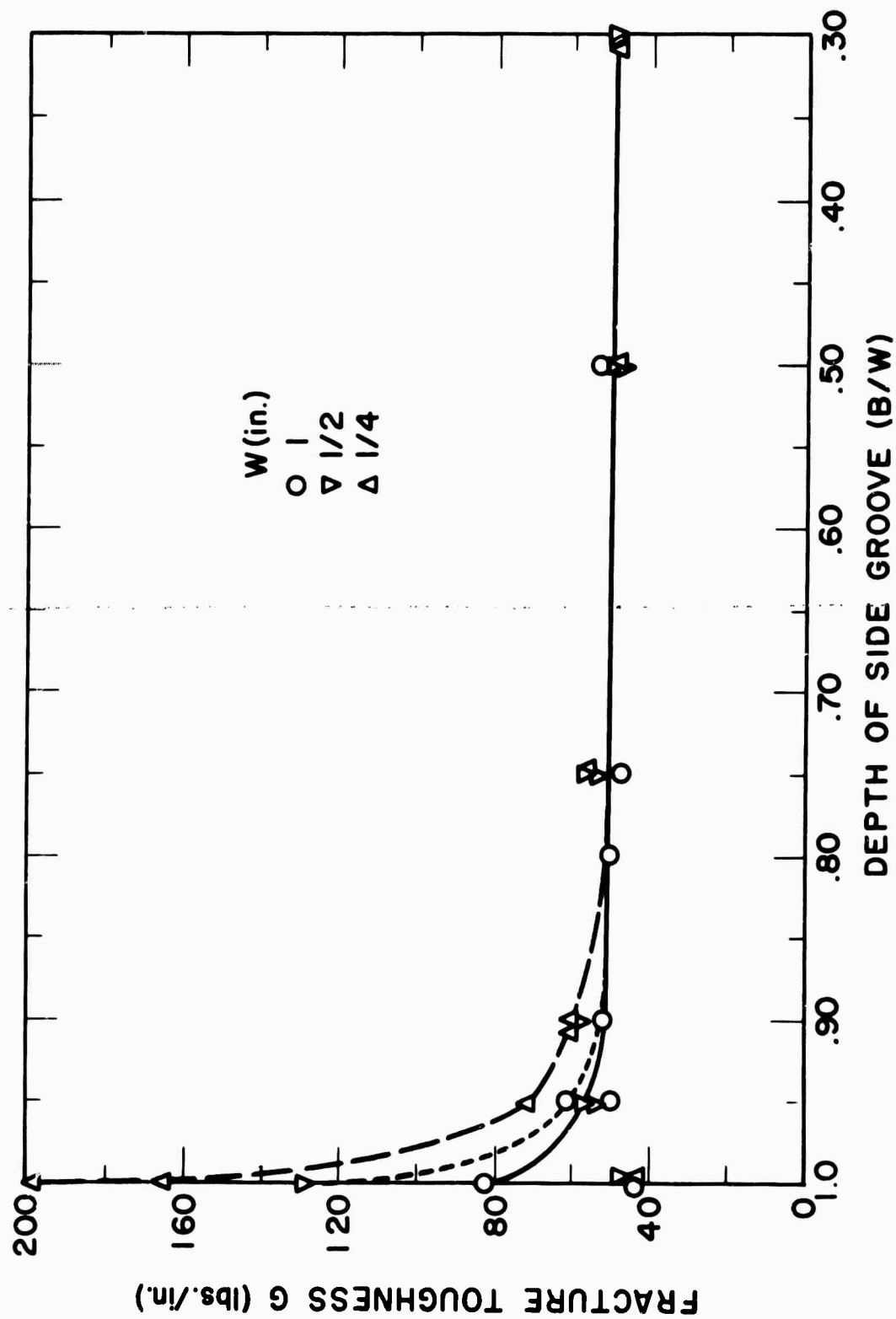


Figure 16. Fracture toughness G versus depth of side groove (B/W) for a commercial Al-5.6% Zn - 2.3% Mg alloy; plane strain fracture toughness is ≈ 50 lbs/in.

($B/W \sim 0.95$) markedly lowered the measured toughness: the largest decrease occurring for the thinnest specimens ($W = 1/4$ in.)⁽¹⁹⁾. When the ratio of B/W was equal to 0.8 or less, all three specimen thicknesses yielded $G = 50 \pm 4$ lb/in, the plane strain toughness of this material. Also, the fact that the fracture toughness remained constant over the broad range $.3 \leq B/W \leq .9$ suggests that once the grooves are deep enough to promote complete plane strain fracture, the toughness value is not influenced by further side grooving.

Because G or K_c depends on the elastic constraint, an advancing crack does not have a plane front perpendicular to the specimen surface except in very brittle materials. The crack travels fastest at the mid-thickness of the specimen where the elastic restraint is greatest, and the behavior is brittle. As the crack front approaches the specimen surfaces, the elastic restraint is greatly reduced and fracture changes from plane strain to plane stress. This usually accounts for the formation of a shear lip or ductile fracture near the specimen surfaces. Thus, often the appearance of the fracture surface gives an indication as to the state of stress⁽²⁰⁾. With these concepts outlined, it is reasonable to expect certain trends when testing the DCB specimens with various notch geometries.

Figure (17) is a plot of crack velocity V versus an "Apparent" plane strain stress intensity factor K_c for intergranular fracture in air. The word "Apparent" is used because the plane strain value of K_c is used in plotting V versus K_c irrespective of the DCB notch geometry. This figure represents points

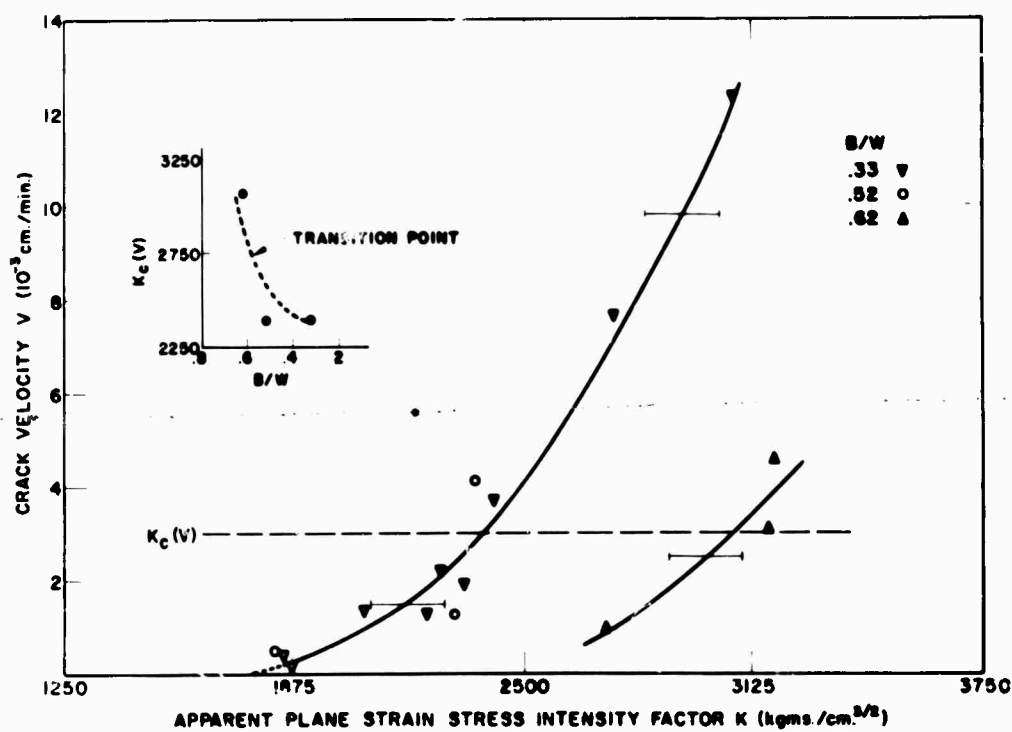


Figure 17. Crack velocity for intergranular fracture in air versus apparent plane strain stress intensity factor; three side-groove geometries, i.e. $B/W = .33, .52, .62$, are plotted with the transition point for plane strain at $B/W \approx .52$.

from three distinct DCB notch geometries, i.e., $(B/W) = .33, .52$, and $.62$, and the plotted values of V and K_c correspond to DCB polycrystal test Nos. 1, 2, and 12 (see Appendix I-B). A description of the microstructures tested will be discussed in section VI.A and B, and at present it is sufficient to state that the experimental points (V and K_c) in Figure (17) are all for the same microstructure, i.e., same volume fraction of G.P. zones in the matrix.

Before discussing the implications of this figure on the state of stress for a particular notch geometry, the importance of a dependence of crack velocity V on the stress intensity factor K_c should be noted. Figure (17) and all subsequent data of this type show a distinct functional dependence for intergranular fracture in air between crack velocity and stress intensity factor.

Figure (17) indicates a range of fracture toughness values, K_c , leading to "stable crack growth" at a velocity, V . However, most literature on fracture mechanics defines K_c or G as the value of fracture toughness at the onset of rapid or "unstable crack propagation"⁽¹⁰⁴⁾. Such a definition is too vague as an operational definition for testing purposes, and a great deal of ambiguity exists in describing the phase, "unstable crack propagation". Figure (9) shows the general criterion adopted for defining the condition at crack instability. The previous discussion of Figure (9), i.e., Griffith analysis, page 42, shows that K_c is defined at the point where $\frac{\delta U}{\delta L} = \frac{\delta \gamma}{\delta L}$. This energy balance doesn't take into account the time required for crack advance, i.e., how fast does the crack propagate? Thus, the present definition of a unique fracture toughness

K_c (independent of time which describes "unstable crack propagation") is insufficient to account for the dependence in Figure (17) of V or K_c . However, by specifying the crack velocity V , a unique value of the stress intensity factor K_c causing fracture at this velocity is determined. This unique value will be referred to as $K_c(V)$.

Values of $K_c(V)$ can now be used in determining the transition from plane stress to plane strain for different notch geometries. By drawing an iso-velocity contour (horizontal line) in Figure (17), the intersecting values of $K_c(V)$, for different values of (B/W) , can be compared. These intersecting values of $K_c(V)$ versus B/W are also plotted in Figure (17) and a distinct transition point is shown at $(B/W) \approx 0.55$. Thus, DCB notch geometries of $B/W \leq .55$ will yield a plane strain value of the stress intensity factor $K_c(V)$.

Having established a plane strain criterion for the DCB test geometry, it would be advantageous to determine a value of $K_c(V)$ which is the inherent fracture toughness of the material and microstructure tested. A logical definition for a unique value of $K_c(V)$, i.e., independent of the time to fracture and only a function of the properties of the material being tested is: $K_c(V)$ as $V \rightarrow 0$. The value of $K_c(V \rightarrow 0)$ will be referred to as the "Threshold Toughness". This definition eliminates the dependence of K_c on time, and the ambiguity in defining "stable or unstable crack growth". Materials that don't exhibit "stable" or time dependent fracture, i.e., most common materials aside from polymers, have a measured fracture toughness K_c independent of crack velocity. However,

it can be rationalized that this time independent K_c (fracture toughness) is approximately equivalent to the threshold toughness $K_c(V \rightarrow 0)$; for if a material exhibits no apparent crack growth below a K_c value then the crack velocity below this fracture toughness is assumed to be zero.

By defining the point of crack instability on Figure (17) at zero crack velocity, a unique point of $K_c(V \rightarrow 0)$ is determined which can be considered equivalent to the normally quoted time independent, fracture toughness of a material. The extrapolated value of stress intensity factor, $K_c(V)$, to zero velocity on Figure (17) yields $K_c(V \rightarrow 0) \approx 1600 \text{ kgs/cm}^{3/2}$ or $G \approx 3.3 \text{ kgs/cm}$. This is smaller but comparable to the measured value of $G \approx 9 \text{ kgs/cm}$ for the commercial (Al-Zn-Mg) alloy shown in Figure (16). However, this comparison between fracture toughness and threshold toughness should only serve as a guide in the definition of $K_c(V \rightarrow 0)$, since a difference in alloy composition and microstructure exists between Figures (16) and (17).

The previous discussion applies to the plane strain stress state for intergranular fracture in air of polycrystal specimens. However, this experimental program has also dealt with bi-crystals which were relatively thin and were not side grooved. Thus, it is plausible to expect a plane stress state to exist in these tests. This precludes a comparison of $K_c(V)$ values between polycrystal and bi-crystal specimens. However, when testing bi-crystals in 0.5M NaCl at low stress values, no ductile rupture was apparent on the fracture surfaces. At these low stresses (no plastic flow), it becomes feasible to compare $G(V)$,

values between polycrystal and bi-crystal specimens. The comparison between the values of G for the two specimens is made at a constant crack velocity and in the absence of plastic flow. However, the values of G are for different stress states: plane stress for bi-crystals and plane strain for polycrystals. Thus, the comparison is valid provided the stress state has no effect on the chemical reaction at the crack tip when testing in the corrosive environment. It should be mentioned that the stress state does play a pronounced effect in the static fatigue of some glasses^(21,22). With this reservation, the comparison between G values has been made and will be discussed in a later section,

V.H.

B. Slow Crack Growth in Air, Distilled H_2O , and 0.5 Molar NaCl:

With the exception of creep rupture, most materials don't exhibit time dependent fracture when testing under relatively low static stress values in air. The ambient environment of air precludes any stress corrosion cracking phenomenon such as hydrogen embrittlement⁽²³⁾ or the static fatigue of glass⁽²⁴⁾. Thus, air is considered as an inert atmosphere, provided the moisture content is low. If an additional restriction of testing below $0.3 \sim 0.4 T_M$ (homologous temperature) is put on the system, failure due to creep rupture can be discounted⁽²⁵⁾. Since all fracture tests on the Al-Zn system were carried out at $.34 T_M$, this would eliminate or reduce creep rupture due to thermal activation. Having eliminated stress corrosion cracking and creep rupture, the slow intergranular crack growth observed in air for the Al-Zn system would indicate a new

division for classifying intergranular fracture. The interpretation and description of this type of intergranular fracture will be discussed in detail in section VIII, and it will be designated as "Slip Induced Intergranular Fracture".

The test results which establish this supposedly new type of fracture are shown in Figure (18). This figure is a plot of crack velocity versus the stress intensity factor K_C for intergranular fracture in air, distilled H_2O , and 0.5 molar NaCl solution. Obviously, to distinguish between the cracking kinetics of these three environments, the microstructure was held constant in these tests. All specimens were heat treated and then aged at 155°C for 50 min.; followed by a 100 hr. age at room temperature prior to testing. The most noticeable feature of Figure (18) is a decrease in the susceptibility to intergranular fracture when changing test environments from 0.5M NaCl \rightarrow distilled $H_2O \rightarrow$ air. This shift is seen quantitatively by drawing an iso-velocity contour through the three curves at a crack velocity equal to 10^{-3} cm/min. The progressive increase in $K_C(V)$ for these three environments is then 310 $\text{kgs-cm}^{-3/2}$ (NaCl), 1420 $\text{kgs-cm}^{-3/2}$ (distilled H_2O), and 2101 $\text{kgs-cm}^{-3/2}$ (air). These values of $K_C(V)$ from Figure (18) tend to indicate that cracking in air represents a true base level, i.e., no environmental effects, for intergranular fracture in this alloy system. If moisture in air played a significant part in the fracture process, it would be expected that the curves for distilled H_2O and air would be coincident with one another, and this isn't the case. Conclusive proof for air being a base level of cracking would necessitate carrying out a

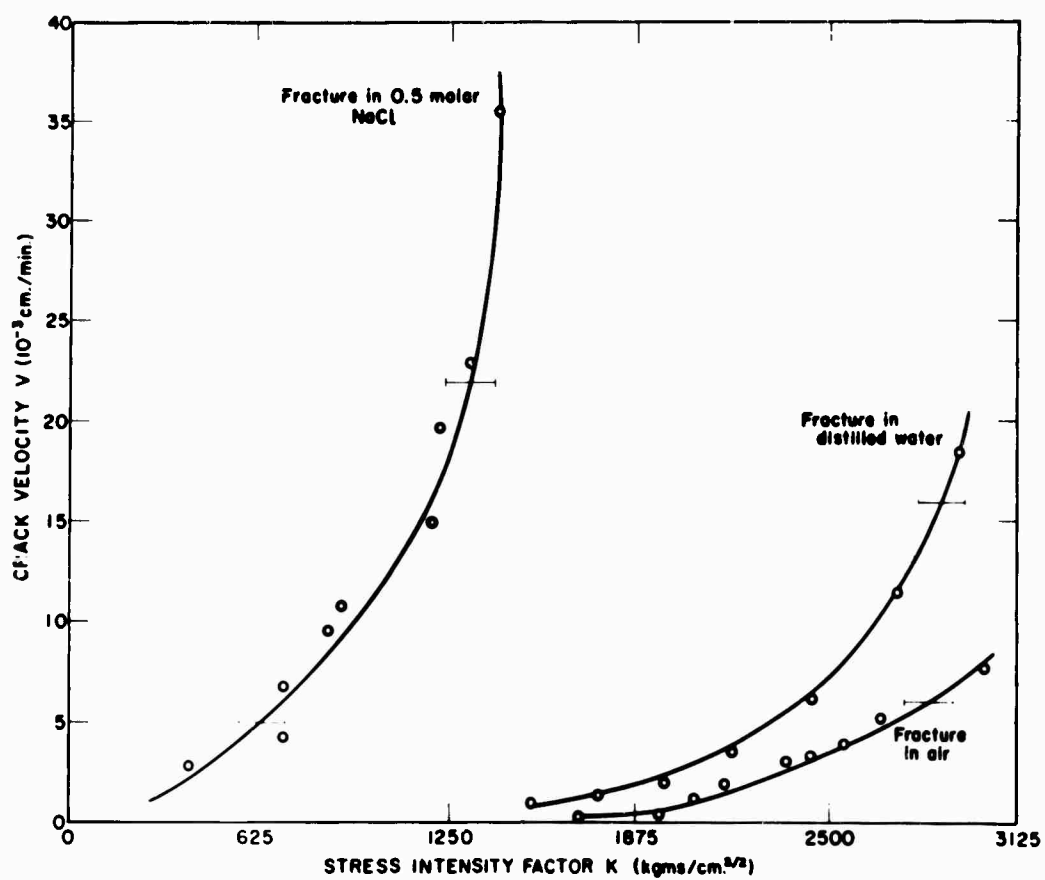


Figure 18. Crack velocity versus stress intensity factor for intergranular fracture in three environments (Air, Distilled H_2O , and .5M NaCl); all points in this figure are for Microstructure No. I, age 50 min. at 155°C prior to a 100 hr. age at room temperature.

fracture test for the same microstructure in a completely inert atmosphere (dry helium or argon). The curve (V versus K) generated in the inert atmosphere would either be coincident with the data for fracture in air or would show a further decrease in the susceptibility to intergranular fracture on Figure (18).

Aside from the obvious trend of a decrease in susceptibility to fracture when testing in air compared to NaCl, Figure (18) shows a certain consistent functional dependence (not linear) between crack velocity V and the stress intensity factor K . A determination of this functional dependence is shown in Figure (19), where V is plotted against K^2 . All three curves in Figure (19) appear to be linear, and this would indicate the following relationship for the three test environments:

$$V = A + B \times K^2 , \quad (V.1)$$

where A and B are constants depending on the test environments. The same dependence of V on K^2 for all three environments would tend to indicate a common intergranular fracture mechanism.

A plausible explanation for the dependence shown in Eq. (V.1) is the so called two stage film rupture mechanism⁽²⁶⁾. In this model, crack advance is discontinuous and occurs by the repetition of two stages; electrochemical and mechanical. The rate controlling process in this mechanism is the formation of a film, i.e., oxide film in metals, at the crack tip. It is then reasoned, if the probability that the film will be ruptured by an avalanche of dislocations is proportional to the plastic zone size, then the rate of crack growth should be

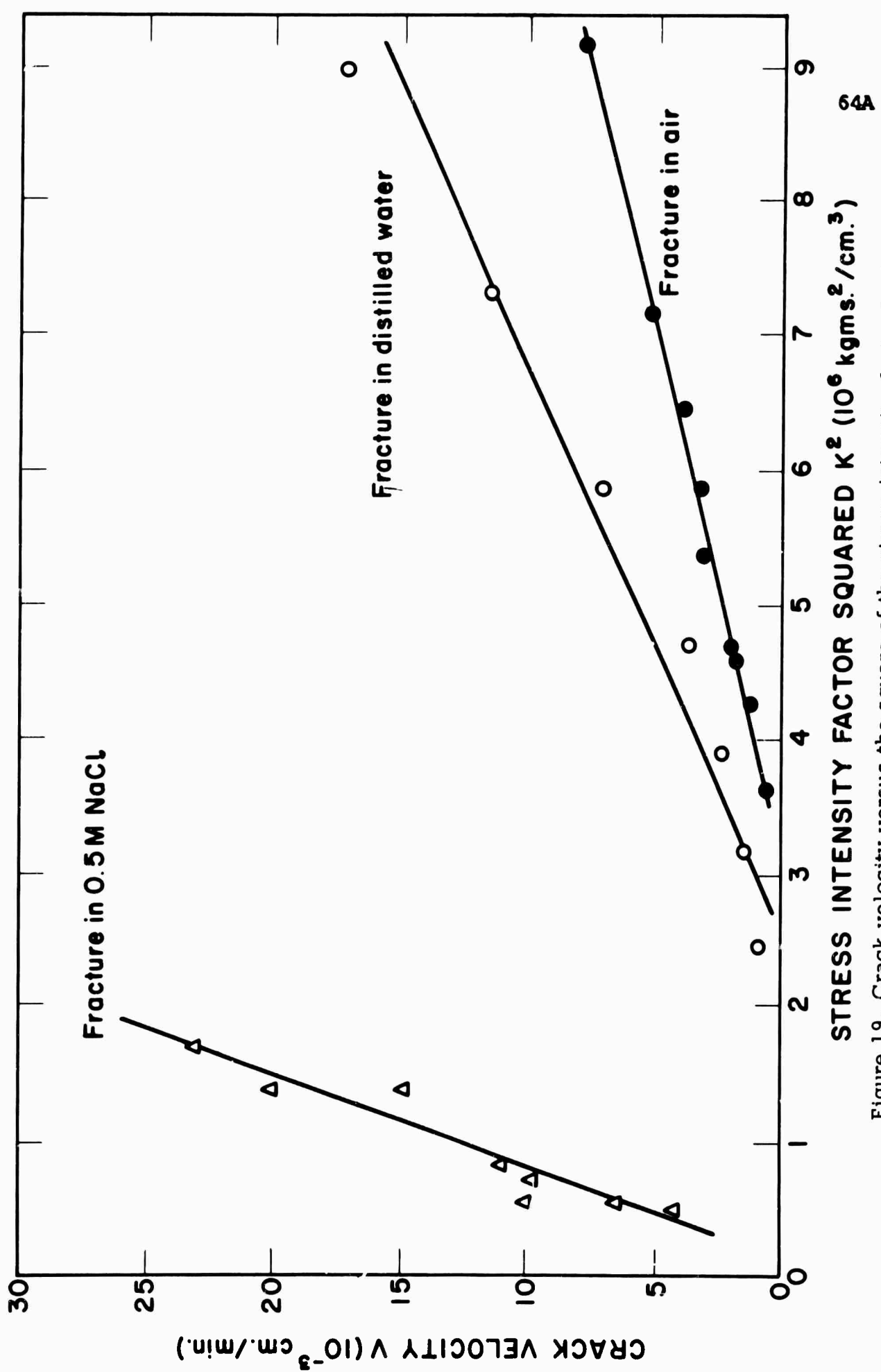


Figure 19. Crack velocity versus the square of the stress intensity factor for intergranular fracture in air, distilled H_2O , and .5M NaCl; test microstructure, No. I, for each environment is held constant.

64A

proportional to the plastic zone size. It can be shown that the plastic zone size is proportional to K^2 (23), and thus this hypothesis predicts a crack velocity dependence on K^2 . However, the theory is inadequate when it comes to explaining the results of intergranular fracture in air, i.e. an inert environment. Thus, a more comprehensive explanation will be developed in section VII to explain the results shown in Figures (18) and (19).

C. The Influence of Microstructure on "Threshold-Toughness" $K_c (V \rightarrow 0)$:

This section will describe the trends observed in air on the intergranular fracture kinetics when varying the heat treatments or microstructures. The microstructures tested in this program aren't too common, and a complete description of the phases present in the matrix and at the grain boundaries will be reserved until the Physical Metallurgy Section, VI.A. At present, all microstructures tested will be noted by the individual heat treatments given to each specimen. A schematic drawing of the thermal treatments leading to the test microstructures is shown in Figure (6). Without going into detail, it is possible to state that as the aging time at 155°C is increased prior to the 100 hr. age at 25°C (room temperature) there is a progressive decrease in the volume fraction of G.P. zones, i.e., coherent Zn rich precipitates in the matrix. This correlation between the volume fraction of G.P. zones and the aging treatment should be kept in mind until a full description of the microstructure is presented.

Four polycrystal specimens (Nos. 1, 3, 8, and 9) with different heat treatments were tested in air at room temperature. Figure (20) is a plot of V

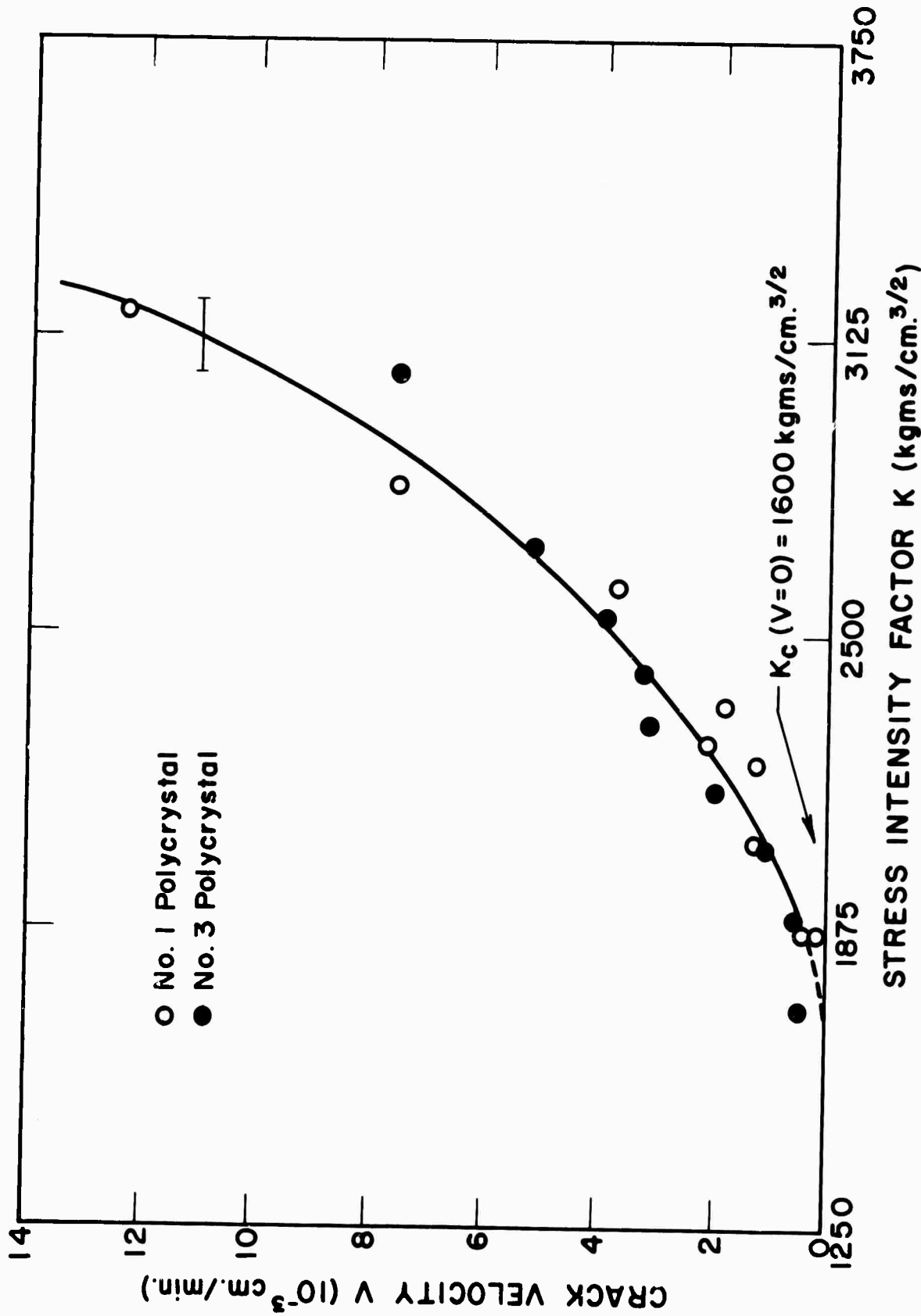


Figure 20. Crack velocity versus stress intensity factor for intergranular fracture in air; Microstructures: No. I polycrystal, aged 50 min. at 155°C prior to 100 hr. age at room temperature and No. III polycrystal aged 15 min. at 155°C prior to 100 hr. age at room temperature.

versus K for two of these specimens. Both specimens were solution annealed at 540°C and then aged for different times at 155°C ; No. 1 received a 15 min. age and No. 3 a 50 min. age. The specimens were then aged at room temperature for 100 hrs prior to testing. Figure (20) shows that there is no discernable difference between these microstructures in terms of intergranular cracking kinetics. Both microstructures have a threshold toughness value $[K_c(v = 0)]$ of $1600 \text{ kgs/cm}^{3/2}$. However, when the aging time at 155°C is increased to 500 min. (No. 9 polycrystal), and the room temperature age is held constant at 100 hrs; a shift in the cracking kinetics is noted. Figure (21) shows this shift where crack velocity V is plotted in units of (10^{-4} cm/min) versus the stress intensity factor K . This figure indicates that there is a decrease in the cracking rate (approximately an order in magnitude when compared at the same K value) for polycrystal No. 9 over Nos. 1 and 3. The extrapolated value of Figure (21) to $K_c(v = 0)$ gives a threshold toughness value of $1880 \text{ kgs/cm}^{3/2}$. Progressive aging to 5000 min. at 155°C (No. 8 polycrystal, Table 13 Appendix I-A) has the effect of completely eliminating intergranular fracture in air at a K value of $2640 \text{ kgs/cm}^{3/2}$, i.e. calculated from Eq. (IV.1) for $K'_{cc} = K_c$.

The results of these tests indicate that progressive aging above 50 min. at 155°C produces a microstructure which increases its resistance to intergranular crack propagation. The corresponding progression in threshold toughness is from $1600 \rightarrow 1880 \rightarrow$ above $2640 \text{ kgs/cm}^{3/2}$. It should also be pointed out that the increasing threshold toughness or crack resistance is accompanied by a

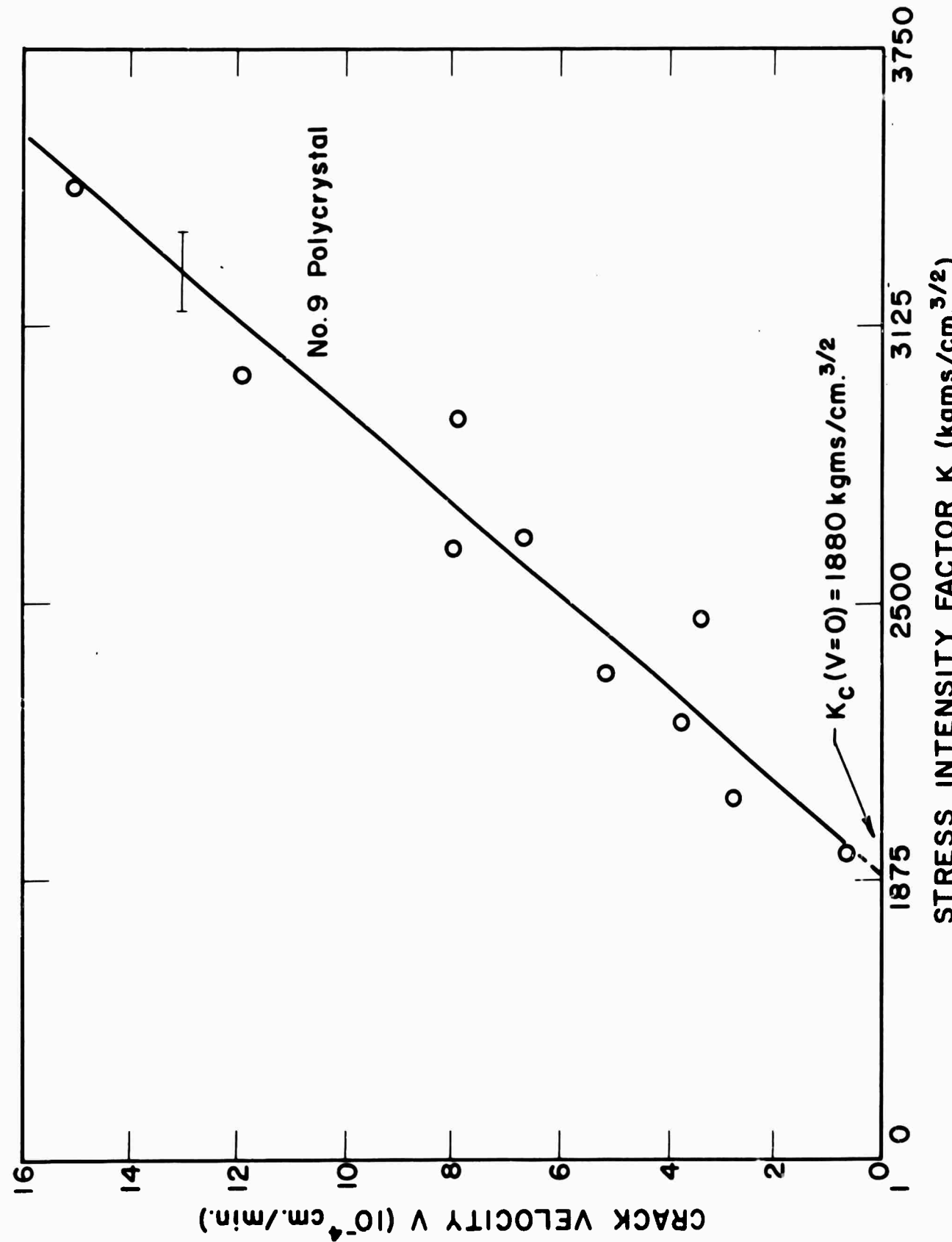


Figure 21. Crack velocity versus stress intensity factor for intergranular fracture in air; Microstructure No. 9 polycrystal, aged 500 min. at 155°C prior to 100 hr. age at room temperature.

decreasing yield strength for the microstructures tested (Figures (11) and (12)).

The table below shows the corresponding values of K_c ($V \rightarrow 0$) and yield strength.

Microstructure aging time at 155°C	Threshold Toughness K_c ($V \rightarrow 0$) ($\text{kgs/cm}^{3/2}$)	Yield Strength 10^3 psi
15, 50	1600	21.5
500	1880	19.0
5000	> 2640	15.8

D. The Influence of Microstructure on Stress Corrosion Cracking Susceptibility:

The heat treatments mentioned in discussing the influence of microstructure on fracture in air are identical to those used for the study of intergranular fracture in 0.5 molar NaCl. The intergranular cracking kinetics studied in the NaCl solution is usually categorized as a stress corrosion cracking phenomenon, and it is considered distinct from intergranular fracture in air. However, it will become apparent that there are strong similarities between the cracking rate dependence on microstructure for fracture in air and in the NaCl solution. Figure (22) is a plot of V versus K for four different microstructures tested in a 0.5 molar NaCl solution. The curve labeled Nos. 4, 5, 6 polycrystals corresponds to a 540°C solution anneal followed by a 50 min age at 155°C and then 100 hrs at room temperature. The next curve labeled No. 12 polycrystal received an identical heat treatment with the exception of a 15 min. age rather than a 50 min. age at 155°C. It appears that these two curves are almost

STRESS CORROSION CRACKING IN 0.5M NaCl

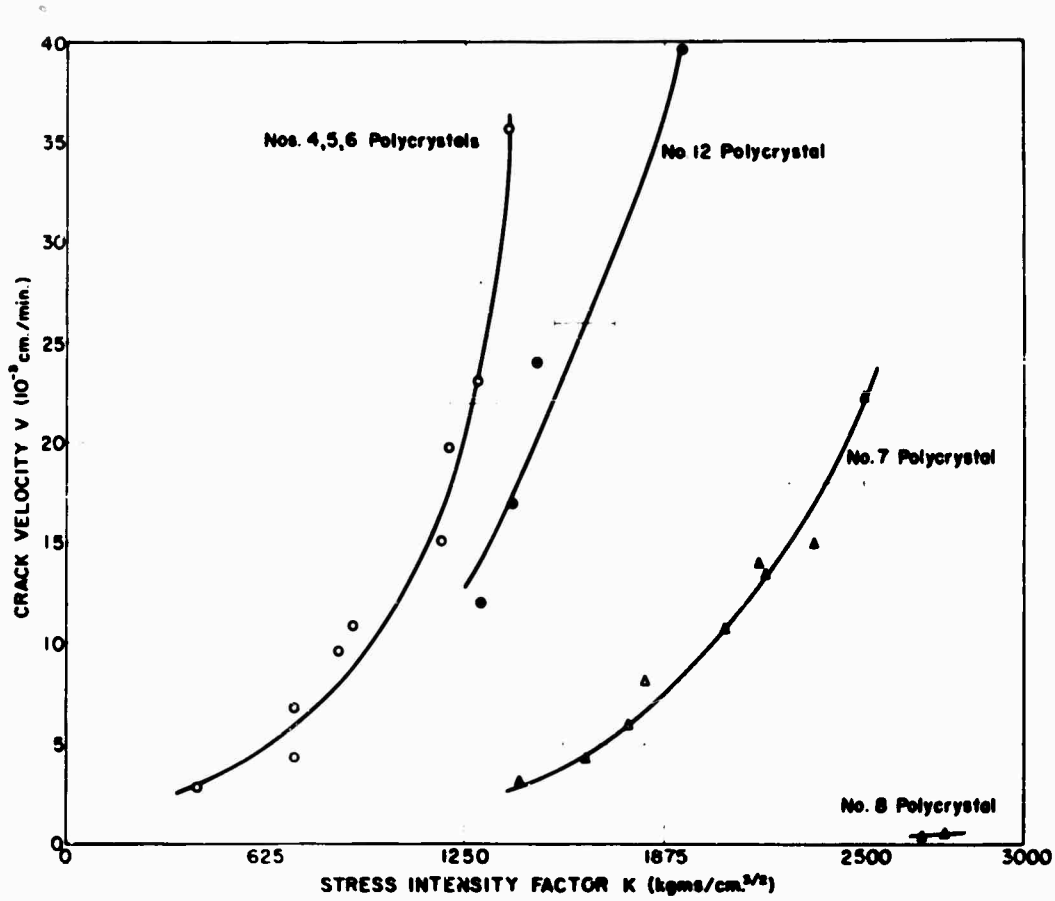


Figure 22: Crack velocity versus stress intensity factor for intergranular fracture in 0.5M NaCl; Four test microstructures: (see section VI.A for full description of Microstructure Nos. I, II, III, and IV corresponding to polycrystal tests in this figure).

coincident but not quite. With some reservation, it can be stated that the shorter aging time, i.e. less than 50 min. at 155°C, produces a microstructure which is slightly more resistant to the stress corrosion cracking properties of the 50 min. microstructure. The other two curves in Figure (22) represent microstructures which received progressively longer aging times at 155°C with no other change in the overall heat treatment. The curve labeled No. 7 polycrystal represents a 500 min. age and No. 8 polycrystal a 5000 min. age. The observable trend from Figure (22) is that progressive aging at 155°C produces microstructures which are successively more resistant to stress corrosion cracking. Quantitatively, this is seen by drawing an iso-velocity (horizontal) line in Figure (22) at a crack velocity at 10^{-2} cm/min. The progressive shift in the stress intensity factor to maintain this level of cracking in the different microstructures is: $1000 \text{ kgs/cm}^{3/2}$ for the 50 min. age to $2000 \text{ kgs/cm}^{3/2}$ for the 500 min. age. The 5000 min. age renders the microstructure so resistant that a cracking rate of less than 10^{-3} cm/min exists at a K value of $2640 \text{ kgs/cm}^{3/2}$ i.e., calculated from Eq. (IV.1) for $K'_{cc} = K_c$.

One other microstructure not plotted on Figure (22) was tested in the NaCl environment. This specimen was No. 10 polycrystal (Table 13 in Appendix I-A). The heat treatment of No. 10 polycrystal was the same as Nos. 4, 5, 6 polycrystals, a 50 min. age at 155°C. However, instead of a 100 hr. age at room temperature prior to testing, No. 10 polycrystal was only allowed to age for 30 min. at room temperature before the test. The resulting microstructure was

extremely resistant to fracture in the NaCl solution, and no cracking was observed at a K value of $1230 \text{ kgs/cm}^{3/2}$, i.e. calculated from Eq. (IV.1). This same microstructure, No. 10 polycrystal, if allowed to age for 100 hrs at room temperature, would then exhibit a cracking rate of $2 \times 10^{-2} \text{ cm/min}$ at the same K value, $1230 \text{ kgs-cm}^{3/2}$. Thus, the aging at room temperature, irrespective of the aging time at 155°C , has a marked effect on the microstructure's resistance to crack propagation.

E. A Comparison of the Cracking Kinetics Between Intergranular Fracture in Air and in 0.5M NaCl:

The microstructural variations produced by progressive aging at 155°C give successive increases in the resistance to intergranular fracture in air and in NaCl. Thus, the addition of a corrosive environment (0.5M NaCl) does not change the effect of microstructure on cracking susceptibility. However, when cracking occurs in the NaCl environment the microstructural trends are the same, but there is a scale shift toward higher cracking velocities at lower stress intensity factors when compared with cracking rates in air. As the fracture environment is changed from air to 0.5M NaCl, the scale shift results in an increase in the crack velocity at a constant stress intensity factor or as a decrease in the stress intensity factor at a constant crack velocity. This is apparent when comparing Figures (20) and (21) for fracture in air with Figure (22) for fracture in NaCl. A quantitative description of this acceleration effect on cracking velocities for the same microstructures tested in air and in NaCl is

shown below:

Microstructure Aging Time at 155°C	Fracture Environment	Velocity cm/min	Stress Intensity Factor $\text{kgs}/\text{cm}^{3/2}$
50 min.	NaCl	1.0×10^{-2}	940
	Air	1.0×10^{-2}	3070
500 min.	NaCl	2.2×10^{-2}	2500
	Air	6.0×10^{-4}	2500
5000 min.	NaCl	6.0×10^{-4}	2750
	Air	0.0	Greater than 2750

The trends for this table show that a three fold increase in the stress intensity factor is necessary to maintain a cracking rate of 10^{-2} cm/min. in the 50 min. microstructure. Conversely, keeping the stress intensity factor constant at $2500 \text{ kgs}/\text{cm}^{3/2}$ in the 500 min. microstructure results in a decrease (approximately two orders in magnitude) in the cracking rates between NaCl and air.

F. Corrosion in the Absence of Stress:

An experiment was performed to determine any degradation in bulk mechanical properties after specimens were subjected to a corrosive environment (0.5M NaCl) in the absence of stress. This was done to separate the effects of corrosion on the phenomenon of stress corrosion cracking. The microstructures tested were those previously described; 50, 500, and 5000 min. age at 155°C followed by a 100 hr. age at room temperature. Tensile specimens of these microstructures were tested for yield strengths after having been

immersed in 0.5M NaCl for 5 days. The yield strengths determined were the same as the yield strengths of microstructures not subjected to a corrosive environment. Thus, there is no degradation in yield strength for the microstructures tested after a 5 day exposure to the NaCl solution.

In addition to testing for bulk mechanical properties, the tensile surfaces were replicated after being exposed to the corrosive environment. The noticeable features of these surfaces are the corrosion pits occurring at the precipitated In_{2}O_3 rich phase in the microstructure. This is readily seen in Figure (23), a replica of the microstructure aged for 50 min. at 155°C . The long shadows are a result of the extent or depth of corrosion pits during the shadowing operation at 45° . Knowing this angle and the shadow length, it is possible to calculate a corrosion pit depth of approximately 1μ . Thus, the extent of pitting is quite shallow, and it would not be expected to influence bulk mechanical properties.

G. The Dependence of Stress Corrosion Cracking Susceptibility on Bi-crystal Orientation:

The previous mentioned results described polycrystal tests and the influences of microstructure on environment sensitive intergranular fracture. Aside from microstructure, the other predominant material variable influencing intergranular fracture is an orientation affect of grains adjacent to the grain boundary or fracture path. This affect was studied by testing different bi-crystal orientations all with the same microstructure. The constant microstructure chosen for the bi-crystal tests was the structure determined to be most susceptible in the polycrystal tests in NaCl. The microstructure corresponds to



Figure 23. 10,000X, two stage carbon-platinum replica of a corrosion surface; shadowing angle of approximately 45° shows the extent of localized pitting at zinc precipitates.

polycrystal Nos. 4, 5, and 6 in Figure (22), i.e. a 50 min. age at 155°C followed by a 100 hr. age at room temperature. The results of the double cantilever beam tests for the bi-crystals are listed in Appendix I-C. In addition to average G and V values listed, bi-crystal orientations are described by five critical angles. These results are plotted in Figure (24) where the average crack velocity V is plotted against the average elastic energy released G. Each number in this figure represents a distinct bi-crystal test and orientation. Also dashed lines are drawn in Figure (24) to indicate transition areas between three regions A, B, and C. Irrespective of bi-crystal orientations, a calculation of the average values of V and G for each region yields the following table.

Region	Average Values	
	V(cm/min)	G(kgs/cm)
A	$2.0 \cdot 10^{-2}$	0.4
B	$1.2 \cdot 10^{-2}$	0.9
C	$0.9 \cdot 10^{-2}$	1.4

Table of Bi-crystal Tests in 0.5M NaCl (from Figure 24)

It is immediately apparent that bi-crystals in Region A are more susceptible to intergranular fracture, i.e., higher cracking velocity at lower G, than bi-crystals in Region B. Likewise, the same trend is observed between Regions B and C. Thus, there is a progressive increase in the resistance to fracture from Region A → B → C. This result has not taken into account the distinct orientations involved in the bi-crystals tested. It will be shown that these three

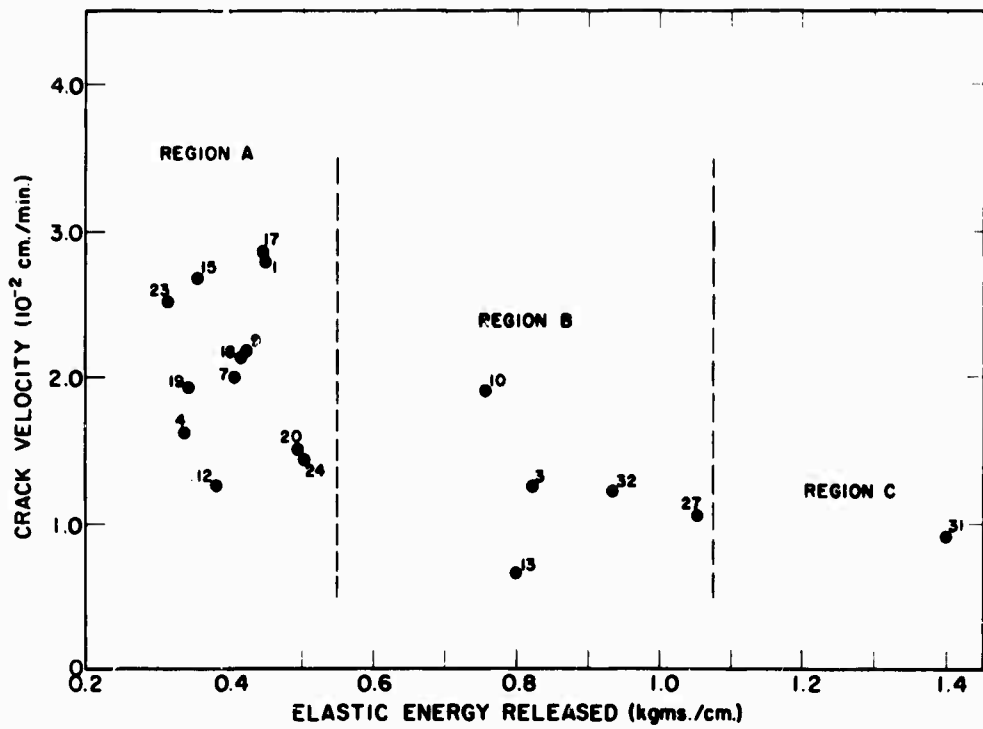


Figure 24. Average crack velocity versus average elastic strain energy released for intergranular fracture of bi-crystals in 0.5M NaCl; all bi-crystals tested have the same microstructure (50 min. age at 155°C prior to a 100 hr. age at room temperature.

regions not only define a transition in cracking susceptibility but also a general difference in the bi-crystal orientations.

The stereographic projections of bi-crystals No. 31 (in Region C) and No. 32 (in Region B) and No. 4 (in Region A) are shown in Figure (25), (26), and (27). The common trend between the two projections representing Regions B and C is the coincidence of {111} slip planes and <110> slip directions between adjacent grains. Bi-crystal No. 31 is a low angle (simple tilt or twist) grain boundary with all four slip planes in each grain coincident; two poles that are within 12° of each other are considered coincident. Also two slip directions are parallel for each pair of coincident {111} poles. Bi-crystal No. 32 in Region B has only two slip planes and directions in each grain which are coincident (see Figure (26)). Similarly, bi-crystal No. 27 in Region B has two pairs of coincident slip systems. If the other three bi-crystals (Nos. 3, 10, 13) in Region B are plotted, only one slip plane and direction in each grain would be found to be parallel. All bi-crystals in Region A are typical of the stereographic projection of No. 4 bi-crystal shown in Figure (27), and no coincidence or parallel slip systems are observed between the two grains. Thus, the increasing resistance to intergranular fracture when proceeding from Region A → B → C is accompanied by an increasing coincidence of slip systems between the two adjacent grains in the bi-crystal.

Bi-Crystal No. 31

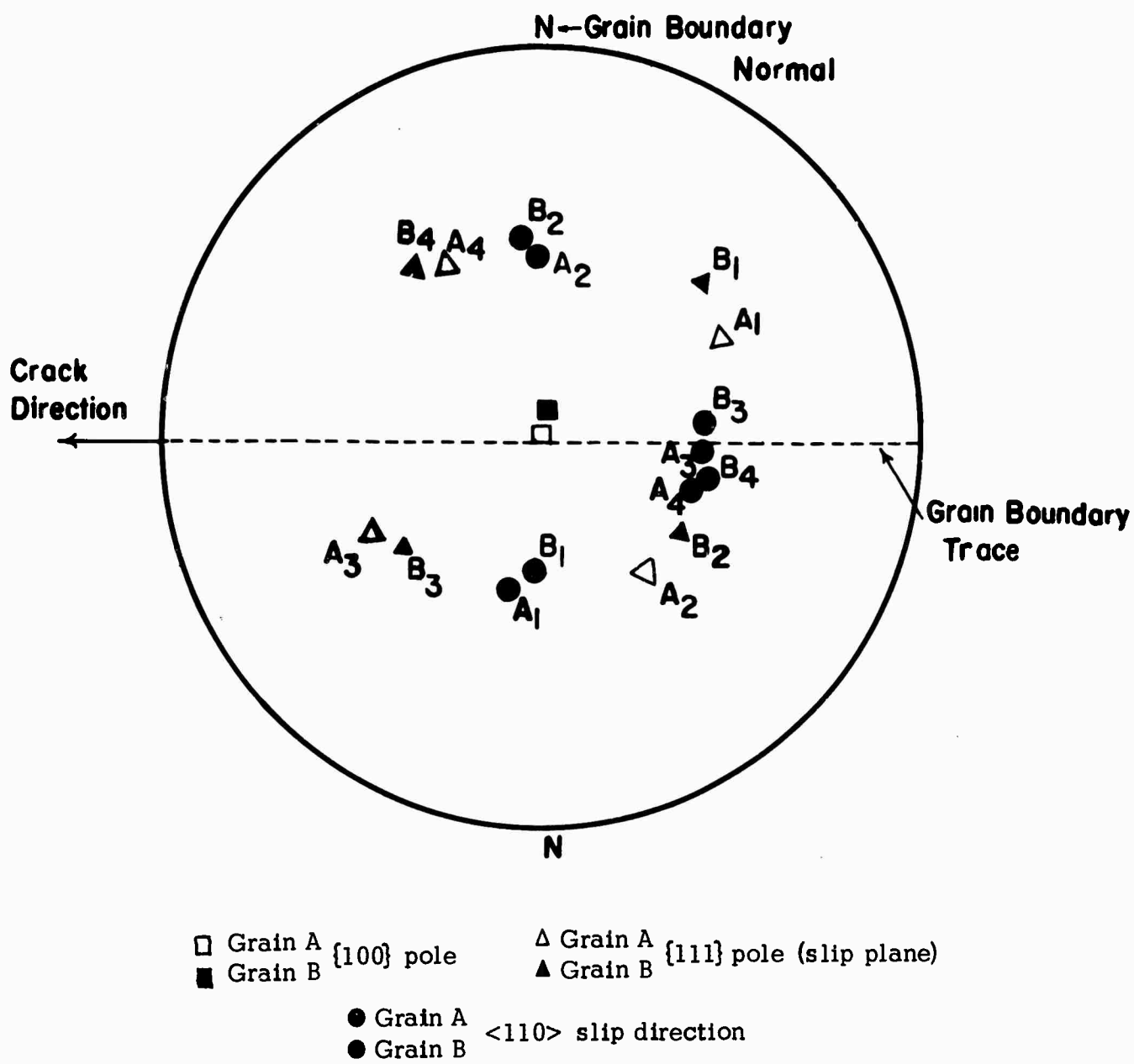


Figure 25. Stereographic projection of bi-crystal No. 31 in Region C of Fig. (24), with four coincident sets of slip systems; highly resistant to intergranular fracture in 0.5M NaCl

Bi-Crystal No. 32

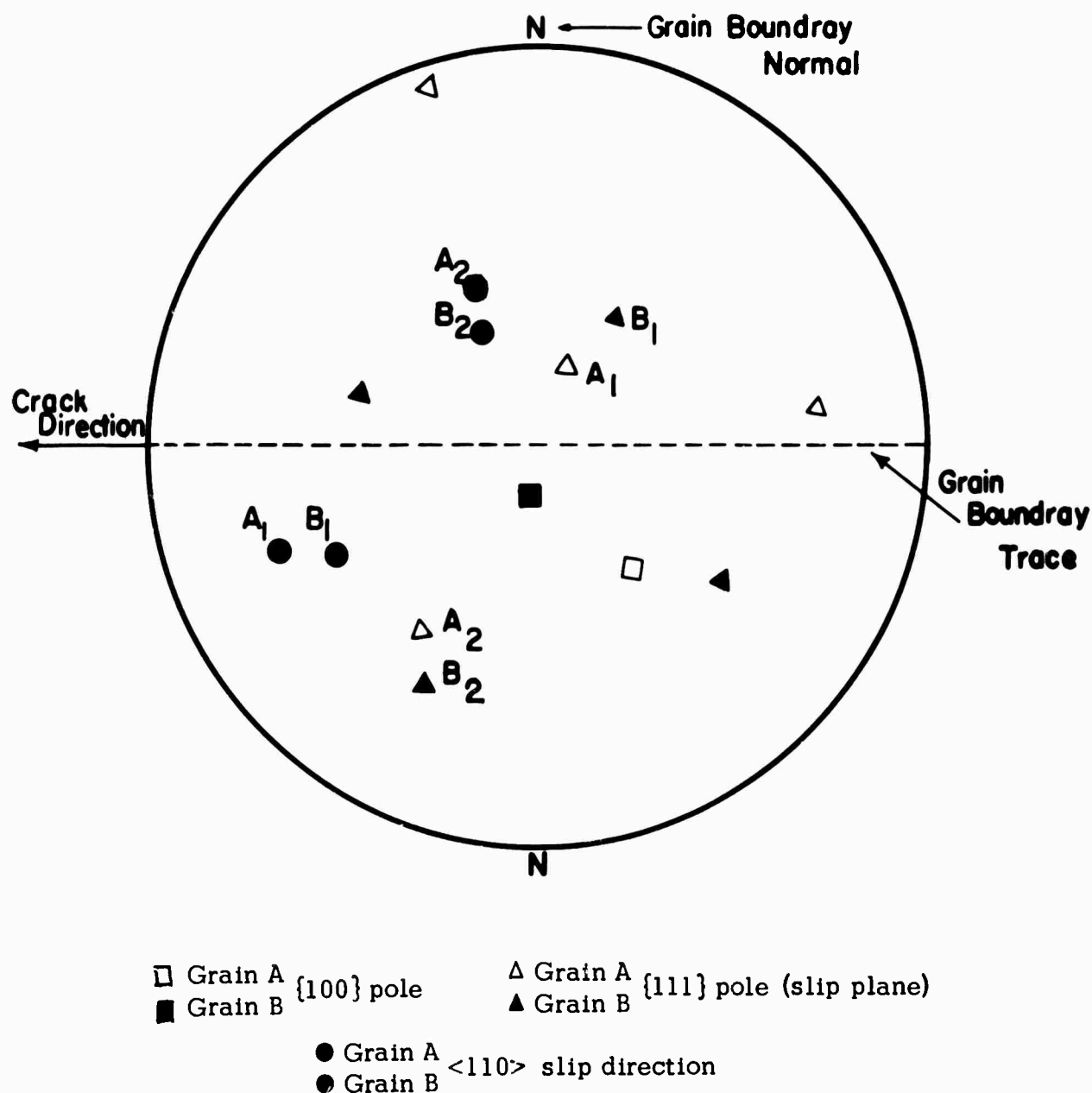


Figure 26. Stereographic projection of bi-crystal No. 32 in Region B of Fig. (24), with two coincident sets of slip systems; slightly less resistant to intergranular fracture than No. 31 bi-crystal.

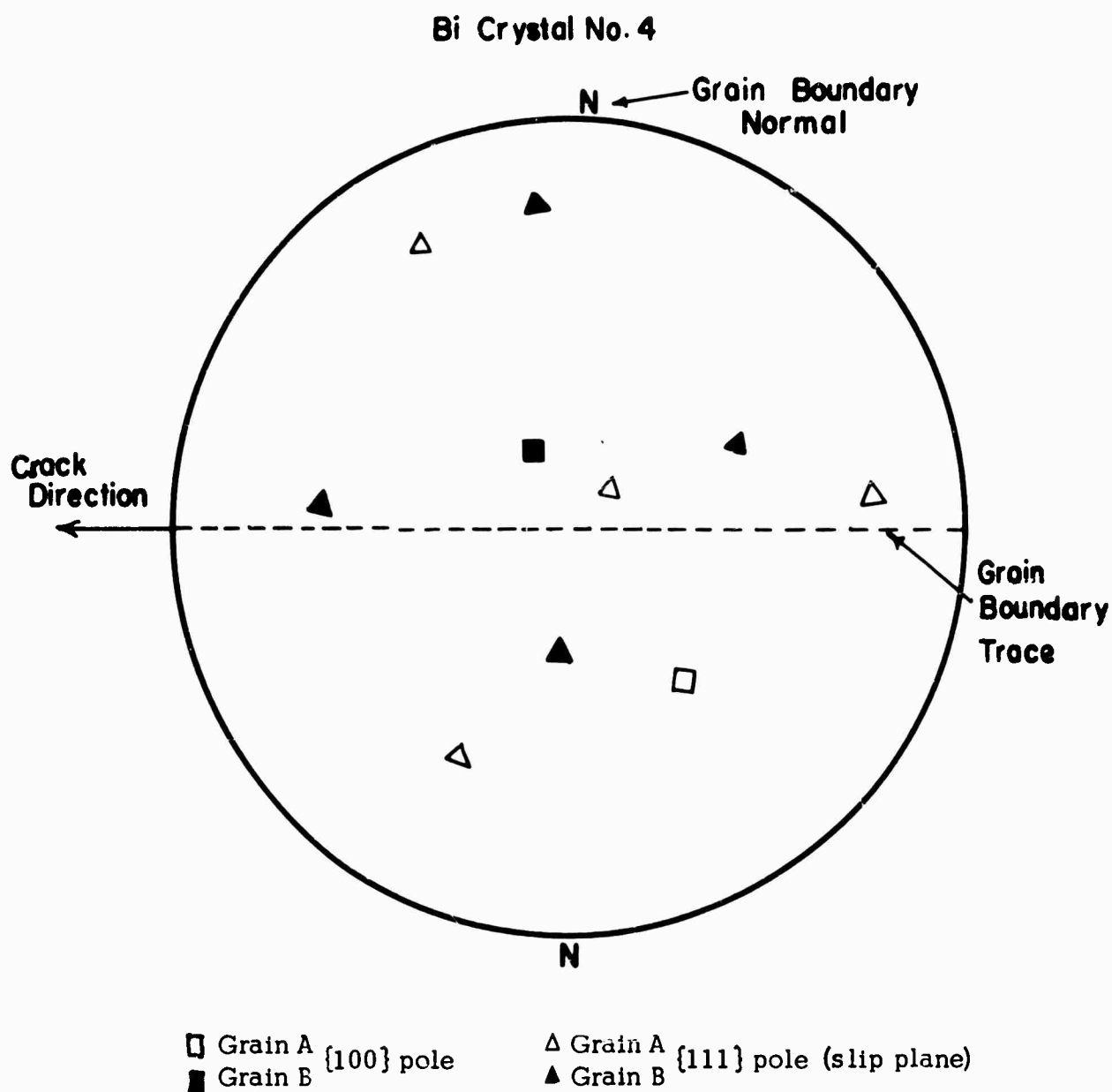
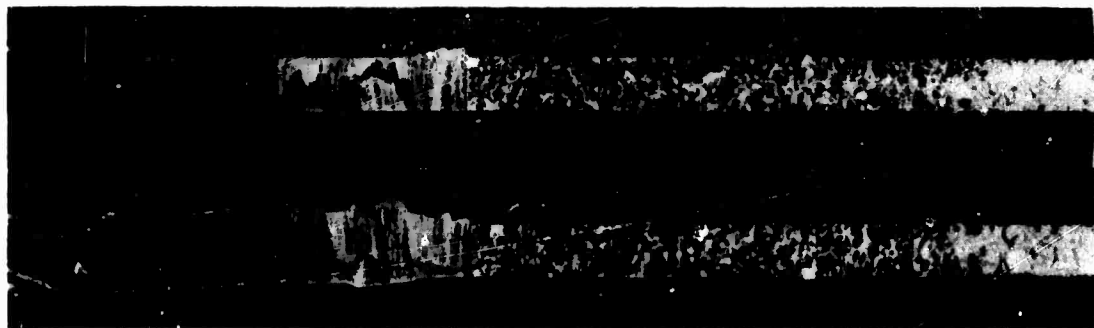


Figure 27. Stereographic projection of bi-crystal No. 4 in Region A of Fig. (24), with no coincident sets of slip systems; highly susceptible to intergranular fracture in 0.5M NaCl.

H. A Comparison of Bi-crystal to Polycrystal Susceptibility in 0.5M NaCl:

Aside from the orientation affect, it might be expected that grain size would influence intergranular fracture. To test this, a comparison can be made between the bi-crystal and polycrystal specimens of the same microstructure. However, the difficulty is in what constitutes a mean value for V and G when selecting from the bi-crystal tests, i.e. Figure (24). This is analogous to the particular grain boundary orientation in Figure (24) that is truly representative of an average grain boundary in a polycrystal aggregate. This would necessitate knowing the probability of occurrence for particular orientations. To avoid this difficulty, the mean values of V and G for the three regions (A, B, C) in Figure (24) will be compared to the corresponding V and G values of polycrystal Nos. 4, 5, 6 in Figure (22). Before this comparison is made, the crack velocities plotted in Figure (22) for the polycrystal specimens must be corrected so that they are equivalent to the measured bi-crystal velocities. The correction involved in the measured polycrystal crack velocities is seen in Figure (28). This figure shows both the top and profile views of a fractured polycrystal aggregate. In the profile view, it is apparent that the wavy crack length is greater than the measured horizontal value. A correction factor of 1.35 times the measured crack length is necessary to convert to the true crack length profile. Using this correction, crack velocities in Figure (22) can be converted to values which can be compared to the bi-crystal tests in Figure (24). The following tables are a listing of the different G values necessary to maintain a



1.7X: Top view of DCB No. 7 polycrystal fracture surface; equi-axed intergranular fracture surface.



25X: Profile view of intergranular fracture in DCB specimen; total crack length is approximately 1.35 times measured crack length.

Figure 28.

constant cracking rate between polycrystal and bi-crystal tests.

*Polycrystal Tests

Actual V (cm/min)	$1.35 \times V$ cm/min	G (kgs/cm)
$1.5 \cdot 10^{-2}$	$2.0 \cdot 10^{-2}$	1.6
$0.9 \cdot 10^{-2}$	$1.2 \cdot 10^{-2}$	1.1
$0.7 \cdot 10^{-2}$	$0.9 \cdot 10^{-2}$	0.7

*(Nos. 4,5,6 Figure 22)

*Bi-crystal Tests

Region	Average Values	
	V(cm/min)	G(kgs/cm.)
A	$2.0 \cdot 10^{-2}$	0.4
B	$1.2 \cdot 10^{-2}$	0.9
C	$0.9 \cdot 10^{-2}$	1.4

*(Figure 24)

A comparison of these tables show that bi-crystals in Region A, when cracking at the same rate as a polycrystal, require only 1/4 the G value, (.4 compared to 1.6 kgs/cm). However, the bi-crystals in Region B require essentially the same energy release rate as a polycrystal to crack at $1.2 \cdot 10^{-2}$ cm/min. The one bi-crystal representing Region C is much more resistant to fracture than the polycrystal aggregate, and requires twice the energy release rate as the polycrystal. If the average polycrystal grain boundary possesses an orientation in Region B then there would not appear to be a grain size affect on intergranular fracture. However, if the average orientation is in Region A then bi-crystals would be more susceptible than the polycrystal aggregate.

VI. Discussion of Results

The previous sections describing cracking results all dealt with the effects of various heat treatments on intergranular fracture. No specific mention was made of the phases present in these different heat treatments. However, without a detailed description of the microstructures resulting from these treatments, little correlation could be made with their effects on intergranular fracture. Consequently, this section will describe the microstructures resulting from the selected heat treatments. Initially a brief description will be presented on the phases (their size and crystallography in the matrix) and the precipitation sequence of these phases. This will be followed by a detailed description of the phases present in the microstructure after the heat treatments used in this study.

A. Physical Metallurgy of the Al-Zn System:

The sequence and mechanism of structure transformations in supersaturated solid solutions of Al-Zn alloys were established by X-ray diffraction and electron microscopic investigations^(17, 28). These gave evidence of the following precipitation sequence in Al-Zn alloys: Spherical G.P. zones \rightarrow Ellipsoidal G.P. zones \rightarrow rhombohedral transition phase $\alpha'_R \rightarrow \alpha_{\text{cubic}}$ cubic transition phase \rightarrow zinc rich stable precipitates. It is shown that after quenching spherical G.P. zones are formed. These G.P. zones are homogeneous and coherent in the matrix, having the same crystal structure as the matrix. At a critical zone radius of about $35\text{\AA}^{(29)}$, the anisotropy of coherency strains around the spherical G.P.

zones lead to the contraction of the lattice spacing along one of the $\langle 111 \rangle$ directions inside the zones. These internal rhombohedral lattice deformations give rise to a change of the spherical shape of the zones into an ellipsoidal one. These ellipsoidal G.P. zones are always coherent with the matrix. The coherency strain fields have a rhombohedral symmetry. The typical dimensions of the ellipsoidal G.P. zones are thought to be between 100 and 150 \AA in the $\{111\}$ planes and between 30 and 50 \AA in the normal direction. The loss of coherency of the ellipsoidal G.P. zones with the matrix, except in the $\{111\}$ -habit plane, leads to the development of the transition rhombohedral phase α'_R . Its diameter is more than 1000 \AA and the thickness is between 100 and 200 \AA . The well known incoherent cubic α' transition phase is developed by breaking down the partial coherency of the rhombohedral phase α'_R . The stable Zn precipitates are finally formed by continuous precipitation on the α' -phase, with the basal planes parallel to the $\{111\}$ planes of the matrix. These recent studies involving the precipitation sequence in the Al-Zn system provide a basis for correlating microstructure to a particular thermal history.

A schematic diagram of the thermal history of the Al-15 wt % Zn alloy is shown in Figure (6). Initially, specimens are homogenized at 430°C to prevent grain boundary liquation when solution annealing at 540°C. The specimens are then directly quenched into a silicone oil bath at 155°C and aged for various times prior to a kerosene quench to room temperature. The significance of aging at 155°C in this alloy system is that this temperature is above the G.P.

zone solvus temperature, i.e. 150°C ^(30,31). Thus, aging at this temperature would suppress any G.P. zone formation and favor heterogenous nucleation. After aging at 155°C , the specimens are quenched and aged at room temperature for various times.

Following this heat treating sequence, the bulk mechanical properties of the Al-15 wt % Zn system are shown in Figure (11). The labeled numbers on this figure represent the different microstructures tested:

Microstructural States: Nos. I, II, III, IV and V.

No. I: Age 50 min. at 155°C and 100 hrs. at room temperature.

No. II: Age 500 min. at 155°C and 100 hrs. at room temperature.

No. III: Age 5000 min. at 155°C and 100 hrs. at room temperature.

No. IV: Age 15 min. at 155°C and 100 hrs. at room temperature.

No. V: Age 50 min. at 155°C and 2 hrs. at room temperature.

B. Metallographic Observations:

The probable microstructural variations in the matrix when proceeding from State I \rightarrow II \rightarrow III are as follows. State No. I contains the intermediate α' platelet phase and occasionally the stable Zn precipitate nucleated at grain boundaries. No α' platelet phase was noticed at heterogenous points (dislocations) in the matrix. These features are seen in Figure (29) part A with the α' phase at the grain boundary and the dislocations in the matrix devoid of any noticeable precipitate. The matrix of microstructure No. I consists of a large volume fraction of G.P. zones, and this is shown in Figure (29) part B. The



Part A: 22,000X, Microstructure No. I showing α' Zn precipitate at grain boundary and not at dislocations.



Part B: 60,000X, Microstructure No. I showing G.P. zones in the matrix.

Figure 29.

mottled type appearance of the picture in part B is representative of a small coherent phase in a matrix. Since the material has a well annealed structure and does not receive a severe quench, it would have approximately 10^7 - 10^8 dislocations/cm². This low dislocation density would offer relatively few nucleation sites in the matrix for the intermediate α' platelet phase. Also from Figure (29) part A, it appears 50 min. at 155°C is insufficient to form the α' phase at dislocations. Progressive aging at 155°C to states II and III will cause a growth of α' at dislocations and the coarsening of α' to stable Zn precipitate at grain boundaries. Figure (30) parts A and B show the α' phase precipitated at dislocations in the matrix for states II and III. The size of the α' in state III is approximately 3 to 4 times the α' in state II. This is consistent with the longer aging time of 5000 min. for state III compared to 500 min. for state II. Likewise the growth of grain boundary precipitate for state II compared to state I is shown in Figure (31). As a result of this sequence, the change in microstructure between states I, II, and III involves a progressive decrease in the volume fraction of G.P. zones. This occurs because of a depletion of Zn in the solid solution with a growth of α' at grain boundaries and dislocations.

Because of the small volume fraction of α' and stable Zn precipitated widely dispersed through-out the matrix of states I, II, and III, it is unlikely that these precipitates play a predominant role in hardening the matrix. Recently Price and Kelly⁽²⁸⁾ and Dash and Fine⁽³²⁾ reported a study of the

79A



Part A: 60,000X, Microstructure No. II showing α' Zn precipitate at dislocations.



Part B: 48,000X, Microstructure No. III showing α' Zn precipitate at dislocations.

Figure 30

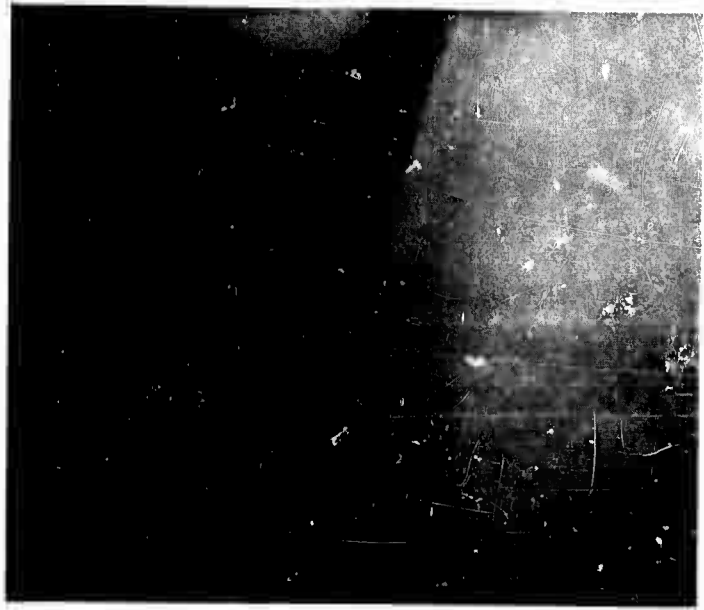


Figure 31. 40,000X, Microstructure No. II showing extent of Zn precipitate at grain boundary.

relative hardening effects of G.P. zones and α' in the Al-Zn system. Their results showed that the hardening effect was proportional to the square root of the volume fraction of G.P. zones. Also, they showed the effect of α' on hardening was negligible because dislocations passed readily through these platelets. Thus, the progressive decrease in yield strength for microstructures I \rightarrow II \rightarrow III is predominately a result of the decrease in the volume fraction of G.P. zones. The increase in yield strength for each microstructure resulting from G.P. zone formation at room temperature is shown in Figure (12).

Figure (12) shows that a solution heat treated specimen directly quenched to room temperature and tested immediately has a yield strength of 6,500 psi. This yield strength is due to solid solution hardening alone without the imposed effects of G.P. zone hardening. It is possible that a small amount of α' and stable Zn precipitate have nucleated at grain boundaries in addition to some G.P. zone nucleation in the matrix; but the predominant microstructure is a solid solution of Zn in Al. Thus, the yield strength of this solid solution represents a base level in mechanical properties, and the subsequent nucleation and growth of G.P. zones tends to harden the matrix. The progressive increase in yield strength with aging time at room temperature is then attributed to G.P. zone nucleation followed by growth up to approximately $35\text{\AA}^{(29)}$. After the growth of G.P. zones to a stable size, 35\AA , a plateau is reached in yield strength and no additional increase in yield strength is obtained upon aging to 200 hrs at room temperature. The differences in the aging characteristics

between the three curves in Figure (12) can be accounted for by the different aging times at 155°C prior to aging at room temperature.

The other two microstructures of interest, IV and V labeled in Figure (11) are a consequence of distinguishing between the predominant role of matrix precipitates over grain boundary precipitates in the intergranular fracture process of this alloy system. The yield strengths of microstructures I and IV are essentially the same, but the volume fraction of precipitates at grain boundaries and dislocations in microstructure IV is smaller than in I, i.e., a consequence of the shorter aging time. However, microstructure V possesses the same volume fraction of precipitates at grain boundaries as microstructure I but a much smaller volume fraction of G.P. zones in the matrix, accounting for the low yield strength. Thus, microstructures I, IV, and V permit a comparison in determining the predominant role played by either matrix or grain boundary precipitates in the intergranular fracture process of this alloy.

C. Surface Topograph of Intergranular Fracture In Air and In 0.5M NaCl:

The topographic features associated with intergranular fracture are generally useful in deducing the type of fracture (auctile or brittle) and also can be of assistance in determining the cause of fracture. These considerations then make it essential to understand the relationship between microstructure and the resulting intergranular fracture features before an attempt at relating microstructure to cracking kinetics can be made. The resulting fractures of both the bi-crystal and polycrystal specimens tested in air and in 0.5M NaCl all have

three distinct topographic features:

A - Faceting or a serrated grain boundary structure composed of apparent crystallographic steps.

B - Fine and coarse slip line striations on all fracture surfaces as well as on the side surfaces of bi-crystal specimens.

C - Corrosion pitting of the Zn precipitate at the grain boundary.

Figure (32) clearly exemplifies all three of these surface features with fine slip markings apparent on the facet steps and a general background of localized pitting at Zn precipitates. Each of these features will be discussed separately with the resulting cumulative affect on the fracture process.

1. Faceting: The first noticeable feature in Figure (32) is the periodic, apparent crystallographic steps or facets on the bi-crystal fracture surface. Originally, it was thought that these steps were a result of the fracture process, i.e., similar to the toughening effect observed when testing MgO in water⁽³³⁾. However, closer scrutiny of the grain boundaries in the bi-crystal specimens prior to fracture, in the NaCl solution, revealed a serrated grain boundary structure. This is shown in Figure (33), a profile view of a bi-crystal grain boundary taken after all thermal heat treatments but prior to the DCB test. The profile view depicts the serrations or saw tooth effect of the facets which correspond to the top view of the grain boundary fracture surface shown in Figure (32). These serrations appeared to be much larger in magnitude and extent on bi-crystal grain boundaries when compared to the polycrystal boundaries.

82A

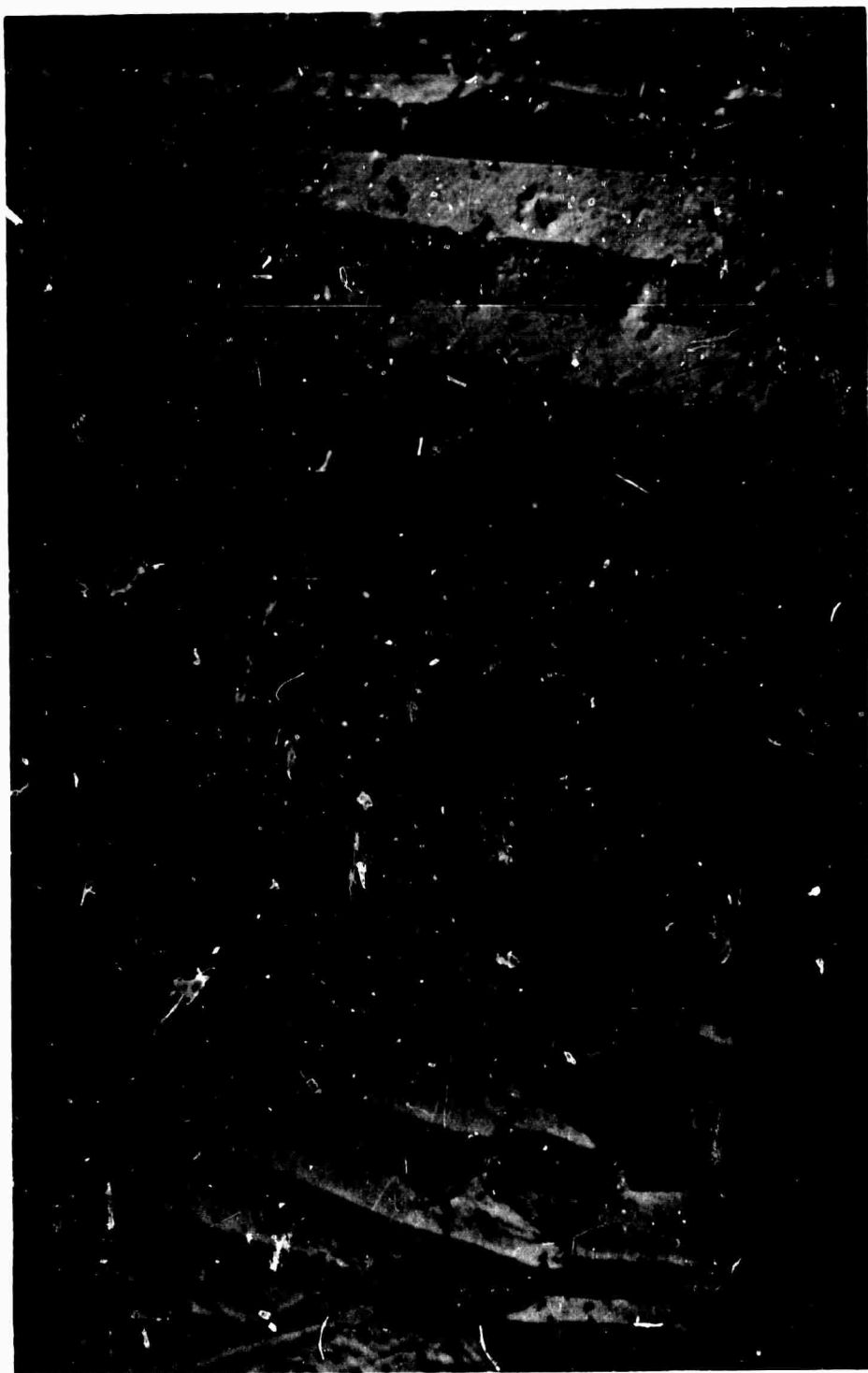


Figure 32. 400X, No. 2 Bi-crystal fracture surface showing facets (step-like appearance), slip traces on facets (fine striations), and localized pitting at Zn precipitate; Fracture in 0.5M NaCl for Micro-structure No. I.

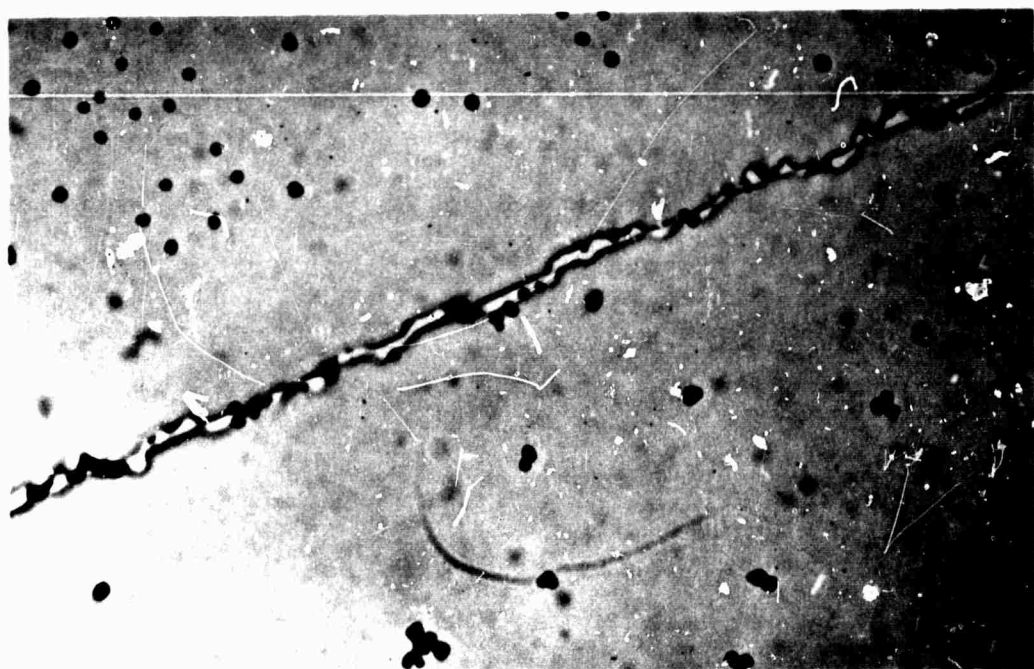


Figure 33. 1000X, profile view of grain boundary on bi-crystal surface prior to fracture; remnants of serrated grain boundary profile are present after electropolishing preferentially attacked the boundary.

Also, the number of facets per unit grain boundary area varied considerably for the different specimens tested. These general observations indicate that the faceting of grain boundaries is a function of thermal history and grain boundary orientation. This would indicate a direction toward stable equilibrium, and at equilibrium the sum of the surface free energies for all surfaces, F_s , is a minimum.

If A_i is the area of the i^{th} surface, and γ_i is its specific free energy, this can be written $F_s = \sum \gamma_i A_i$. If the grain boundary free energy depends on the orientation of the boundary, the differential of F_s takes the form $dF_s = \sum \gamma_i dA_i + \sum A_i dy_i$. Thus, the surface area of the grain boundary can increase with faceting provided the individual facets represent a decrease in free energy over the original planar boundary⁽³⁴⁾. This type of faceting has also been observed by Crussard⁽³⁵⁾ in a brittle iron alloy, and it was found to be strongly dependent on prior thermal treatments. Crussard reached the conclusion that the faceting was a result of the grain boundary assuming a microgeometric configuration consistent with a reduction in energy.

No further characterization of this effect was undertaken since it would have entailed a major study not directly related to the problem of cracking kinetics. It is fairly conclusive that the facets are due to a minimization of free energy and not a consequence of the fracture process. However, the influence of the facets on crack advance in bi-crystal specimens does play a minor role, and it will be discussed in the next section.

2. Slip Line Patterns: Aside from the three distinct topographic features, the general appearance of all fracture surfaces is their apparent brittleness and lack of any dimple or ductile rupture. This leads to the question: what are the characteristics of a solid that endow it with a susceptibility to brittle fracture regardless of its environment? It is well known that a coarse grain size^(36,37) and a high yield stress^(36,37) and an inability to deform on a sufficient number of slip systems⁽³⁸⁾, (to satisfy the von Mises criterion), all promote brittleness. Moreover, it has been demonstrated recently⁽³⁹⁾ that an increased resistance to cross slip also reduces the fracture stress and ductility of those solids capable of cleavage. More importantly, it has been shown that the propensity for cross slip plays a similar role in fcc solids when deformed in an embrittling liquid metal environment⁽⁴⁰⁾. It is the purpose of this section to emphasize further that the consequence of changes in slip line patterns on the fracture surfaces of bi-crystal and polycrystal specimens are of general significance in the fracture process.

The most important feature on a typical intergranular fracture surface is shown as fine discrete parallel lines on the facets of the bi-crystal fracture in Figure (32). The fine striations are more pronounced in Figure (34) parts A and B, and the intersecting traces of these striations can be associated with a set of intersecting {111} planes on the fracture surface. Figure (35) is a map of the traces in Figure (34) and shows the corresponding stereographic projection of the {111} poles associated with that part of the fracture surface of No. 3

84A

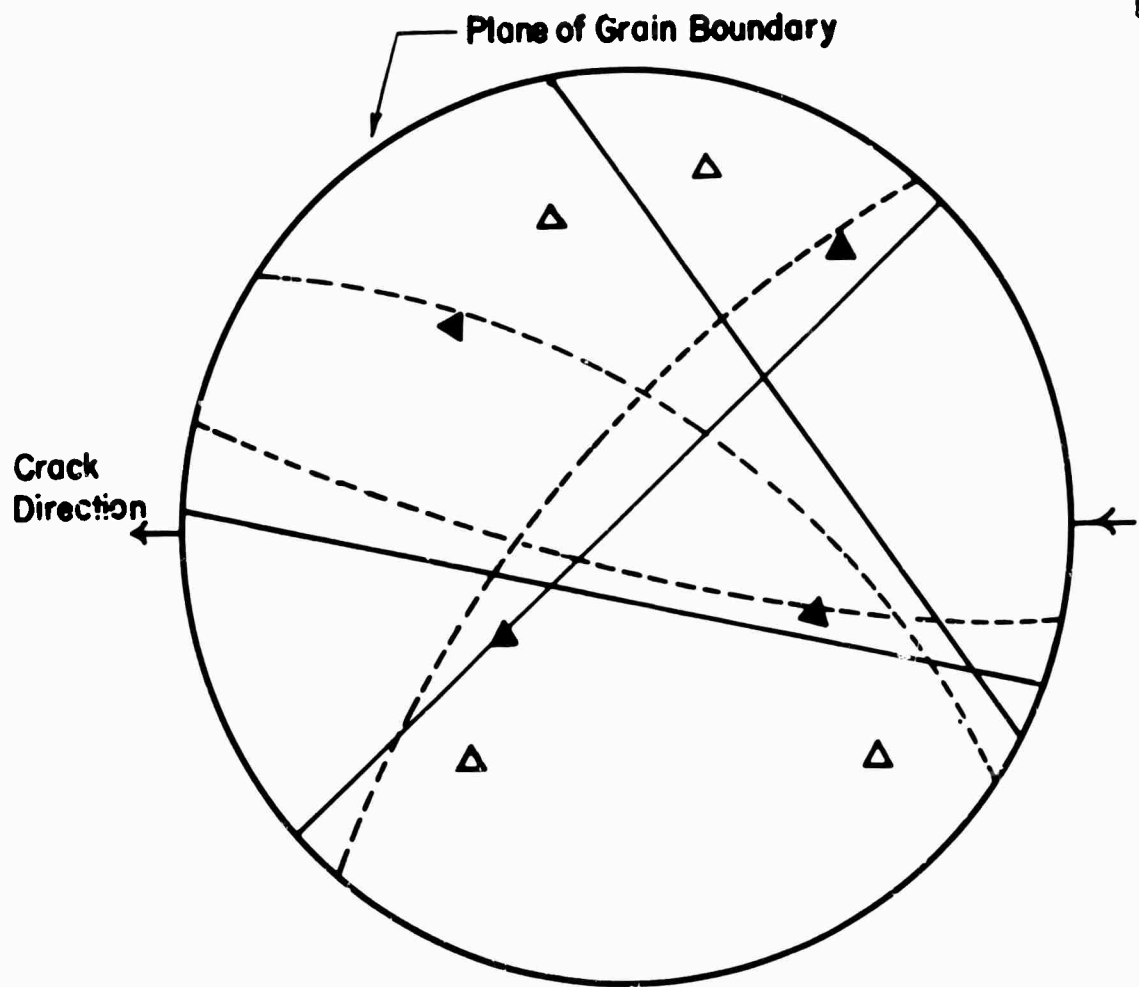


Part A: 450X, three distinct slip trace patterns on No. 3 bi-crystal fracture surface; Microstructure No. I fractured in 0.5M NaCl.



Part B: 1000X, blow up of Part A showing planar slip band spacing of approximately .1 to 1μ .

Figure 34.



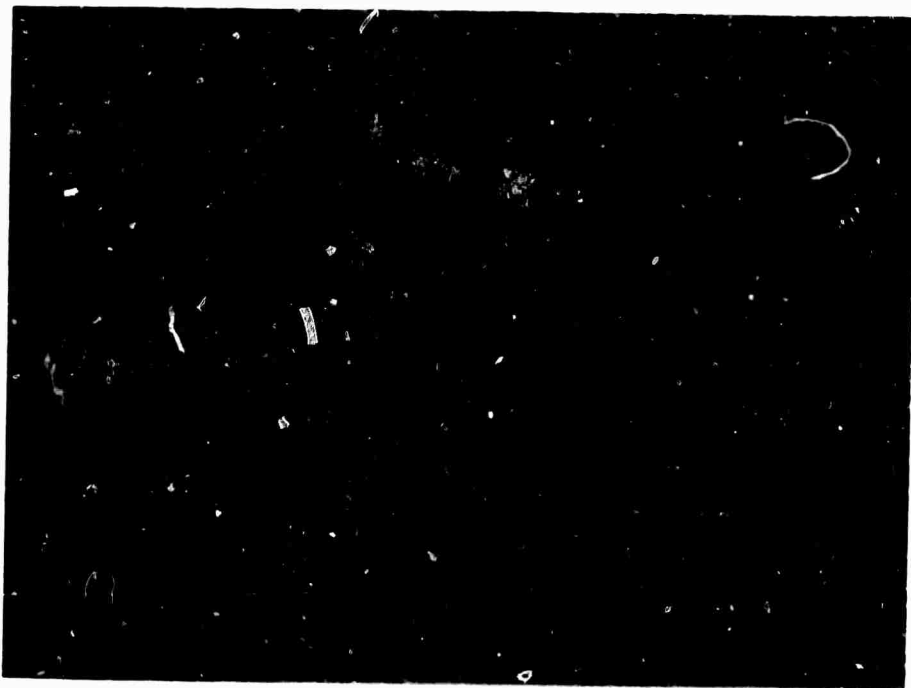
Bi-Crystal No. 3

Figure 35: Match up traces on No. 3 bi-crystal fracture surface with {111} slip planes for the known orientation of the bi-crystal.

- ▲ - Original orientation of (111) poles with crack direction also representing grain boundary trace.
- △ - Rotate ▲ 90° to move grain boundary surface into plane of paper.
- Trace of (111) slip planes
- _____ Slip traces from Picture No. 34.

bi-crystal. Since these traces can be paired up with a set of slip planes in each individual grain of the bi-crystal, it is likely they are slip traces and representative of the type of slip in the bulk material. A detailed description of the influence of microstructure on the dislocation distributions in the bulk material would require deformation studies involving transmission electron microscopy. Since studies of this type were not performed, it can only be inferred how deformation in the bulk material leads to the observed surface slip traces. With these considerations, a comparison will be made of the different types of surface slip patterns observed on the intergranular fracture surfaces of polycrystal and bi-crystal specimens. These slip patterns will be categorized according to the microstructure states (I, II, and III) discussed in section VI.B.

The resulting surface slip patterns for the intergranular fracture of microstructure No. I in 0.5M NaCl are shown in Figures (32), (34) parts A and B, and (36) parts A and B. The slip traces on No. 3 bi-crystal in Figure (34) parts A and B are typical of all bi-crystal failures and consist of clusters of discrete surface slip lines which are straight and show no apparent waviness. The distance between these individual slip lines is approximately .1 to 1μ . The fine nature of this planar slip is a result of the relatively low strain values necessary to cause bi-crystal failure in 0.5M NaCl. A similar surface appearance of the slip markings is noted on the polycrystal fracture surfaces for microstructure No. I, or the 50 min. age at 155°C . This is apparent in Figure (36) parts A and



Part A: 450X, fracture surface of No. 5 polycrystal tested in 0.5M NaCl; Microstructure No. I shows planar slip and pitting.

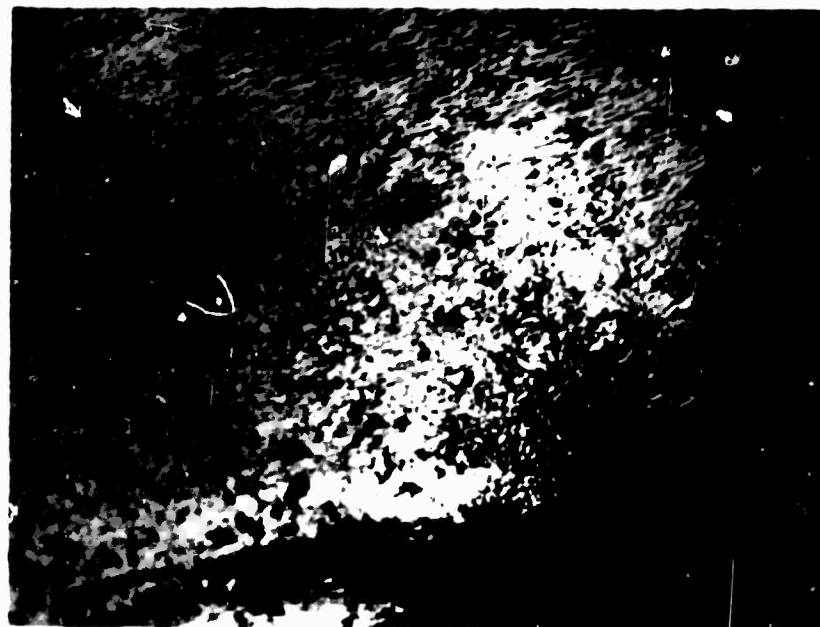


Part B: 1100X, blow up of Part A showing localized attack at Zn precipitate.

Figure 36.

B for No. 5 polycrystal tested in 0.5M NaCl. Aside from the planar slip markings in this figure, the polycrystal surface shows a limited degree of faceting and localized pitting at the zinc precipitate. Thus, it is evident that microstructure No. I produces planar slip markings.

The other two microstructures tested (Nos. II, III), aging for successive times of 500 and 5000 mins. at 155°C, produce observable differences in the surface slip markings. Figure (37) parts A and B shows the fracture surface of No. 7 polycrystal tested in air. At low magnifications, part A Figure (37), surface slip markings on this fracture surface are not readily visible. At a higher magnification, part B Figure (37), fine wavy slip lines become apparent, but the slip markings have lost the distinct linear appearance of those traces in Figure (36). Thus, the slip lines for microstructure No. II have become wavy and discontinuous in their surface appearance. The type of wavy slip resulting from microstructure No. III is exemplified on the polished surface of a bi-crystal specimen. This specimen shown in Figure (38) was deformed in air and depicts wavy-discontinuous slip lines. Consequently, microstructures Nos. II and III produce a more dispersed type surface slip pattern when compared to microstructure No. I. However, it is impossible to distinguish differences in the appearance of surface slip markings between microstructures Nos. II and III. Since changes in the surface slip band topography are not pronounced between these two microstructures, it would be necessary to use transmission electron microscopy to determine differences in the deformation character.



Part A: 275X, fracture surface of No. 7 polycrystal tested in air; Microstructure No. II shows fine-wavy slip.



Part B: 1100X, blow up of Part A showing details of wavy slip.

Figure 37.



Figure 38. 300X, slip traces for Microstructure No. III shown on the polished surface of a bi-crystal deformed in air; wavy slip lines.

However, this was not done, and it can only be inferred from the general trends observed in this work that dislocation distributions in the bulk material are more dispersed for microstructure No. III than No. II.

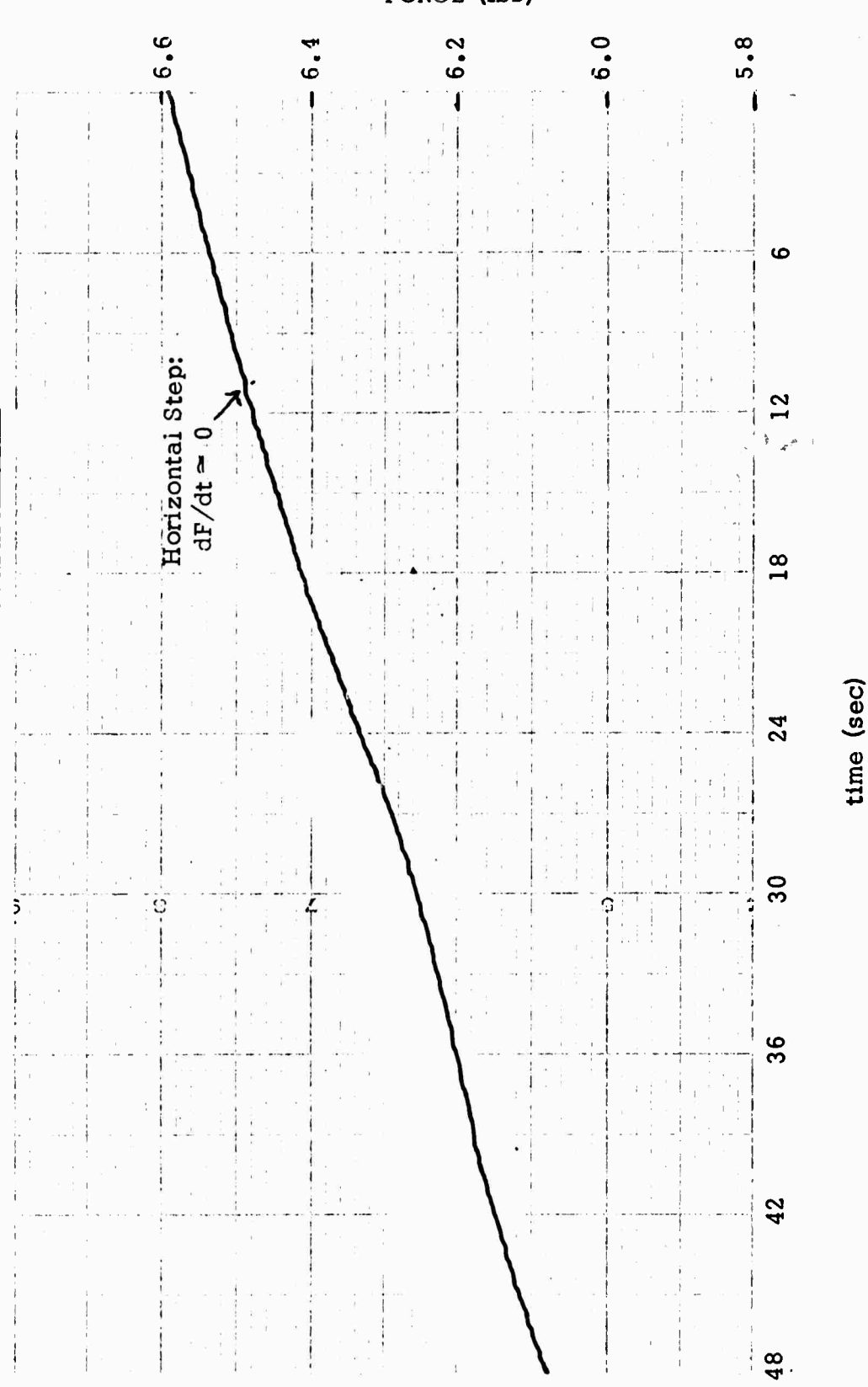
3. Stress Corrosion Pitting: The third general feature present on all fracture surfaces tested in 0.5M NaCl is the localized corrosion pitting at the second phase zinc precipitates. Localized pitting in the absence of stress was discussed previously, and transmission replicas in Figure (23) show the extent of these pits. There is no apparent difference between pits formed in the presence or absence of stress, and Figure (36) part B is typical of the general nature of pitting on all fractures in 0.5M NaCl. This picture shows the localized attack at the zinc precipitates on the fracture surface and the circular depressions formed. These observations would indicate that the zinc precipitate at the grain boundary is anodic with respect to the matrix and thus, undergoes local dissolution in the presence of a 0.5M NaCl electrolyte.

This type of preferential dissolution is not uncommon in the age hardenable aluminum alloys, and originally Dix^(43,44) showed the presence of a galvanic cell between the matrix and the grain boundary precipitate in an Al-Cu system. More recently, Helfrich⁽⁴⁵⁾ studied stress corrosion cracking in an age hardened Al-Zn-Mg alloy and found the rate controlling step in the process to be the anodic dissolution of $MgZn_2$ at grain boundaries.

D. Movement of Crack Front During Fracture:

At the inception of this work it was thought that bi-crystals would offer a sufficiently well defined geometry to determine whether intergranular fracture in this system was continuous or discontinuous in nature. A continuous cracking mechanism would imply that crack velocity is never zero. However, changes in velocity are probable with either acceleration or deceleration occurring during propagation. Contrary to this type of cracking, discontinuous propagation must proceed with points of zero velocity. Under fixed-grip conditions, a development of the expressions involving F , L , and t under a constant δ for the double cantilever beam geometry, Figure (5), shows crack velocity dL/dt to be proportional to the slope of load relaxation versus time, dF/dt : i.e. $dF/dt = (dF/dL) \cdot V$. Since dF/dL is a geometric factor and independent of time, the crack velocity V is directly related to dF/dt . Thus, by monitoring the Instron trace of load relaxation it is possible to determine the nature of crack propagation (continuous or discontinuous). By utilizing optimum sensitivity on the Instron, it is possible to observe changes in load of $\pm 5 \times 10^{-3}$ lbs over a time of $\pm 3 \cdot 10^{-1}$ sec. The load relaxation accompanying crack propagation in a bi-crystal is shown in Figure (39). In this figure it is noticed on a fine scale that horizontal steps, approximately 0.6 sec. in duration and spacing, exist during crack propagation. This type of trace would indicate points where $dF/dt \approx 0$, and thus the corresponding crack velocity $dL/dt \approx 0$. Without further evidence of a substructure (faceting) on the bi-crystal grain boundary, it

INSTRON TRACE OF FORCE VERSUS CRACKING TIME



88A

Figure 39: Load relaxation trace of a Bi-crystal DCB specimen tested in 0.5M NaCl; the trace shows the periodic occurrence of horizontal steps, i.e., $dF/dt \approx 0$.

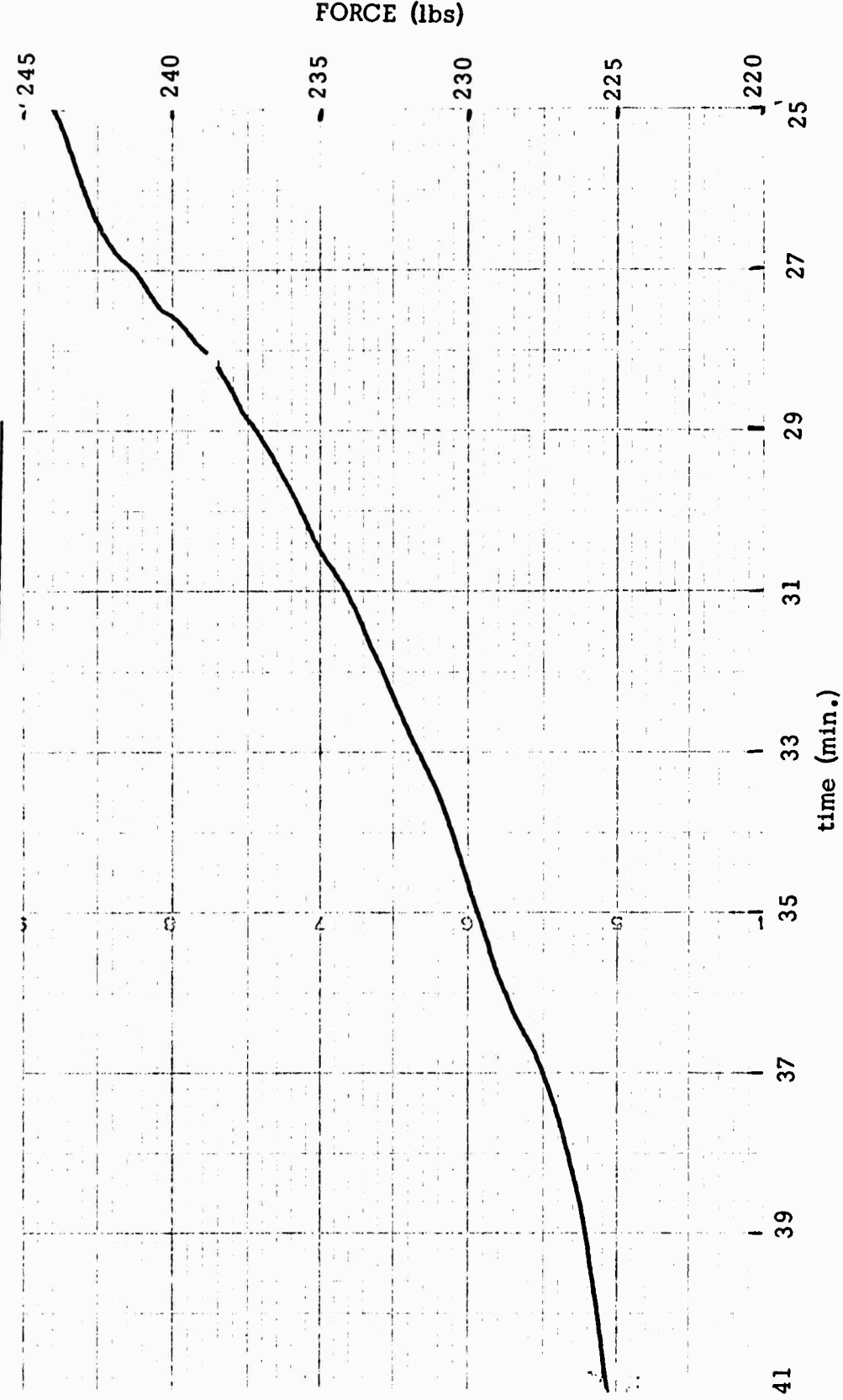
could be concluded that the trace in Figure (39) represents a discontinuous fracture process. However, the number of horizontal steps in Figure (39) (approximately 15 steps for a 0.1 lb load drop) corresponds to the number of faceted steps in Figure (32), over the crack length increment 0.83 mm, which is equivalent to the 0.1 lb load drop. Thus, it is concluded that the discontinuous cracking process is a result of the faceted grain boundary structure and not due to an inherent fracture mechanism.

A similar Instron trace for load relaxation during crack propagation in a polycrystal specimen is shown in Figure (40). Unlike the trace in Figure (39), there is no indication of fine horizontal steps, $dF/dt \approx 0$, existing. However, this figure does show several sharp load drops over relatively short periods of time. These load drops on Figure (40) are attributed to rapid grain boundary fractures of individual equi-axed grains in the aggregate. With an average grain diameter of approximately .5 to 1 mm and a cracking cross section of 4.2 mm, about 5 to 8 equi-axed grains should span the planar crack front; see Figure 28 part A. These numbers would indicate an average of approximately 5 to 8 sharp changes in dF/dt over a cracking increment roughly equal to the grain size. This is generally observed on Instron traces for polycrystal fracture.

E. Influence of Microstructure on the Slip Band Structure:

The relation of microstructure to intergranular fracture in the Al-Zn system will be shown to be determined by the deformation processes in the

INSTRON TRACE OF FORCE VERSUS CRACKING TIME



89A

Figure 40: Load relaxation trace of a polycrystal DCB specimen tested in air; the trace shows irregular changes in the slope, dF/dt , attributed to the equi-axed grain size of the test specimens.

matrix. The recent discussion on surface topography has shown the following correlation between microstructure and observed surface slip patterns: Microstructure No. I produces a coarse-planar type of surface slip while Microstructures II and III produce a wavy-dispersed type surface slip pattern. When related to the matrix microstructure, the coarse slip is associated with a high volume fraction of G.P. zones, and a lower volume fraction of G.P. zones produces a dispersed type slip in the matrix leading to wavy surface slip lines. A similar type of behavior has been reported in the aluminum-4% copper alloys where the slip bands change from coarse, single slip lines to lamellated slip during the sequence⁽⁴⁶⁾:

$$\text{G.P. [1]} \rightarrow \text{G.P. [2]} \rightarrow \theta'.$$

In this system, Thomas and Nutting showed that for approximately equivalent strains, the slip displacements on the surface increase (become coarser) as more G.P. [1] zones form with aging. This is analogous to the trends observed between the microstructures tested in the Al-Zn system. The suggested explanation for this effect is that the increase in formation of G.P. [1] zones makes it more difficult for dislocation sources to become active, and thus reduces the number of active slip systems. Such an effect would be associated with an increase in hardness, and this is observed. However, it is difficult to decide from experimental evidence what interaction or effect in the matrix produces the observed slip line patterns for different volume fractions of G.P. zones.

Aside from differences in the slip properties between G.P. zone structures, it is a general observation for all crystalline materials that as the yield

strength is increased, i.e., by alloying, precipitation hardening, lowering temperature etc., slip lines become fewer and coarser^(41,42). This observation is noted in all age hardenable Al systems where coarse slip is associated with the G.P. zone structure just prior to peak hardness and fine slip with the stable incoherent precipitate in the overaged condition. Elucidation of this experimental result justifies a discussion of dislocation interactions with coherent, semi-coherent, and incoherent precipitates.

When a fine precipitate is formed in a solid solution, an additional barrier to the movement of dislocations is created. The precipitate particles will lie across the slip planes along which dislocations move, so that the dislocations must behave in one of two ways:

1. Cut through the particles of precipitate.
2. Take a path around the obstacles.

While it is difficult to observe these interactions even in the electron microscope, the first mechanism is thought to predominate in lightly aged alloys with very fine coherent precipitates, or G.P. zones, while the second mechanism is more characteristic of overaged alloys with coarser dispersions of precipitates. Thus, the slip traces on a polished surface should undergo marked changes dependent on the degree of aging. Crystals containing G.P. zones deform on the slip plane on which the resolved shear stress is highest, and the zones are sheared by the passage of the dislocations. The crystals change shape in a way expected from slip on one system of slip planes⁽⁴⁷⁾. On the

other hand, Al-Cu crystals aged to peak hardness and containing θ' precipitate do not always change shape like single crystals deforming on one system and behave more like polycrystalline material. This suggests that a number of slip systems are equally favored and leads to less well defined slip traces. This trend appears to become more pronounced in the overaged condition.

Electron microscopic examination has shown conclusively that G.P. zones are cut by dislocations. The following zones and phases have been reported as being sheared by dislocations^(48,17); G.P. 1, G.P. 2, and θ' in Al-Cu, G.P. zones in Al-Zn, and γ' in Al-Ag. However, whether or not a phase is cut by a dislocation will depend on the extent of plastic deformation; it is likely that semi-coherent precipitates such as θ' and γ' are not cut during small deformations, but only after heavier deformation. It seems generally agreed that incoherent precipitates such as θ in Al-Cu are not cut by dislocations, but may fracture after heavy deformation.

The general trend appears to be that particles of 200\AA diameter or less which are coherent, will deform with the matrix from the start, but particles up to 1000\AA which are at least semi-coherent may be sheared by dislocations at heavier deformations. However, substantial evidence exists for incoherent particles holding up dislocation lines prior to bowing out between them; resulting in residual loops around the particles⁽⁴⁹⁾ and increasing the opportunity of cross slip for successive dislocations.

From the preceding discussion, it is plausible to assume all G.P. zone

sizes in the Al-Zn system are sheared by dislocations and offer little resistance to successive deformation on the same slip plane. Thus, an explanation for the relation between observed slip characteristics on the surface and the volume fraction of G.P. zones in the matrix might involve a description of differences in dislocation sources; as originally suggested by Thomas and Nutting⁽⁴⁶⁾. If this is the case, the observed trends in slip patterns in the Al-Zn system would indicate that microstructure (No. I) with the high volume fraction of G.P. zones would have a considerably smaller number of active dislocation sources than microstructures (Nos. II and III) with the smaller volume fraction of zones.

F. Interpretation of Dependence of Fracture Toughness on Microstructure:

This section will interpret and show the compatibility of present results on the threshold toughness K_c ($V \rightarrow 0$) in the Al-Zn system with other fracture studies done on different microstructures in a commercial alloy system. From the previous discussion of the influence of microstructure on the deformation processes in the matrix, general trends can be stated for age hardenable Al alloys. These observations are cross referenced in the following table under the characteristics of strength, microstructure, and the resulting deformation mode.

<u>STRENGTH</u>	<u>MICROSTRUCTURE</u>	<u>SLIP PROPERTIES</u>
Underaged	{A - Saturated solid solution B - Small Volume Fraction of G.P. zones.	Fine
Peak Strength	A - Large Volume Fraction of G.P. zones.	Coarse
Overaged	{A - Semi-coherent Precipitate B - Incoherent Precipitate	Fine

This table will be used as a basis for comparing fracture toughness, i.e. K_c at crack instability, in a commercial Al-Zn-Mg alloy with the threshold toughness, K_c ($V \rightarrow 0$), results in the Al-Zn system. Recently, the plane-strain fracture toughness for different microstructures was determined in an Al-7% Zn-2.3% Mg alloy⁽⁵¹⁾. Although no correlation with the deformation processes was made, the following table summarizes the results:

Plane Strain Fracture Toughness for
an Al-7% Zn-2.3% Mg Alloy

STRENGTH		FRACTURE TOUGHNESS* $\text{kgs/cm}^{3/2}$
CONDITION	YIELD STRENGTH 10^3 psi	
Underaged	66	7300
Peak Strength	77	4270
Overaged	65	5400

* K_c : Stress intensity factor at crack instability measured by pop-in.

The general observation from this table is that the microstructure corresponding into to peak strength has a lower fracture toughness value than either micro-structure in the over-or-underaged state. Thus, a comparison of the two tables would indicate inhomogeneous plastic flow, or coarse slip, in the matrix lowers the fracture toughness when compared to microstructures producing fine dispersed type slip. This trend is substantiated in the Al-Zn system for micro-structures composed of different volume fractions of G.P. zones. The following

table lists the corresponding threshold toughness values, microstructures, and observed slip traces in the Al-Zn system.

**Condition	Strength		Slip Traces
	Yield Strength (10^3 psi)	Threshold* Toughness $3/2$ (kgs/cm)	
Large Volume Fraction of G.P. zones (f_1)	21.5	1600	Planar
Smaller Volume Fraction of zones (f_2)	19.0	1875	Wavy
(f_3)	15.8	>2625	Wavy

{* K_c ($V=0$): Extrapolated stress intensity factor to zero velocity
{** $f_1 > f_2 > f_3$ (Volume Fractions of G.P. zones)}

This table shows that the preceding trend holds, and microstructures producing coarse-planar slip have a lower threshold toughness value than microstructures with fine-wavy slip. Thus, the type of deformation and its relation to microstructure is the controlling metallurgical variable on a material's resistance to fracture. The quantitative explanation of this effect will be developed in section VII. Briefly, this explanation is based on inhomogeneous slip in the matrix being blocked at grain boundaries and causing severe stress concentrations. Thus, the higher the stress concentrations the lower the critical stress intensity factor necessary to cause intergranular fracture, and as slip becomes homogeneous in the matrix, higher critical stress intensity factors can be tolerated.

G. Interpretation of the Dependence of Stress-Corrosion Cracking Susceptibility on Microstructure:

Assuming the presence of a corrosive environment does not affect plastic flow properties within the matrix, a microstructure which corresponds to a susceptible condition for fracture in air might also hold for fracture in a corrosive environment. However, the addition of a corrosive environment should manifest itself by a difference in cracking kinetics between fracture in air and in a chemically active environment at a constant stress intensity factor. A quantitative comparison has been made in section V.E between cracking velocities and stress intensity factors for fracture in air and in 0.5M NaCl. The difference between intergranular fracture in these two environments can be accounted for by assuming the corrosive environment either causes preferential anodic attack or surface adsorption. Both of these effects would tend to lower the fracture criteria along the preferential sites and result in larger cracking velocities than fracture in air.

Since the preferential attack of the second phase zinc precipitate at grain boundaries has been demonstrated in this alloy system, i.e. section V.F, it would appear the 0.5M NaCl environment sets up a galvanic cell between the Zn precipitate and the matrix. Thus, the alternate explanation, of complex ion adsorption on the crack front lowering the inherent surface energy of the system, need not be invoked for Al-Zn tested in a NaCl solution. Aside from the electrochemical nature of the phenomenon, there appears to be a common, underlying

mechanical affect for the intergranular fracture of this system in air, distilled water, and 0.5M NaCl. The common dependence of cracking velocity being proportional to the square of the stress intensity factor is noted for all three test environments (Eq. (V.1)). This relation suggests that the mechanical effect in the matrix is the controlling variable for susceptibility to intergranular fracture, irrespective of environment. If the mechanical effect depends on microstructure, the same trends noted between threshold toughness and microstructure should also be apparent between stress corrosion cracking susceptibility and microstructure. The table below lists microstructure, susceptibility to fracture in 0.5M NaCl, and deformation mode. The susceptibility between microstructures is determined from Figure (22) by drawing an iso-velocity (horizontal line) at 2×10^{-3} cm/min.

** Condition	Strength		Slip Traces
	Yield Strength (10^3 psi)	* Stress Intensity Factor $K_c(V)$ $kgs/cm^{3/2}$	
Large Volume Fraction of G.P. zones (f_1)	21.5	310	Planar
Smaller Volume Fraction of zones (f_2)	19.0	1300	Wavy
(f_3)	15.8	> 2625	Wavy

* $K_c(V)$: Obtained at $V = 2 \times 10^{-3}$ cm/min. from Figure (22).

** $f_1 > f_2 > f_3$ (Volume Fractions of G.P. zones).

The same trends are apparent from this table as previously shown for threshold toughness. Planar slip appears to cause stress concentrations at the grain boundaries and decreases the resistance to stress corrosion cracking. However, microstructures producing homogeneous slip in the matrix, exemplified by wavy traces on the surface, do not cause high stress concentrations when the slip is blocked by grain boundaries. Thus, these microstructures are more resistant to intergranular fracture.

These trends observed in the Al-Zn system have also been substantiated for intergranular fracture in an Al-Zn-Mg system by Pugh⁽⁵²⁾. In general, the stress corrosion life of an age hardenable aluminum alloy is known to decrease with increasing aging time to a minimum value, after which it progressively increases^(52,53). Thus, the common explanation appears to be the influence of microstructure on the deformation mode, which in turn determines the resistance or susceptibility to intergranular fracture. The explanation can be re-inforced by showing that the matrix precipitates are more important than grain boundary precipitates in the intergranular fracture process of the Al-Zn system.

Assuming the deformation process is controlled by matrix precipitates, then it follows that matrix and not grain boundary precipitates should directly influence susceptibility to stress corrosion cracking. This assumption hinges on the effect that a solute depleted zone or precipitate denuded zone adjacent to the grain boundary plays no part in bulk deformation, and thus doesn't influence stress corrosion properties. Recently, this has been shown to be

correct in the Al-Zn-Mg system⁽⁵⁴⁾. Similary, if matrix precipitates are the controlling structure in the Al-Zn system, then this strengthens the explanation based on the type of deformation, i.e. coarse or fine slip. The following table is a comparison of stress-corrosion cracking susceptibilities for three different microstructures. The relative volume fractions are listed for matrix and grain boundary precipitates corresponding to cracking velocities for a constant stress intensity factor of 1220 kgs/cm^{3/2}.

Microstructure	*Condition		Yield Strength (10 ³ psi)	**Crack Velocity for Constant Stress Intensity Factor V(K) (cm/min)
	Matrix ppt	Grain Boundary ppt		
No. I: Age 50 min at 155°C and 100 hrs at room temperature.	f_1	η_1	21.5	18.0×10^{-3}
No. IV: Age 15 min at 155°C and 100 hrs at room temperature.	f_1	η_2	21.5	12.0×10^{-3}
No. V: Age 50 min at 155°C and 2 hrs at room temperature.	f_2	η_1	10.1	0.0

{ * $f_1 >> f_2$ (Volume Fraction of G.P. zones).

$\eta_1 \gtrsim \eta_2$ (Volume Fraction of Zn precipitate at grain boundary).

**Values taken from Figure No. 22 for $K = 1220 \text{ kgs-cm}^{-3/2}$ and Table 13, Appendix I-A.

An estimate of the relative magnitudes of f_1 and f_2 in the matrix can be made by assuming the yield strength is proportional to the square root of the volume fraction of G.P. zones in the matrix, i.e., $f^{1/2}$. This assumption is justified by recent work of Price and Kelly⁽²⁸⁾ and Dash and Fine⁽³²⁾ who showed strengthening in the Al-Zn system to be proportional to $f^{1/2}$. Thus, the yield strength, Y.S., of a G.P. zone strengthened matrix may be approximated as

$$Y.S. = A + B \times f^{1/2} \quad (VI.1)$$

where A and B are material constants. The constant "A" is the Y.S. intercept at $f^{1/2} = 0$ and corresponds to a saturated solid solution. From Figure (12), "A" is estimated at 7,000 psi. Knowing the respective bulk yield strengths corresponding to the matrix precipitates f_1 and f_2 , Eq. (VI.1) is used to calculate a ratio $f_1/f_2 \approx 25$ for the microstructures in the preceding table.

An estimate of the differences between the volume fraction of grain boundary precipitates, η_1 and η_2 , is based on the different aging or diffusion times at 155°C, i.e., 15 min. and 50 min. If it is assumed that the growth of a spherical particle at a grain boundary is proportional to the square root of the time, t , at the diffusion temperature⁽¹⁰⁵⁾, then $\eta_1/\eta_2 = 6$. The calculations for $f_1/f_2 = 25$ and $\eta_1/\eta_2 = 6$ were made to obtain some idea of the magnitude of the change in microstructure, and it is emphasized that these calculations are offered only as rough estimates.

The preceding table points out the importance of matrix precipitates (f_1, f_2) over grain boundary precipitates (η_1, η_2). Microstructures with slightly

different volume fractions of grain boundary precipitates but the same bulk matrix precipitate, f_1 , crack at approximately the same velocity, $(18 \sim 12) \times 10^{-3}$ cm/min. under a fixed stress intensity factor. A comparison between microstructures (I) and (V) shows a distinct change in the matrix precipitate $f_1 \gg f_2$, as exemplified by the difference in the yield strengths. These microstructures have approximately a constant volume fraction of grain boundary precipitate but show a large shift in cracking susceptibility. Thus, it appears the volume fraction of G.P. zones, or the matrix precipitate, is the controlling structure for stress corrosion cracking susceptibility.

H. Bi-crystal Susceptibility to Stress Corrosion Cracking:

The polycrystal results have shown that the deformation mode as influenced by microstructure is a controlling variable in determining susceptibility to intergranular fracture in air and in 0.5M NaCl. The validity of this result is further substantiated by the effects of orientation on bi-crystal susceptibility. The bi-crystal tests were performed to determine the affect of the orientation of adjacent grains to a grain boundary on the intergranular fracture process. The results of this study were presented previously in section V.G, and the following general conclusion was reached: the larger the number of coincident slip systems (parallel (111) slip planes and <110> slip directions) between adjacent grains of a bi-crystal specimen; the greater the resistance to stress-corrosion cracking. This coincidence of slip systems across a grain boundary will be referred to as "slip band continuity". Figure (41) shows partial continuity of one

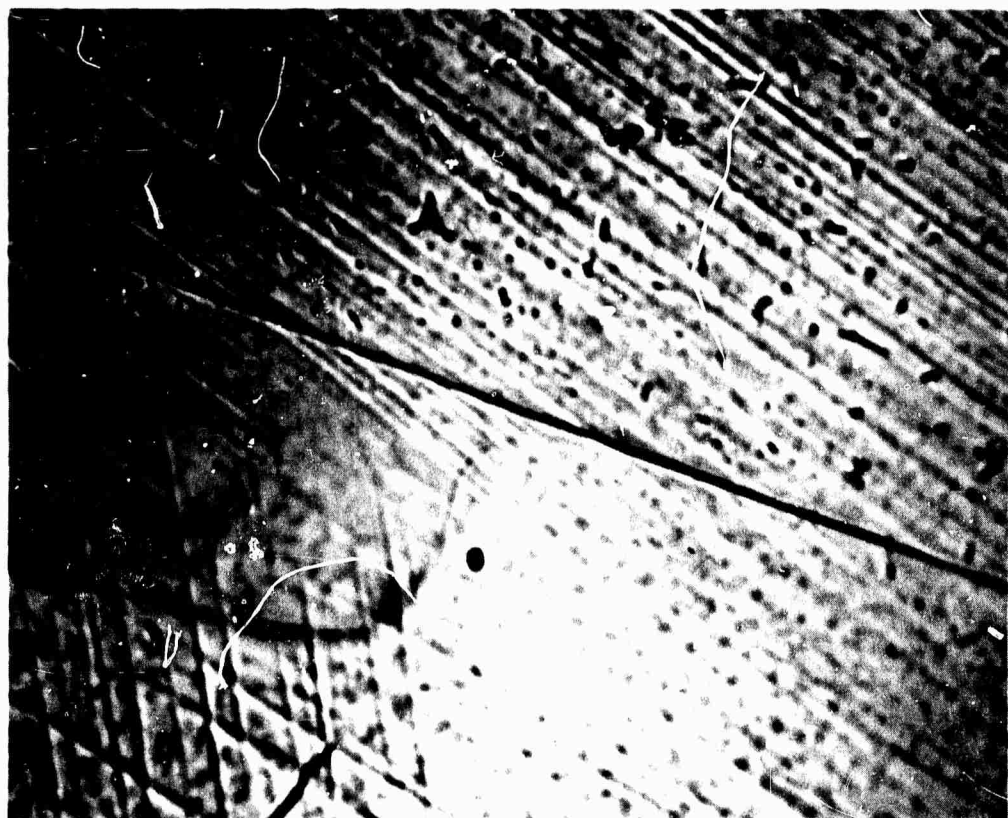


Figure 41. 450X, polished bi-crystal surface for Microstructure No. I showing planar slip coincidence across grain boundary; one set of slip systems $\{111\}$ planes and $\langle 110 \rangle$ directions in each grain adjacent to the grain boundary parallel.

set of slip systems across the grain boundary of No. 6 bi-crystal, i.e. micro-structure No. I producing planar slip traces. From this figure it becomes evident that planar slip is not blocked at a grain boundary when the slip systems of adjacent grains are parallel. The grain boundary does not interfere with the transmission of the deformation from one grain to another without distorting the slip plane and direction. This type of behavior was first investigated by Ogilvie⁽⁵⁵⁾ working with polycrystal aluminum and α -brass. He found that continuity of slip bands occurred when both slip planes and directions of the adjacent grains are within 2° of one another. This restriction proved too severe for slip band continuity, and a latter investigation⁽⁵⁶⁾ extended the divergence between slip systems to approximately 10° to 20° . It should be noted that the criterion used for determining the coincidence of slip systems in regions A, B, and C of Figure (24) was 15° .

A further investigation by Kratochvílova and Sestak⁽⁵⁷⁾ showed good continuity for all small angle boundaries, whereas for large angle boundaries those slip bands associated with dislocations of predominantly edge character gave the best continuity. Screw dislocations were wavy and tended to spread when impinging on the boundary. A characterization of screw or edge slip bands was not made in this study on Al-Zn bi-crystals; however, a simple tilt or twist grain boundary of approximately 5° was the most resistant orientation to stress corrosion cracking. The stereographic projection of No. 31 bi-crystal, Figure (25), shows this type of low angle boundary to have complete coincidence

of adjacent slip systems. Koppenaal⁽⁵⁸⁾ and Usikov⁽⁵⁹⁾ have observed continuous slip bands across grain boundaries and inferred that the mechanism was one of stress activation of sources along the boundary. Stroh's⁽⁶⁰⁾ treatment for stresses near the head of a dislocation pile-up, which is representative of a slip band, also predicted the stress activation of sources at the grain boundaries in aluminum⁽⁵⁶⁾. Whether such singular, discrete pile-ups occur is immaterial since the analysis is a good approximation, in that the stress distribution at the head of a blocked slip band must be similar in form to that of a free-slipping crack. Eshelby⁽⁶¹⁾ pointed out that the stresses ahead of such a crack are the same as those at the head of a dislocation pile-up.

The question to be answered is how the severe stress concentrations at the head of a blocked slip band are relaxed. Johnston^(62, 63) has shown for MgO that whether the shear stress concentration of the slip band injects dislocations into the neighboring grain before the tensile stress concentration nucleates a crack depends upon the orientation of the two grains. The probability for slipping is greatest when the orientations are practically the same, i.e., for small angle tilt or twist boundaries, since the maximum shear stress concentration ahead of the pile-up is then applied over a slip plane of the adjacent grain. There are certain intermediate misorientations, i.e., 1, 2, or 3 sets of coincident slip systems, for which slip bands will be oriented to produce slip in the adjacent grain while the other operating slip systems will tend to assist intergranular crack nucleation through tensile stress concentrations.

Finally, all operating slip systems in orientations where no slip coincidence exists should aid crack nucleation and growth. This trend is observed, see section V.G and Figure (24), for intergranular stress corrosion cracking in the Al-Zn system. Also, it is important to note that in a typical randomly oriented polycrystalline aggregate, the majority of grains have large relative misorientations so that the cracking susceptibility of a polycrystal specimen should lie toward regions A and B on Figure (24). This trend is observed when comparing polycrystal and bi-crystal tests, section V.H. Thus, to improve the resistance to intergranular fracture, a highly oriented texture, similar to Region C in Figure (24), would be necessary to accommodate slip from grain to grain without fracture.

Having categorized the trends for orientations between regions A, B, and C of Figure (24), some mention should be made of the different susceptibilities obtained for bi-crystals in the same Region, i.e., A, B, or C. To distinguish between the susceptibility of orientations in the same region, two criteria are needed:

1 - A determination of the operating slip systems for a given orientation and state of stress.

2 - A model to calculate the effect of slip band blockage and the resulting tensile stress concentration at the grain boundary from each operating slip system.

It is possible that the operative slip systems at the tip of a bi-crystal crack

could be selected with the following assumptions:

(i) The critical resolved shear stress for slip is the same on all possible slip systems; critical shear stress law.

(ii) Strain compatibility across the grain boundary. It has been shown⁽¹⁵⁾ that in the general case for strain compatibility, at least four slip systems are required to operate at the grain boundary of a bi-crystal, i.e., distributed as one-three or two-two between the component crystals.

(iii) A maximum in the external work for the unique set of operating slip systems.

If these three assumptions proved useful in selecting a unique set of slip systems for a particular bi-crystal orientation and stress state, then an appropriate model could be invoked to describe the effective tensile stress concentration σ_c for slip band blockage at a grain boundary. Such a model describing σ_c ahead of a dislocation pile-up is discussed in the next section, i.e., Eq. (VII.6).

It is suggested that the summation of the effective tensile stress concentration for each of the unique operating slip systems, i.e.,

$$\sum_{i=1}^N \sigma_c (i)$$

where N is the number of operating slip systems, is the critical parameter for determining susceptibility to intergranular fracture.

Thus, if this procedure were carried out on the orientations in regions A

and B of Figure (24); the most susceptible orientations in either region would be those contributing to the highest cumulative tensile stress concentration from the operating slip systems, i.e., maximum

$$\sum_{i=1}^N \sigma_c(i) .$$

This concludes the qualitative discussion of intergranular fracture in air and in 0.5M NaCl. However, it is apparent that the mode of deformation (planar or wavy slip) as determined by microstructure and the degree or extent of slip band blockage at grain boundaries as determined by orientation are the controlling variables to intergranular fracture. These results will now be combined to form a quantitative description of the intergranular fracture process.

VII. Theoretical Formalism For Intergranular Fracture In Air and In A Corrosive Environment.

A. Introduction:

This section will propose a model for intergranular fracture in air and in a corrosive environment. Initially, a review of the literature discussed intergranular crack nucleation in air, and a plausible mechanism to account for the time dependence of crack initiation was cited and attributed to Rosenfield and Hahn⁽⁸⁰⁾. The results of this present study on Al-Zn indicate that time dependent fracture in air or in a corrosive environment is primarily controlled by the mode of slip, coarse or fine, in the matrix. Also, other results^(74,79) would tend to indicate that the sensitivity of dislocation velocity or mobility to shear stress should be a controlling variable in the fracture process. Thus, a partial understanding of the general problem of fracture involves a description of dislocation motion and configuration as a function of temperature, microstructure, and stress.

Also, it is noted that the effects discussed so far are related to a particular system in the absence of a corrosive environment. When environment is added the complexity of the problem increases, and two distinct yet related variables are encountered:

1 - Metallurgical

2 - Chemical

Reduced to simpler terms, it appears that the large amount of empirical information concerning the phenomenon of intergranular stress corrosion cracking may be

simplified to two necessary and sufficient conditions:

- 1 - The existence of a structural path at which the intensity of chemical reactivity is high relative to the surrounding matrix.
- 2 - A mechanism for concentration of a normal stress across the path of chemical reactivity.

Any proposed mechanism to explain intergranular stress corrosion must deal with the interrelation of the above criteria. A useful introduction into the complexity of the problem is the electrochemical theory proposed by Dix⁽⁴⁴⁾. According to this generalized model, a prerequisite for stress corrosion cracking is the existence of a localized anodic path in the material. In working with the age hardenable Al-Cu system, Dix found grain boundaries to be anodic with respect to the matrix. Thus, in the presence of a corrosive aqueous environment and a tensile stress, a galvanic cell is set up in which the anodic path is preferentially attacked. The base of the resulting corrosion crevice then becomes the site of stress concentrations, and these were thought to cause the metal to "tear apart by mechanical action". It was considered that the tearing action exposes fresh metal, unprotected by films, so that accelerated corrosion occurs in this region. This in-turn leads to further stress concentration and further tearing of the metal. While this model accounts for the apparent electrochemical nature of stress corrosion cracking, it leaves unanswered the principal question concerning the phase "tearing apart by mechanical action". An understanding of this phase requires some insight into the theory behind the

fracture of crystalline materials, and this topic will be discussed in following sections.

B. Crack Initiation In Air:

A theoretical development concerning intergranular fracture kinetics must start with a basic foundation for the criterion of fracture. Once this has been established, the development may be expanded to account for the time dependence of fracture, and thus, offer an explanation for cracking kinetics. Initially, we start by considering the conditions under which a crack will form in a crystalline material. As a first assumption in the formation or growth of a crack, only the component of stress normal to the plane of the crack will be considered. This assumption simplifies the stress state at the crack tip and ignores bi-axial or tri-axial stress states and discards any direct contribution of shear stresses. However, in the subsequent development of this theory, it will be shown that shear stresses indirectly contribute to an added tensile stress, above the applied tensile stress.

The other assumed criteria for fracture are: the tensile stress at the crack tip must approach the true fracture stress, i.e. cohesive strength, of the material. However, it is not sufficient merely to specify the tensile stress at a single point, for if this were so a single dislocation could produce a crack. The necessary additional condition may be obtained by requiring that the formation of the crack is to be accompanied by a decrease in the energy of the system (refer to Figure (9)). With these initial assumptions, we are able to

treat a two dimensional problem concerning crack formation. Figure (42) shows the essential features required to define crack initiation in a system with a macroscopic crack under an applied stress, σ_{applied} . The criteria for crack initiation in this system can now be stated as: fracture occurs when the tensile stress at the crack tip, $\sigma_{yy}^{\text{total}}$, is equal to the inherent fracture stress of the system, σ_{fracture} . To reach the critical material constant σ_{fracture} , it becomes necessary to describe how the tensile stress $\sigma_{yy}^{\text{total}}$, can increase above its instantaneous response to the applied stress, σ_{applied} , on the system. A description of the fracture criteria can now be stated as

$$\sigma_{\text{fracture}} = \sigma_{yy}^{\text{(instantaneous)}} + \sigma_{yy}^{\text{(time dependent)}}. \quad (\text{VII.1})$$

The total normal tensile stress at the crack tip becomes the sum of an immediate response to the applied stress on the system $\sigma_{yy}^{\text{(instantaneous)}}$ plus a time dependent stress $\sigma_{yy}^{\text{(time dependent)}}$ described by a hypothetical model.

1. Description of σ_{yy} Time Dependent:

Cottrell⁽⁹⁸⁾ and Eshelby, Frank, and Nabarro⁽⁶¹⁾ investigated the shear stress concentration which would be produced if a group of like edge dislocations moving in a single glide plane were blocked and piled-up against a barrier. Both of these analyses led to the conclusion that the shear stress would be increased locally, at the leading end of the pile-up, by a factor N , where N is the number of dislocations in the pile-up. Koehler⁽⁵⁰⁾ then pointed out that, in addition to a shear stress concentration ahead of a pile-up, a large tensile

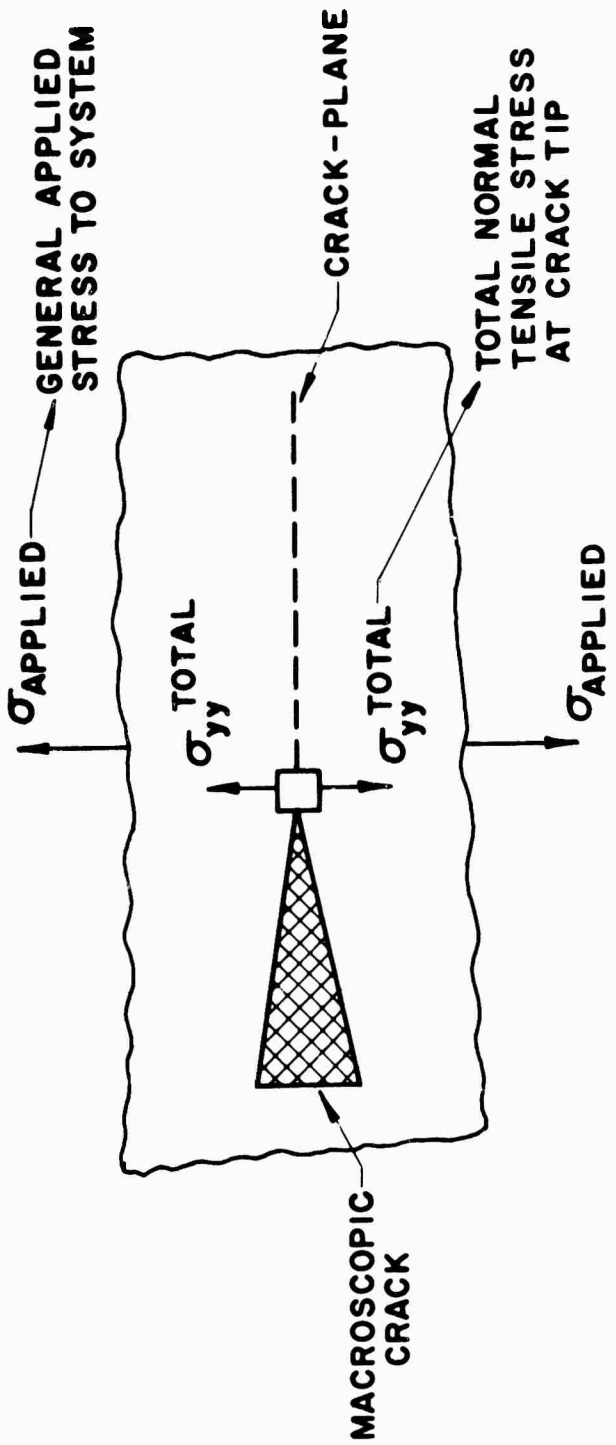


Figure 42. Schematic drawing showing the total normal stress across a fracture plane ahead of a macroscopic crack.

III.

stress, of approximately the same magnitude as the shear stress, would result at the end of a pile-up. Mott⁽⁹⁹⁾ then suggested that these large tensile stresses might be sufficient to initiate fracture by slip, and this model was investigated in some detail by Stroh^(60,77).

Figure (43) is a schematic drawing of Stroh's model and shows edge dislocations piled-up at an obstacle, i.e. a grain boundary in this case, and causing a high tensile stress concentration. The results of Stroh's model indicate that the normal stress concentration, $\sigma_{\text{concentration}} \equiv \sigma_c$, acting normal to the grain boundary a distance ρ from the pile-up is:

$$\sigma_c = 3/2 \left[\frac{d(N)}{\rho} \right]^{1/2} \tau_{x'y'} \sin \varphi \cos 1/2 \varphi. \quad (\text{VII.2})$$

The quantity $d(N)$, length of dislocation pile-up on slip plane, can also be expressed as:

$$d(N) = \mu b n / \pi (1 - \nu) \tau_{x'y'} \quad (\text{VII.3})$$

μ = shear modulus

b = Burger's vector

ν = Poisson's ratio

n = number of dislocations in the pile-up

$\tau_{x'y'}$ = applied shear stress on slip plane.

Provided N is sufficiently large ($N \gg 1$), this expression for $d(N)$ is accurate for the subsequent calculations involving pile-ups⁽¹⁰⁰⁾. In Stroh's original model, $\tau_{x'y'}$ was considered constant over the active slip plane and independent of the angle φ from the blocking obstacle, i.e., grain boundary in Figure (43). However, this assumption is too restrictive when dealing with the shear

111A

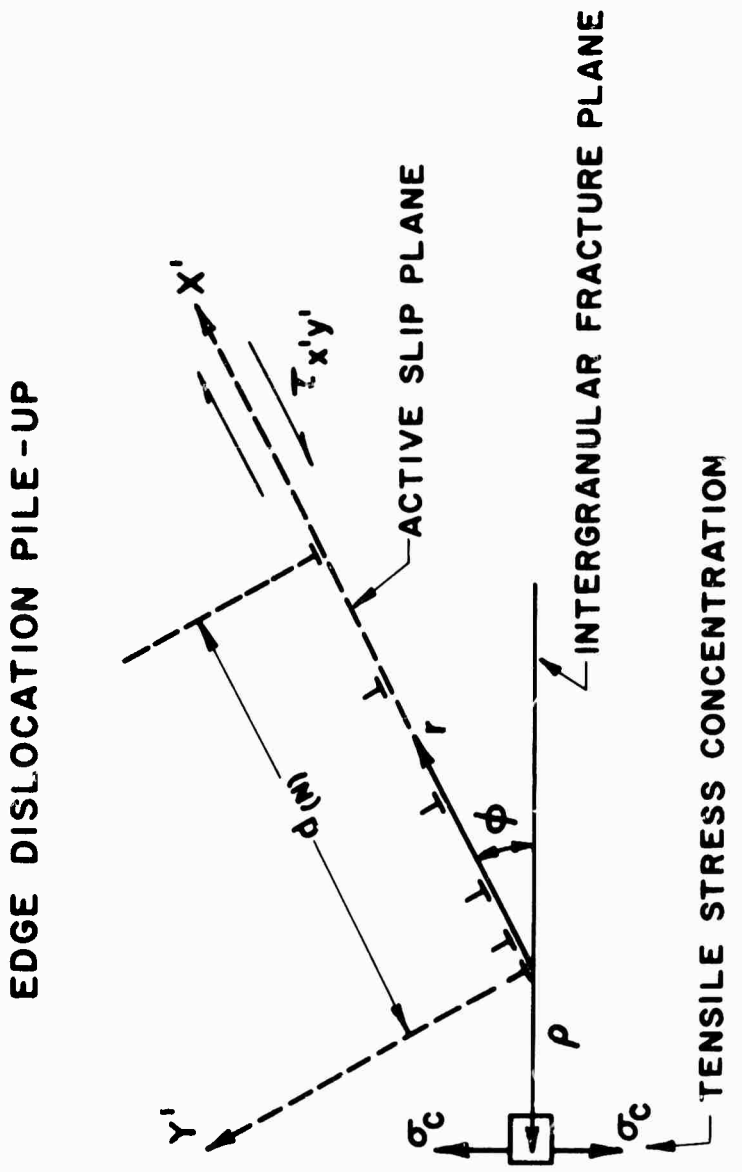


Figure 43. Stroh's model showing the normal tensile stress concentration ahead of a blocked slip band.

stress distribution at a crack tip, and a more adaptable dependence of $\tau_{x'y'}$, on ϕ and r will be used where ϕ is the angle from the crack plane to the active slip plane and r is the radial distance from the crack tip to any point on the slip plane. As previously mentioned, Williams⁽⁹⁾ in Figure (7) developed the elastic stress distribution at the base of a stationary crack. If the first term of William's series solution for $\sigma_{r,\phi}$ is used then:

$$\tau_{x'y'} = \frac{K}{4(2\pi r)^{1/2}} \left[\sin \frac{\phi}{2} + \sin 3 \frac{\phi}{2} \right] \quad (\text{VII.4})$$

K = stress intensity factor

r = radial distance from crack tip

Higher order terms in the solution for $\tau_{x'y'}$, are neglected, and this approximation discounts the stress singularities, i.e. $\tau_{x'y'} \rightarrow \infty$ as $r \rightarrow 0$. Equation (VII.4) shows $\tau_{x'y'}$ to be proportional to $1/r^{1/2}$, and this shear stress gradient is incompatible with the previous assumption of dislocation pile-ups based on a constant shear stress on the slip plane. To take this point into account, an average shear stress $\bar{\tau}_{x'y'}$, resulting from this gradient can be computed and used as an approximate shear stress causing dislocation pile-ups

$$\bar{\tau}_{x'y'} = 1/R_C \int_0^{R_C} \tau_{x'y'}(r, \phi) dr \quad \phi = \text{constant.} \quad (\text{VII.5})$$

The length of the shear stress gradient, R_C , over which $\bar{\tau}_{x'y'}$, is computed can be limited to the grain size of the microstructure tested. Considering grain boundaries as an active source of dislocation; $\bar{\tau}_{x'y'}$, can be visualized as

generating dislocations at a grain boundary and then moving these dislocations on a slip plane to the opposite boundary to cause a pile-up. Since σ_c is dependent on φ or the angle of intersection of a discrete slip plane with the grain boundary, it was decided to maximize σ_c with respect to φ and set an upper limit on the effectiveness of blocked inhomogeneous slip in causing crack nucleation.

Substituting Eqs. (VII.3) and (VII.5) into Eq. (VII.2) and maximizing σ_c with respect to φ , we find σ_c is maximum at $\varphi \approx 67^\circ$ and equal to

$$\sigma_c \approx 3/4 \left[\frac{\mu \cdot b}{\pi(1-\nu)\rho R_c^{1/2}} \right]^{1/2} \times N^{1/2} \times K^{1/2}. \quad (\text{VII.6})$$

It will be noted that σ_c is dependent on N , the number of dislocations piled-up in the slip plane. Since it takes a finite period of time for these dislocations to pile-up, σ_c is dependent on time. This time dependence of σ_c involves a description of dislocation motion, or velocity, on slip systems in the matrix. The time dependent part of the normal stress at the crack σ_{yy} (time dependent) i.e., Eq. (VII.1), can now be equated to $\sigma_c (\varphi = 67^\circ)$. Likewise if the first term of the William's series solution, Figure (7) part B, for $\sigma_{\varphi\varphi}$ is used for σ_{yy} (instantaneous) at $\varphi = 0$ then the fracture criterion becomes:

$$\sigma_{\text{fracture}} = \frac{K}{(2\pi\rho)^{1/2}} + 3/4 \left[\frac{\mu \cdot b}{\pi(1-\nu)\rho R_c^{1/2}} \right]^{1/2} \times N^{1/2} \times K^{1/2}, \quad (\text{VII.7})$$

σ_{yy} (instantaneous) is a function of the applied stress and crack geometry and reaches its value at the moment of loading, or at zero time. However,

σ_c ($\phi \approx 67^\circ$) is time dependent through the number, N , of blocked dislocations forming on the slip plane. Thus, the fracture criteria is expressed only as a function of the stress intensity factor and the number of dislocations in a pile-up.

C. Time Dependence of Dislocation Pile-Ups:

The previous section has formulated a static criteria of fracture in terms of the stress intensity factor and the number of dislocations in a pile-up. Logically, the next step is to describe the time dependence of the number of dislocations in a pile-up, and thus, the time involved to initiate fracture for a given stress intensity factor. When discussing the time for different lengths of dislocation pile-ups to occur, we are dealing with the dependence of dislocation motion on the applied stress on the system. Without sufficient data on a particular system, an assumption must be made describing the relation between dislocation velocity and the applied shear stress on an active slip plane. For the purposes of this analysis, the form of the stress-velocity relation will be assumed as:

$$v = v_o \left(\frac{\tau_{\text{effective}}}{\tau_o} \right)^m \quad (\text{VII.8})$$

v = dislocation velocity

v_o = 1 cm/sec.

$\tau_{\text{effective}}$ = the applied stress minus back stresses leading to an effective shear stress on a slip system.

m = constant characteristic of the material

τ_o = shear stress needed to move a dislocation at 1 cm/sec.

If we further assume that a slip system is initially free of dislocations, and subsequently, a pile-up forms by the generation of dislocations at a grain boundary which move down the slip plane one at a time; then the problem can be formulated mathematically. A complete development of this problem is shown in Appendix II-A with the following result.

$$t_{(N)} = \frac{\tau_o^m N}{V_o} \sum_{i=1}^N \frac{[R_c - d_{(i-1)}]}{[\tau_{\text{applied}} - \tau_{\text{back stress}}]}^m \quad (\text{VII.9})$$

$$\text{where } d_{(i-1)} = \frac{(i-1) \mu \times b}{\pi(1-r)\tau_{\text{applied}}}.$$

The quantity $t_{(N)}$ in Eq. (VII.9) is the time required to build up an array of N dislocations under a shear stress, τ_{applied} , and over a fixed microstructural grain size R_c . The calculation of $\tau_{\text{(back stress)}}$ due to $(i-1)$ dislocations in the pile-up on the i^{th} dislocation is discussed in Appendix II-A.

D. Crack Propagation:

The conditions specified in Eqs. (VII.7) and (VII.9) defines both a criterion for fracture and a means for calculating the time to cause crack nucleation. However, the analysis makes no mention of the propagation stage, or the distance of crack advance once the fracture criterion is reached. The choice of an appropriate criterion to describe the propagation stage of fracture comes from analyzing the extent of the stress field of blocked inhomogeneous plastic flow. The stress concentration of blocked slip bands at a grain boundary is localized over the extent of the impingement of plastic flow. The tensile stress

concentration σ_c (See Eq. (VII.2)) across the grain boundary decreases as one over the square root of the distance from the crack tip. Thus, the stress concentration is large in the near vicinity of the blocked slip band but decreases rapidly as the distance from the band increases. However, the decreasing stress field of the blocked slip band encounters the static stress field of the advancing crack tip, which also decreases as one over the square root of the distance from the crack tip, i.e. first term of Eq. (VII.7) for σ_{fracture} . Thus, the static stress field at the crack tip is enhanced by the neighboring slip band impingement.

Figure (44) depicts the superposition of the static stress field of the crack and the increasing stress field of a blocked slip band. This figure shows that

$\sigma_{yy}^{\text{total}} = \sigma_{\text{fracture}}$ (Eq. (VII.1)) at $\rho = s/2$ and for a time, $t_{(N)}$, where:

$\rho = s/2$ is one half the slip band spacing or one half the distance between the advancing crack front and the blocked slip band.

$t_{(N)}$ is the time required to build up a critical number of dislocations, N , such that Eq. (VII.7) is satisfied for $\rho = s/2$.

This model describes the propagation stage by restricting crack extension to the distance between coarse slip bands in a microstructure which exhibits inhomogeneous plastic flow. Once the fracture criterion is reached at $\rho = s/2$, the crack is assumed to extend to the next coarse slip band and await crack initiation again. The process is repetitive, and a summation of crack initiation times and crack propagation increments leads to macroscopic crack extension as a function of time. With this assumption, Eq. (VII.9) defines a time, t , for crack initiation and propagation over a distance, S , between coarse slip bands.

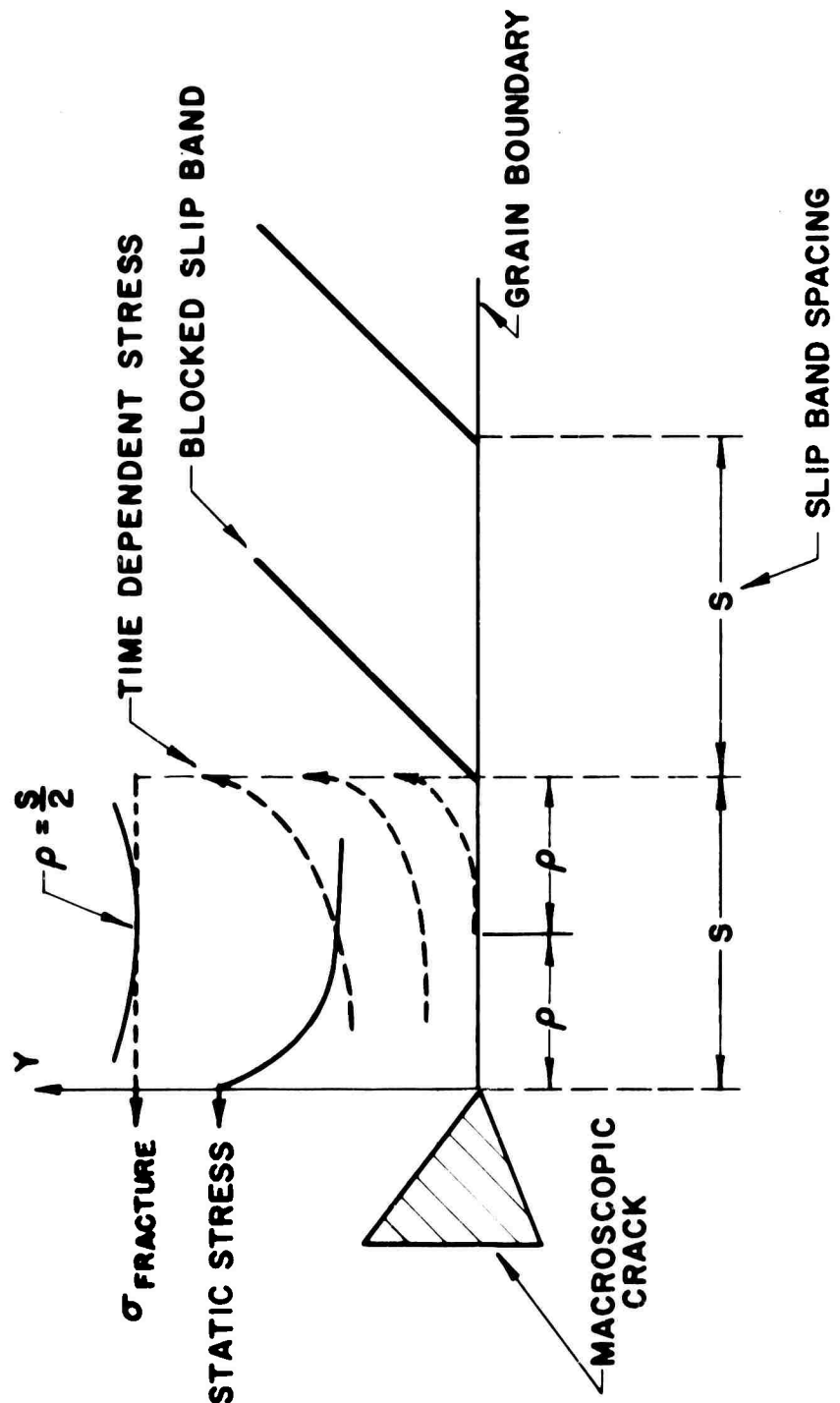


Figure 44. Superposition of a static stress state, i.e. at the crack tip, and a time dependent stress state, i.e. at the blocked slip band, over a distance S .

Consequently, the crack velocity for any increment is:

$$v_c = S/t_{(N)} . \quad (VII.10)$$

In summary, the geometric dependence of the elastic stress state or the stress intensity factor, K , on crack length can be determined if the loading condition and geometry is known. By combining the functional dependence of K on crack length L in Eq. (VII.7), the fracture criterion is expressed in terms of the required number of dislocations, N , at any crack length necessary to cause a further crack extension S . Also, the time required for these N dislocations to build up under an elastic stress state determined by K is calculated from Eq. (VII.9).

E. Theoretical Simulation of Intergranular Fracture In Air:

The hypothesis developed for intergranular crack initiation and propagation in air offers a quantitative description of cracking kinetics under varying elastic stress states. The plausibility of this hypothesis was tested by assuming material constants in Eqs. (VII.7), (VII.8), and (VII.10) appropriate to the Al-15 wt % Zn system. These constants are tabulated and referenced in Appendix II-B. Equations (VII.7) and (VII.9) were then used in a computer program, listed in Appendix II-B, to calculate fracture times associated with a given stress intensity factor for the DCB geometry of No. 3 polycrystal i.e. shown in Table (4) of Appendix I-A. Crack velocity was calculated from Eq. (VII.9) and plotted against stress intensity factor K in Figure (45) along with the

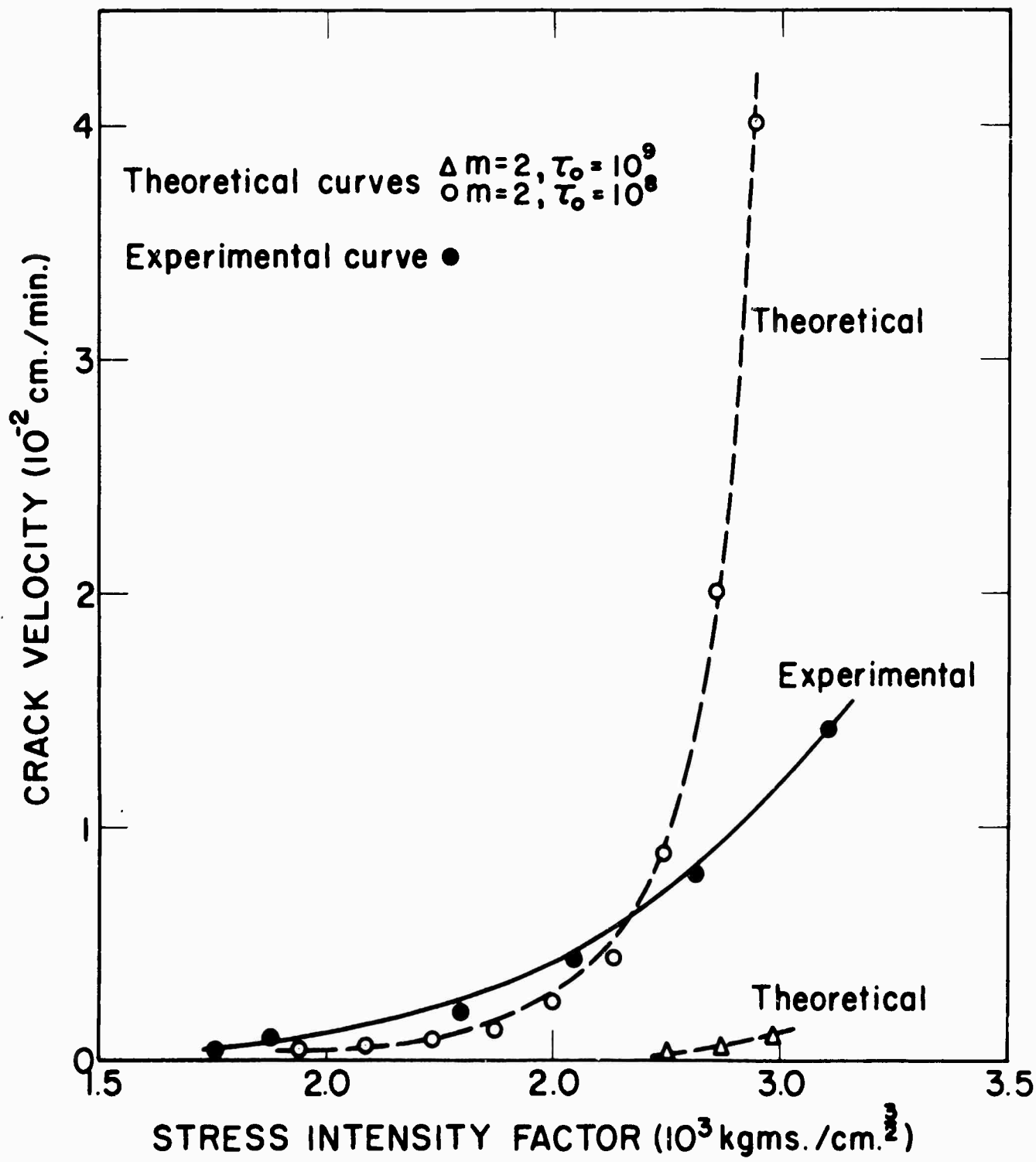


Figure 45. Crack velocity for intergranular fracture in air versus stress intensity factor; for No. 3 polycrystal and for assumed values S, τ_0, V_0 , and m .

experimental values from No. 3 polycrystal. An exact determination of the theoretical curve in Figure (45) depends upon the choice of parameters i.e., coarse slip band spacing, S , in Eq. (VII.10) and dislocation mobility constants τ_o , V_o , and m in Eq. (VII.8).

The coarse slip band spacing for a particular microstructure can be determined by measuring the distance between straight slip traces on a surface after some degree of deformation. Slip traces corresponding to the experimental curve and microstructure in Figure (45) are shown in Figures (34) and (36). These figures show that the microstructure corresponding to No. 3 polycrystal i.e., designated No. I and discussed in section VI.a, has a coarse slip band spacing, S , of approximately 1μ . In addition to knowing S for a particular microstructure, a determination of parameters, τ_o and m , which describe dislocation velocity in the matrix is required to completely define the process. Experimental studies relating dislocation velocity in the matrix to an applied shear stress have not been performed on the different microstructures in the Al-15 wt % Zn system. Thus, it becomes necessary to make an educated guess as to the appropriate values of τ_o and m for the microstructure of interest. The critical resolved shear stress, C.R.S.S., for the microstructure of No. 3 polycrystal was used to set an upper limit on the parameter τ_o . A C.R.S.S. for a similar microstructure has been reported by Price and Kelly⁽²⁸⁾ as 8.43 kgms/mm^2 . This value was used to set the upper limit on stress, $\tau_o = 10^9$ dynes/cm², necessary to cause a dislocation velocity of $V_o = 1 \text{ cm/sec}$. The

C.R.S.S. for a particular slip system is the stress where macroscopic deformation takes place, and it is plausible to assume this stress is capable of moving dislocations at velocities of at least 1 cm/sec. A lower limit to the shear stress necessary to cause this same dislocation velocity was arbitrarily assumed to be τ_o , the parameter m , which describes the sensitivity of dislocation velocity to shear stress was selected equal to 2. A value of $m = 2$ in Eq. (VII.9) represents the smallest value found in dislocation velocity studies in a variety of other systems i.e.; Si, Lif, Fe-Si, W, Cu, and Cu-Ni⁽¹⁰²⁾. If the microstructure tested in the Al-Zn system exhibits similar characteristics to dislocation velocity as the fcc Cu and Cu-Ni structures, the parameter m may well be bounded as, $2 \leq m \leq 10^{(102)}$. Based on these studies, a selection of $m = 2$ forces a minimum dependence, or sensitivity, of dislocation velocity on shear stress in the experimental microstructure. The microstructure of interest, No. I, contains a large volume fraction of G.P. zones in the matrix and a choice of $m = 2$ implies that the zones suppress a strong dependence ($m > 2$) of dislocation velocity on shear stress.

A comparison of the theoretical and experimental curves in Figure (45) shows that they coincide to a large extent when the following parameters are used:

$$S = 1\mu, m = 2, \tau_o = 10^8 \text{ dynes/cm}^2 \text{ and } m = 2.$$

This implies that the experimental microstructure, No. I, has a coarse slip band spacing of 1μ and affects the dislocation velocity V in the matrix as; $V = (\tau/10^8)^2$.

Thus, the theoretical analysis predicts the observed dependence of crack velocity on stress intensity factor for intergranular fracture in air of this microstructure.

F. Application of Formalism to Intergranular Fracture In A Corrosive Environment:

The theoretical analysis can be adapted to explain intergranular fracture in the presence of a corrosive environment if the following a priori assumption is made: "The addition of a corrosive environment sets up a localized attack but does not affect slip properties in the matrix". Localized attack may be either the local anodic dissolution of a precipitate or grain boundary in the matrix or the adsorption of select species at an intergranular crack tip. A general review of phenomena involving electrochemical attack and surface adsorption has been written in section I.

The microstructures tested in the Al-15 wt % Zn system exhibit a localized attack at grain boundary zinc precipitates as exemplified by Figure 36. If this localized galvanic attack occurs at the intergranular crack tip during fracture, it would be plausible to assume that $\sigma_{(\text{fracture})}$ in Eq. (VII.7) becomes a function of time. This would imply that the inherent fracture strength of the grain boundary is being locally decreased by the anodic dissolution of zinc precipitate on the boundary. If the kinetics of this electrochemical reaction were known, it might be possible to express the fracture stress of the boundary as a function of time, t . This could be accomplished by a series expansion with the coefficients of the expansion dependent on the rate of the corrosion reaction i.e.,

$$\sigma_{(\text{fracture})}(t) = \sigma_F(0) + \left(\frac{\delta \sigma_F}{\delta t} \right)_{t=0} t + \dots \quad (\text{VII.11})$$

Equation (VII.11) would then replace the static fracture stress of the grain boundary, $\sigma_F(0)$, in Eq. (VII.7) by a time dependent function. If $\sigma_{(\text{fracture})}(t)$ decreases as the corrosion reaction proceeds, then a lower number of piled-up dislocations, N , would be required to cause crack initiation when compared to a pile-up formed under a constant $\sigma_{(\text{fracture})}(0)$. Thus, the time required to form N dislocations would be decreased and the fracture process accelerated. The acceleration in fracture kinetics is experimentally observed when comparing crack velocity versus stress intensity factor for a constant microstructure tested in different environments, refer to Figure (18). The extent of the shift in cracking kinetics for the test environments air, distilled H_2O , and 0.5M NaCl in Figure (18) cannot be deduced because of a lack of experimental data in determining Eq. (VII.11).

G. Summary:

The results of this research on intergranular fracture processes in an Al-15 wt % Zn alloy will be summarized under four categories: (i) Stress State and Intergranular Cracking Kinetics, (ii) Microstructural Affects on Intergranular Fracture, (iv) The Effects of Grain Boundary Orientation on Intergranular Fracture, and (v) Theoretical Formalism For Intergranular Fracture. The hypothesis is based on the qualitative results listed in categories (i), (ii), (iii), and (iv) and formulates a quantitative description of environment-sensitive intergranular fracture.

(i) Stress State and Intergranular Cracking Kinetics

- A) A plane strain stress state exists for the polycrystalline double-cantilever beam test geometry.
- B) Slow crack growth in air under a decreasing stress intensity factor.
- C) An acceleration in the crack velocity under a fixed stress intensity factor for a change in the test environment from air to distilled H_2O to 0.5M NaCl.
- D) The crack velocity V is proportional to the square of the stress intensity factor K ; i.e., $V = A + B \times K^2$ where A and B are constants depending on the test environment and microstructure.

(ii) Microstructural Affects on Intergranular Fracture

- A) Surface slip traces change from a straight, planar appearance to a wavy, dispersed type as the volume fraction of G.P. zones in the matrix decreases.
- B) Intergranular crack propagation in air and 0.5M NaCl decreases as the volume fraction of G.P. zones in the matrix decreases.
- C) The threshold toughness $K(V \rightarrow 0)$ increases with a decreasing yield strength and volume fraction of G.P. zones.
- D) Susceptibility to stress corrosion cracking in 0.5M NaCl decreases as the volume fraction of G.P. zones decreases.
- E) Matrix precipitates, i.e. G.P. zones, and not grain boundary precipitates appear to control susceptibility to intergranular fracture in 0.5M NaCl.

(iii) Galvanic Attack

Localized anodic attack, i.e. pitting corrosion in 0.5M NaCl, in the absence of stress is noted at the second phase zinc precipitate.

(iv) The Effects of Grain Boundary Orientation on Intergranular Fracture

The greater the number of coincident slip systems, i.e. parallel {111} planes and <110> directions, across a bi-crystal grain boundary the less the susceptibility to intergranular fracture in 0.5M NaCl.

(v) Theoretical Formalism for Intergranular Fracture in Air and in a Corrosive Environment

- A) Predicts the observed dependence of crack velocity on stress intensity factor.
- B) The theory takes into account the alloy system and microstructure on the intergranular fracture processes by considering deformation characteristics, i.e. homogeneous or inhomogeneous plastic flow, and the dependence of dislocation velocity on the applied shear stress.
- C) The formalism predicts an increase in the crack velocity under a fixed stress intensity factor when changing the test environment from air, i.e. inert atmosphere, to a corrosive medium.

General Bibliography

1. A. A. Griffith, *Philosophical Transactions*, vol. 221, (1921), p.163.
2. C. E. Inglis, *Transactions of Inst. of Naval Architects*, vol. 60, (1913) p.219.
3. G. R. Irwin and J. A. Kies, *Welding Res. suppl.*, 33 (4) 1935-98 (1954).
4. J. J. Gilman, *J. Appl. Phys.*, 31 (12) 2208-18 (1960).
5. A. R. Westwood and T. T. Hitch, *J. Appl. Phys.*, 34 (10) 3085-89 (1964).
6. P. P. Gillis and J. J. Gilman, *J. Appl. Phys.*, 35 (3) 647-58 (1964).
7. S. M Wiederhorn and A. M. Shorb, "Critical Analysis of the Double Cantilever Method of Measuring Fracture Surface Energies", to be published.
8. J. E. Srawley and B. Gross, *Mater. Res. Std.*, 7 (4) 155-62 (1967).
9. M. L. Williams, *Journal Applied Mechanics, Trans. ASME*, No. 56-A.16, (1957).
10. G. R. Irwin, *Encyclopedia of Physics*, vol. VI, Springer, Heidelberg (1958).
11. P. C. Paris and G. C. Sih, *Fracture Toughness Testing*, ASTM, Philadelphia, STP No. 381 (1965), p.30.
12. A. A. Griffith, *Proc. Int. Congr. Appl. Mech.*, 55, (1924).
13. C. N. Freed and J. M. Krafft, *Journal of Materials*, vol. 1, No. 4, (1966) p.770.
14. R. Chadwick, N. B. Muir, and H. B. Grainger, *Journal of the Institute of Metals*, 85, p.161 (1956).
15. U. F. Kochs, *Phil. Mag.*, 10, 187 (1964)
16. A. A. Johnson, E. K. Hughes and P. W. Barton, *Journal of the Institute of Metals*, 94, No. 5, p.186 (1966).
17. A. Kelly and R. B. Nicholson, *Prog. Mat. Sci.*, 10, 3, (1963).
18. S. Timoshenko, *Theory of Elasticity*, (McGraw-Hill Book Co., Inc., New York, (1934) p.33.

19. S. Mostovoy, P. Crosley, and E. Ripling, *Journal of Materials*, vol. 2, No. 3, (1967) p.661.
20. G. R. Irwin and J. A. Kies, *Metal Progress*, 78, No. 2, 73 (1960).
21. R. J. Charles, *Progress in Ceramic Science*, 1961, vol. 1, p.1.
22. W. B. Hillig, *Modern Aspects of the Vitreous State*, vol. 2, Butterworths, London, 1962.
23. A. S. Tetelman and A. J. McEvily, *Fracture of Structural Materials*, p.459, John Wiley & Sons, New York, (1967).
24. T. C. Baker and F. W. Preston, *J. Applied Phys.*, 1946, vol. 17, p.170.
25. D. McLean, *J. Inst. Metals (London)*, 85, 468, (1957).
26. D. Tromans and J. Nutting, *Fracture of Solids*, Interscience, New York (1962) p.637.
27. J. W. Christian, *The Theory of Transformations in Metals and Alloys*, Pergamon Press, New York (1965), p.307.
28. R. J. Price and A. Kelly, *Acta Met.*, 1964, 12, p.159.
29. M. Murakami and O. Kawano, *Acta Met.*, 1969, 17, p.29.
30. A. Johnson, E. Hughes, and P. Barton, *J. Inst. Metals*, 94, 186, (1966).
31. G. J. Carpenter and R. Garwood, *J. Inst. Metals*, 94, 301, (1966).
32. J. Dash and M. Fine, *Acta Met.*, 1961, 9, p.149.
33. D. A. Shockley and G. W. Groves, *Journal of the American Ceramic Society*, 51, No. 6, 299, (1968).
34. C. Herring, *Structure and Properties of Solid Surfaces*, edit. R. Gomer and C. Smith (Univ. of Chicago, 1955), 5.
35. G. Henry, J. Plateau, and C. Crussard, *Mech. Sci. Rev. Metall.*, 56, (1959) 417.
36. A. H. Cottrell: *Trans. Met. Soc. AIME*, 1958, vol. 212, p.192.
37. N. J. Petch, *Phil. Mag.*, 1958, vol. 3, p.1089.

38. G. W. Groves and A. Kelly: Phil. Mag., 1963, vol. 8, p.877.
39. T. L. Johnston, R. G. Davies, and N. S. Stoloff, Phil. Mag., 1965, vol. 12, p.305.
40. A. C. Westwood and N. S. Stoloff, Environment Sensitive Mechanical Behavior, AIME Conference, vol. 35, (1965), p.613.
41. A. M. Turkalc and J. R. Low, General Electric Research Report No. 64-RL-3614M, Schenectady, New York (1964).
42. W. G. Johnston and J. J. Gilman, J. Appl. Phys., 31, 632 (1960).
43. R. B. Mears, R. H. Brown, and E. H. Dix: Symposium on Stress Corrosion Cracking of Metals, p.323, ASTM-AIME, Philadelphia, (1944).
44. E. H. Dix: Trans. Met. Soc. AIME, 1940, vol. 137, p.11.
45. W. Helfrich, Symposium on Stress Corrosion Cracking of Metals, ASTM, New Jersey, (1965).
46. G. Thomas and J. Nutting, J. Inst. Metals, 86, p.7 (1957-58).
47. G. Greetham and R. Honeycombe, J. Inst. Metals, 89, 13, (1960).
48. J. Friedel, Les Dislocations, Pergamon Press, Oxford, (1956).
49. D. Corderoy and R. Honeycombe, J. Inst. Metals, 93, 432, (1965).
50. J. S. Koehler, Phys. Rev. 86, 52, (1952).
51. P. J. Guest, M. S. Thesis, AEC Contract No. W-7405, Univ. Cal., (1967).
52. E. N. Pugh: Ph.D. Thesis, Univ. of Wales, 1959.
53. G. Meikle, J. Inst. Metals, 1956-57, vol. 85, p.540.
54. A. J. DeArdo: Ph.D. Thesis, Carnegie-Mellon University, (1969).
55. G. J. Ogilvie, J. Inst. Metals, 81, 491 (1952).
56. K. G. Davis, E. Teghtsoonian, and A Lu, Acta Met., 14, 1677 (1966).
57. N. Kratochvilova and B. Sestak, Phys. Status Solidi, 5, 343, (1964).

58. T. J. Koppenaal, *Acta Met.*, 10, 684 (1962).
59. M. P. Usikov, *Physics Metals Metallog.*, 11, 127 (1961).
60. A. N. Stroh, *Proc. R. Soc.*, 223, A, 404 (1954).
61. J. D. Eshelby, F. Frank, and F. Nabarro, *Phil. Mag.*, 42, 351 (1951).
62. T. L. Johnston, R. Stokes, and C. Li, *Phil. Mag.*, 6, 23 (1961).
63. R. C. Ku and T. L. Johnston, *Phil. Mag.*, 9, 231 (1964).
64. F. C. Roesler, *Proc. Phys. Soc.*, B-69, 981 (1956).
65. F. Clarke and R. J. Sambell, *Phil. Mag.*, 5, 697, (1960).
66. E. Andrade and L. Tsien, *Proc. Roy. Soc. (London)*, A159, 346 (1937).
67. C. Zener, *Fracturing in Metals*, ASM, Cleveland, (1948), p.3.
68. R. J. Stokes, T. L. Johnston, and C. Li, *Phil. Mag.*, 4, 920 (1959).
69. R. L. Bell and R. W. Cahn, *J. Inst. Metals*, 86, 433 (1957-58).
70. J. J. Gilman, *Trans. AIME*, 200, 621 (1954).
71. A. Westwood, *Phil. Mag.*, 5, 981, (1960).
72. D. Hull, *Acta Met.*, 8, 11 (1960).
73. R. Honda, *J. Phys. Soc. Japan*, 16, 1309 (1961).
74. A. S. Tetelman, *Proc. AIME Intern. Conf. on Fracture*, Seattle, Wash. (1962).
75. E. Hornbogen, *Trans. AIME*, 221, 711 (1961).
76. R. Carnahan, T. Johnston, R. Stokes, and C. Li, *Trans. AIME*, 221, 45 (1961).
77. A. N. Stroh, *Adv. Phys.*, 6, 418 (1957).
78. E. Smith, *Acta Met.*, 16, 313 (1968).
79. G. T. Hahn and C. Reid, *J. Iron Steel Inst.*, 202, 677 (1964).

80. A. Rosenfield and G. Hahn, *Acta Met.*, 16, 755 (1968).
81. W. Rostoker, J. McCaughey, and H. Markus, *Embrittlement by Liquid Metals*, Reinhold, New York (1960).
82. M. Kamdar and A. Westwood, *Environment Sensitive Mechanical Behavior*, p.581, Gordon and Breach, New York (1966).
83. A. Westwood and M. Kamdar, *Phil. Mag.*, 8, 787 (1963).
84. E. D. Hondros, *Phil. Mag.*, 148 (1968).
85. A. Westwood and E. Pugh, *Mat. Sci. Res.*, 3, 553 (1965).
86. F. Booth and H. Godard, *First Intern. Conf. on Metallic Corrosion*, London (1961), p.703.
87. N. A. Nielsen, *Second Intern. Conf. on Metallic Corrosion*, Texas (1965) p.116.
88. C. Edeleanu, *J. Inst. Metals*, 89, 90 (1960-61).
89. P. Swann and J. Embury, *Intern. Maters. Conf. on High Strength Maters.*, p.327, (1964) John Wiley.
90. E. Uhlig, *Phy. Metallurgy of Stress Corrosion Fracture*, p.1, (1959), Interscience, New York.
91. A Jacobs, *Trans. AIME*, 58, No. 4, p.579 (1965).
92. M. Speidel, *Proceedings of Conference on Stress Corrosion Cracking*, Houston, Texas (1969) p.561.
93. W. Gruhl, *Aluminum*, 38, 775 (1962).
94. D. Tromans and J. Nutting, *Corrosion*, 21, No. 5, p.143 (1965).
95. A Forty and P. Humble, *Second Intern. Conf. on Metallic Corrosion*, Texas, (1963), p.80.
96. R. N. Parkins, *Met. Rev.*, 9, 201 (1964).
97. G. Irwin, J. Kies, and H. Smith, *Proc. ASTM*, 58, 640 (1958).
98. A. H. Cottrell, *Progr. Metal Phys.*, 1, 77 (1949).

99. N. Mott, Proc. Roy. Soc., A220, 1 (1953).
100. J. Hirth and J. Lothe, Theory of Dislocations, p.705, McGraw-Hill Book Co., Inc., New York (1968).
101. D. H. Thompson and A. Tracy, Inst. Metals, AIME, 185, (1949) p.100.
102. A Rosenfield, G. Hahn, A. Bement, and R. Jaffe, Dislocation Dynamics, McGraw-Hill Book Co., Inc., New York, (1967) p.557.
103. T. Baumeister, Mark's Mechanical Engineers' Handbook, 6th Ed. 1964, McGraw Hill Book Co. Inc., New York, p.5-6.
104. Fracture Toughness Testing and its Applications, ASTM No. 381, Chicago, Illinois, (1964), p.138.
105. P. G. Shewmon, Diffusion In Solids, McGraw-Hill Book Co., Inc., New York (1963) p.19.

Appendix I-A
Table No. 1

Specimen No. 1 Polycrystal

Microstructure Tested: 15 min. age at 155°C and 100 hrs at room temperature.

Test Conditions: Fracture in air.

"DCB" Geometry: Deflection δ 9.75×10^{-2} cm. Height H 1.2690 cm.

Length L 8.325 cm. Width B 0.4165 cm. Width W 1.270 cm.

Force F (lbs.)	Crack Length L (cm.)	Time t (min.)
448.5	3.497	0.0
430.5	3.586	1.2
409.2	3.698	3.8
393.6	3.718	7.0
388.5	3.761	9.1
383.5	3.834	11.4
376.5	3.834	14.4
359.0	4.029	21.4
348.0	4.029	23.8
335.5	4.029	28.0
318.5	4.083	39.0
314.8	4.083	47.0
309.5	4.160	58.0
305.3	4.206	64.2
296.7	4.296	69.0
291.5	4.296	77.0
289.0	4.370	83.4
286.0	4.370	92.0
282.5	4.370	102.0
277.0	4.462	110.0
269.5	4.503	115.0
265.0	4.550	124.0
263.0	4.572	131.4
260.0	4.572	141.0
248.5	4.572	151.0
243.5	4.594	162.0
238.8	4.648	174.0
235.5	4.691	198.0
234.6	4.691	202.0
211.7	4.978	348.0
199.5	5.265	547.0
196.6	5.265	577.0
177.3	5.333	1107.0
174.9	5.333	1177.0
168.2	5.372	1319.0

Appendix I-A

Table No. 2

Specimen No. 1 Polycrystal

Microstructure Tested: 15 min age at 155°C and 100 hrs at room temperature.

Test Conditions: Fracture in air.

"DCB" Geometry: Deflection 313.51×10^{-2} cm. Height $H1.2690$ cm.Length $L 8.325$ cm. Width $B 0.4165$ cm. Width $W1.270$ cm.

Force F (lbs.)	Crack Length L (cm.)	Time t (min.)
224.5	5.452	0.0
219.5	5.545	7.6
217.2	5.545	12.6
214.0	5.589	22.6
211.3	5.623	35.6
207.5	5.650	66.6
204.0	5.706	86.6
200.5	5.739	99.6
195.0	5.746	128.6
191.0	5.798	147.6
185.2	5.880	200.0
170.5	5.973	457.0
152.3	6.274	1239.0
140.2	6.533	1554.0
136.7	6.533	1664.0
111.0	6.958	2664.0

Appendix I-A

Table No. 3

Specimen No. 2 Polycrystal

Microstructure Tested: 50 min age at 155°C and 100 hrs at room temperature.

Test Conditions: Fracture in air.

"DCB" Geometry: Deflection 8.38×10^{-2} cm. Height $H 1.2690$ cm.

Crack Length $L 5.775$ cm. Width $B 0.660$ cm. Width $W 1.270$ cm.

Force F (lbs.)	Crack Length L (cm.)	Time t (min.)
531.0	3.217	0.0
503.5	3.269	10.2
489.5	3.331	20.0
476.5	3.369	34.0
466.5	3.407	50.0
456.0	3.499	66.0
443.5	3.558	80.5
413.5	3.619	126.0
404.0	3.645	151.0
394.0	3.669	189.0
386.0	3.699	222.5
351.0	3.908	404.5
317.5	4.014	619.5
251.1	4.207	1177.5
* 211.3	4.207	1484.5

* Not valid, crack propagation out of side grooves.

Appendix I-A
Table No. 4

Specimen No. 3 Polycrystal

Microstructure Tested: 50 min age at 155°C and 100 hrs at room temperature.

Test Conditions: Fracture in air.

"DCB" Geometry: Deflection 6.10×10^{-2} cm. Height $H 1.2690$ cm.

Crack Length $L 8.330$ cm. Width $B 0.4130$ cm. Width $W 1.270$ cm.

Force F (lbs.)	Crack Length L (cm.)	Time t (min.)
391.7	3.149	0.0
354.0	3.261	38.0
342.3	3.368	50.0
329.5	3.412	61.2
316.5	3.495	89.4
305.0	3.558	118.0
295.0	3.601	146.8
287.0	3.643	170.0
280.5	3.681	183.0
268.0	3.885	222.0
262.5	3.903	250.0
252.1	3.954	294.0
247.2	3.970	314.0
241.5	3.978	346.0
234.5	4.002	390.0
221.5	4.015	455.0
219.5	4.075	478.0
196.5	4.257	724.0
188.5	4.336	833.0
163.8	4.720	1432.0
162.7	4.720	1457.0

Appendix I-A
Table No. 5

Specimen No. 3 Polycrystal

Microstructure Tested: 50 min age at 155°C and 100 hrs at room temperature.

Test Conditions: Fracture in air.

"DCB" Geometry: Deflection δ 12.90×10^{-2} cm. Height H 1.2690 cm.

Length L 8.330 cm. Width B 0.4130 cm. Width W 1.270 cm.

Force F (lbs.)	Crack Length L (cm.)	Time t (min.)
324.7	4.814	0.0
308.3	4.945	6.0
281.5	5.034	24.6
263.5	5.087	39.0
251.3	5.208	45.6
238.5	5.306	53.8
223.7	5.306	70.6
218.0	5.406	92.6
207.0	5.457	112.6
194.3	5.538	178.6
186.5	5.659	222.6
184.0	5.707	245.6
184.0	5.751	252.6
160.0	5.854	388.6
128.0	6.183	703.6

Appendix I-A

Table No. 6

Specimen No. 4 Polycrystal

Microstructure Tested: 50 min age at 155°C and 100 hrs at room temperature.

Test Conditions: Fracture in 0.5M NaCl

"DCB" Geometry: Deflection δ 6.99×10^{-2} cm. Height H 1.2690 cm.

Length L 5.898 cm. Width B 0.4310 cm. Width W 1.270 cm.

Force F (lbs.)	Crack Length L (cm.)	Time t (min.)
170.0	4.125	0.0
158.4	4.210	2.7
153.8	4.279	4.3
147.6	4.559	7.5
143.8	4.567	11.0
137.4	4.655	16.0
129.2	4.845	23.5
123.4	4.960	30.0
110.4	5.195	39.3
95.5	5.229	47.0
83.8	5.344	54.0
76.4	5.400	59.5
65.8	5.461	68.0
52.8	5.485	78.5
49.0	5.538	80.5
43.2	5.645	92.0
30.4	5.688	110.0
28.8		

Appendix I-A
Table No. 7

Specimen No. 5 Polycrystal

Microstructure Tested: 50 min age at 155°C and 100 hrs at room temperature.

Test Conditions: Fracture in 0.5M NaCl.

"DCB" Geometry: Deflection 6.02×10^{-2} cm. Height H 1.2690 cm.

Length L 5.807 cm. Width B 0.4070 cm. Width W 1.2690 cm.

Force F (lbs.)	Crack Length L (cm.)	Time t (min.)
131.8	3.375	0.0
118.6	3.672	11.7
114.4	3.695	17.2
112.4	3.737	19.1
110.8	3.755	22.2
109.1	3.787	25.6
104.7	3.958	33.2
101.5	4.014	39.4
98.5	4.062	46.2
95.0	4.222	53.7
91.6	4.320	59.6
84.2	4.445	78.9
78.0	4.518	97.1
73.6	4.642	106.3
70.2	4.699	113.6
62.2	4.797	125.2
56.6	4.976	148.9
50.0	5.097	163.5
46.0	5.261	168.7
20.7	5.451	189.5
11.6	5.491	210.6

Appendix I-A

Table No. 8

Specimen No. 6 Polycrystal

Microstructure Tested: 50 min age at 155°C and 100 hrs at room temperature.

Test Conditions: Fracture in 0.5M NaCl.

"DCB" Geometry: Deflection 52.84×10^{-2} cm. Height H 1.270 cm.

Length L 5.807 cm. Width B 0.646 cm. Width W 1.270 cm.

Force F (lbs.)	Crack Length L (cm.)	Time t (min.)
172.3	3.286	0
170.0	3.316	23.5
168.3	3.342	39.0
167.2	3.357	47.5
165.3	3.357	56.0
163.6	3.377	64.3
162.3	3.377	69.8
148.9	3.634	120.6
132.0	3.988	185.4

Appendix I-A

Table No. 9

Specimen No. 6 Polycrystal

Microstructure Tested: 50 min age at 155°C and 100 hrs at room temperature.

Test Conditions: Fracture in 0.5M NaCl.

"DCB" Geometry: Deflection δ 5.56 $\times 10^{-2}$ cm. Height H 1.270 cm.

Length L 5.807 cm. Width B 0.646 cm. Width W 1.270 cm.

Force F (lbs.)	Crack Length L (cm.)	Time t (min.)
241.5	3.995	0.0
220.5	4.225	8.6
209.5	4.307	11.9
193.0	4.452	18.6
187.0	4.560	29.6
173.0	4.560	44.0
161.3	4.733	57.0
137.2	4.804	80.0
123.0	4.980	111.7
116.7	5.041	115.3
104.0	5.205	123.9
91.7	5.291	129.1
65.6	5.330	135.2
61.7	5.355	136.7
58.7	5.421	138.2

Appendix I-A

Table No. 10Specimen No. 7 Polycrystal

Microstructure Tested: 500 min age at 155°C and 100 hrs at room temperature.

Test Conditions: Fracture in 0.5M NaCl.

"DCB" Geometry: Deflection δ 6.70×10^{-2} cm. Height H 1.270 cm.Length L 8.330 cm. Width B 0.4175 cm. Width W 1.270 cm.

Force F (lbs.)	Crack Length L (cm.)	Time t (min.)
304.1	3.256	0.0
301.0	3.350	4.2
300.0	3.461	8.4
296.2	3.525	13.4
287.5	3.525	20.0
278.8	3.612	27.4
275.4	3.612	29.6
270.0	3.709	33.8
267.5	3.709	35.0
263.4	3.780	38.6
260.0	3.809	42.1
256.5	3.809	46.0
253.4	3.843	49.0
246.1	3.914	54.0
238.0	3.914	59.2
230.0	3.914	64.6
220.0	4.103	74.3
213.5	4.103	84.1
210.7	4.247	90.0
208.5	4.247	95.6
206.3	4.293	101.2
203.0	4.339	107.8
201.5	4.339	110.0
189.3	4.460	128.0
186.8	4.460	130.8
183.5	4.460	136.0

Appendix I-A
Table No. 11

Specimen No. 7 Polycrystal

Microstructure Tested: 500 min age at 155°C and 100 hrs at room temperature.

Test Conditions: Fracture in 0.5M NaCl.

"DCB" Geometry: Deflection δ 6.70 $\times 10^{-2}$ cm. Height H 1.270 cm.

Length L 8.330 cm. Width B 0.4175 cm. Width W 1.270 cm.

Force F (lbs.)	Crack Length L (cm.)	Time t (min.)
18.13	4.488	140.2
177.5	4.534	151.2
174.5	4.599	162.8
174.0	4.599	166.0
171.0	4.799	181.0
168.5	4.799	195.0
165.7	4.814	208.8
160.9	4.850	222.0
155.5	4.925	232.0
152.5	4.925	238.4
148.0	4.953	245.0
143.0	4.993	270.0
124.6	5.434	399.4
122.3	5.556	422.0

Appendix I-A
Table No. 12

Specimen No. 7 Polycrystal

Microstructure Tested: 500 min age at 155°C and 100 hrs at room temperature.

Test Conditions: Fracture in 0.5M NaCl.

"DCB" Geometry: Deflection δ 14.55×10^{-2} cm. Height H 1.270 cm.

Length L 8.330 cm. Width B 0.4175 cm. Width W 1.270 cm.

Force F (lbs.)	Crack Length L (cm.)	Time t (min.)
231.0	5.556	0.0
223.6	5.660	4.8
212.0	5.853	11.8
205.5	5.853	17.6
187.5	6.050	33.0
177.5	6.242	46.0
169.0	6.402	61.0
162.5	6.402	68.0
151.5	6.733	79.0
147.0	6.893	83.0
138.0	7.025	90.6
131.5	7.025	97.4
127.5	7.025	102.8
124.5	7.183	107.0
120.5	7.183	114.0
115.5	7.284	126.6
112.0	7.402	140.0
109.0	7.569	144.6
105.0	7.569	149.0
92.5	7.685	161.0

Appendix I-A

Table No. 13Specimen No. 8 Polycrystal

Microstructure Tested: 5000 min age at 155°C and 100 hrs at room temperature.
 Test Conditions: Fracture in 0.5M NaCl.

DCB Geometry:
 Deflection 6.70×10^{-2} cm. Height H 1.2667 cm.

Width B 0.4180 cm. Width H 1.270 cm.

Specimen No. 10 Polycrystal

Microstructure Tested: 50 min age at 155°C and 30 min at room temperature.
 Test Conditions: Fracture in 0.5M NaCl.

DCB Geometry:
 Length L 8.3510 cm.

Deflection 6.70×10^{-2} cm. Height H 1.2667 cm.
 Width B 0.4170 cm. Width H 1.270 cm.

Force F (lbs)	Crack Length L (cm)	Time t (min.)	Force F (lbs)	Crack Length L (cm)	Time t (min.)
360.0	3.435	0.0	164.0	3.511	0.0
348.5	3.466	60.0	160.0	3.511	185.0
345.5	3.466	95.0	159.0	3.511	220.0
343.0	3.466	124.0			
340.8	3.500	152.0			
337.5	3.542	206.0			
336.0	3.542	228.0			
328.0	3.550	250.0			
					No cracking observed.

Appendix I-A

Table No. 14

Specimen No. 9 Polycrystal

Microstructure Tested: 500 min age at 155°C and 100 hrs at room temperature.

Test Conditions: Fracture in air.

"DCB" Geometry: Deflection 69.70 $\times 10^{-2}$ cm. Height H 1.2690 cm.Length L 8.355 cm. Width B 0.4145 cm. Width W 1.270 cm.

Force F (lbs.)	Crack Length L (cm.)	Time t (min.)
443.7	3.550	0.0
426.1	3.550	19.4
422.3	3.550	35.4
413.5	3.550	83.4
408.5	3.578	127.0
362.6	3.830	472.0
358.2	3.974	479.0
270.0	4.257	1147.0
256.0	4.371	1279.0
248.0	4.489	1356.0
245.2	4.543	1391.0
240.3	4.592	1455.0
235.4	4.619	1570.0
223.2	4.775	1962.0
209.6	4.870	2607.0
204.0	4.887	2864.0
202.0	4.887	2999.0
196.3	4.897	3354.0
190.6	4.965	4006.0

Appendix I-A

Table No. 15Specimen No. 9 Polycrystal

Microstructure Tested: 500 min age at 155°C and 100 hrs at room temperature.

Test Conditions: Fracture in air.

"DCB" Geometry: Deflection δ 17.60×10^{-2} cm. Height H 1.2690 cm.Length L 8.355 cm. Width B 0.4145 cm. Width W 1.270 cm.

Force F (lbs.)	Crack Length L (cm.)	Time t (min.)
314.6	5.633	0.0
306.6	5.680	8.4
302.5	5.686	21.4
201.0	5.686	28.4
298.5	5.686	40.4
296.0	5.711	49.4
292.7	5.735	64.4
290.2	5.757	79.4
286.4	5.762	97.4
282.0	5.800	106.4
278.6	5.810	120.4
274.1	5.825	146.4
262.5	5.946	210.4
259.5	5.982	232.4
249.5	6.053	264.4
246.0	6.113	278.4
242.3	6.169	307.0
241.2	6.169	317.0
237.0	6.208	345.0
234.0	6.208	375.0
231.3	6.230	388.0
227.5	6.270	416.0
223.3	6.278	453.0
221.7	6.299	472.0
212.3	5.522	625.0
211.0	6.568	654.0
209.5	6.568	672.0
199.0	6.697	835.0
179.7	6.897	1413.0
179.5	6.897	1437.0
177.8	6.897	1572.0
177.4	6.897	1652.0

Appendix I-A
Table No. 16

Specimen No. 11 Polycrystal

Microstructure Tested: 50 min age at 155°C and 100 hrs at room temperature.

Test Conditions: Fracture in air.

"DCB" Geometry: Deflection δ 10.60×10^{-2} cm. Height H 1.2698 cm.

Length L 8.260 cm. Width B 0.7850 cm. Width W 1.270 cm.

Force F (lbs.)	Crack Length L (cm.)	Time t (min.)
551.5	3.429	0
537.0	3.475	3.4
522.0	3.511	7.6
512.0	3.543	12.0
503.0	3.583	19.2
497.5	3.592	25.0
490.0	3.592	32.6
483.5	3.592	38.4
476.0	3.613	47.0
470.5	3.659	52.6
464.0	3.675	58.0
454.0	3.757	67.4
450.5	3.787	72.8
442.6	3.818	82.0
425.0	3.846	122.0
419.5	3.875	140.0
417.0	3.892	149.0
415.0	3.907	158.0
410.5	3.926	180.0
406.5	3.926	205.0
403.5	3.938	230.5
398.0	3.953	253.0
392.0	3.953	315.0
389.0	3.966	355.0
373.0	4.007	620.0
328.0	4.125	1380.0
323.5	4.139	1565.0

Appendix I-A

Table No. 17

Specimen No. 11 Polycrystal

Microstructure Tested: 50 min age at 155°C and 100 hrs at room temperature.

Test Conditions: Fracture in air.

"DCB" Geometry: Deflection 512.00 $\times 10^{-2}$ cm. Height H 1.2698 cm.Length L 8.260 cm. Width B 0.7850 cm. Width W 1.270 cm.

Force F (lbs.)	Crack Length L (cm.)	Time t (min.)
477.0	4.157	0
455.5	4.217	8.6
446.0	4.235	15.6
441.0	4.235	21.6
435.0	4.242	27.6
429.0	4.257	35.6
424.0	4.295	46.6
420.0	4.320	55.6
415.0	4.330	67.0
407.0	4.345	83.5
403.5	4.345	96.0
394.0	4.345	119.5
390.0	4.345	128.0
386.0	4.362	143.5
376.5	4.403	182.0
365.5	4.415	234.5
330.5	4.511	494.5

Appendix I-A

Table No. 18

Specimen No. 12 Polycrystal

Microstructure Tested: 15 min age at 155°C and 100 hrs at room temperature.

Test Conditions: Fracture in 0.5M NaCl.

"DCB" Geometry: Deflection $\delta 4.87 \times 10^{-2}$ cm. Height $H 1.2698$ cm.

Length L 8.340 cm. Width B 0.4140 cm. Width W 1.270 cm.

Force F (lbs.)	Crack Length L (cm.)	Time t (min.)
195.6	3.464	0
190.7	3.464	31.0
188.6	3.558	35.5
187.8	3.603	39.0
184.6	3.710	48.5
181.5	3.863	54.0
173.2	3.885	59.1
166.6	3.908	63.0
163.0	4.036	65.0
160.8	4.036	67.0
156.1	4.126	72.5
153.2	4.226	76.5
150.8	4.271	80.0
143.8	4.336	85.8
138.0	4.352	89.5
132.2	4.398	94.5

Appendix I-A

Table No. 19

Specimen No. 12 Polycrystal

Macrostructure tested: 15 min age at 155°C and 100 hrs at room temperature.

Test Conditions: Fracture in 0.5M NaCl.

'DCB" Geometry: Deflection 69.74×10^{-2} cm. Height H_1 2.2698 cm.Length L 8.340 cm. Width B_0 4.140 cm. Width W_1 2.70 cm.

Force F (lbs.)	Crack Length L (cm.)	Time t (min.)
231.5	4.650	0
218.5	4.791	3.5
213.5	4.895	5.5
205.0	5.091	8.0
197.5	5.131	9.5
187.0	5.170	13.0
178.0	5.315	16.5
171.0	5.367	19.0
163.5	5.415	21.5
157.5	5.473	23.7
152.0	5.473	25.8
147.2	5.518	28.0
143.5	5.559	30.0
139.0	5.797	32.5
134.0	5.866	36.5
128.0	5.956	39.5
121.0	6.043	44.0
118.6	6.087	46.3
114.5	6.220	51.0
111.5	6.257	54.6
106.0	6.297	62.5
100.0	6.407	69.8
97.5	6.504	74.1

Appendix I-A

Table No. 20

Specimen No. 13 Polycrystal

Microstructure Tested: 50 min age at 155°C and 100 hrs at room temperature.

Test Conditions: Fracture in Distilled H_2O .

"DCB" Geometry: Deflection $6.12.05 \times 10^{-2}$ cm. Height $H = 1.270$ cm.

Length L 8.360 cm. Width B 0.4150 cm. Width W 1.270 cm.

Force F (lbs.)	Crack Length L (cm.)	Time t (min.)
427.0	3.459	0
378.0	3.741	3.4
364.0	3.753	5.6
347.5	3.791	17.2
340.5	3.900	23.0
329.5	3.973	30.8
324.0	4.011	32.8
314.0	4.084	41.0
310.0	4.150	45.2
295.0	4.279	56.0
287.5	4.337	65.0
281.0	4.384	72.8
274.5	4.440	83.2
262.0	4.582	105.6
255.0	4.642	120.6
250.0	4.757	134.2
241.0	4.834	143.2
236.0	4.888	151.0
226.0	4.950	176.6
219.0	5.042	192.4
207.5	5.138	223.0
203.0	5.216	240.2
199.0	5.280	255.6
185.5	5.325	320.6
163.5	5.641	466.0
147.7	5.861	626.0
105.5	6.534	1261.0
78.0	7.105	1561.0

Appendix 1-A

Table No. 21

Specimen No. 1 Bi Crystal

Microstructure Tested: 50 min. age at 155°C and 100 hrs at room temperature.

Test Conditions: Fracture in 0.5M NaCl.

DCB Geometry: Length L 0.6954 in.

Deflection $6.7.95 \times 10^{-3}$ in. Height H 0.1512 in.

Width B 0.0368 in.

Specimen No. 2 Bi Crystal
Microstructure Tested: 50 min. age at 155°C and 100 hrs at room temperature.

Test Conditions: Fracture in 0.5M NaCl.

DCB Geometry: Length L 0.6110 in.

Deflection $6.7.20 \times 10^{-3}$ in. Height H 0.1500 in.

Width B 0.0358 in.

Force F (lbs)	Crack Length L (cm)	Time t (min.)	Force F (lbs)	Crack Length L (cm)	Time t (min.)
7.86	0.648	0.0	5.04	0.787	0
6.52	0.770	5.2	4.14	0.937	8.65
4.46	1.047	13.1	3.42	0.984	12.90
4.06	1.113	16.5	3.02	1.029	14.92
3.37	1.113	20.6	2.60	1.067	16.60
2.89	1.208	24.4	2.17	1.15	18.68
2.64	1.208	26.5	1.78	1.178	21.08
2.14	1.113	29.4	1.50	1.218	23.88
			1.20	1.247	25.58
			0.85	1.338	27.06
			0.67	1.374	28.20
			0.46	1.399	29.46

Appendix 1-A

Table No. 22

Specimen No. 3 Bi Crystal

Microstructure Tested: 50 min. age at 155°C and 100 hrs at room temperature.

Test Conditions: Fracture in 0.5M NaCl.

DCB Geometry: Length L 0.5290 in.

Deflection $6.7.90 \times 10^{-3}$ in. Height H 0.1262 in.

Width B 0.0285 in.

Specimen No. 4 Bi Crystal

Microstructure Tested: 50 min. age at 155°C and 100 hrs at room temperature.

Test Conditions: Fracture in 0.5M NaCl.

DCB Geometry:

Deflection $6.10.30 \times 10^{-3}$ in. Height H 0.1270 in.

Width B 0.0343 in.

Force F (lbs)	Crack Length L (cm)	Time t (min.)	Force F (lbs)	Crack Length L (cm)	Time t (min.)
4.78	0.676	0.0	3.96	1.005	0.0
3.76	0.707	15.3	3.21	1.044	13.7
3.40	0.740	18.0	3.08	1.072	15.7
3.04	0.751	21.2	2.74	1.136	20.2
2.56	0.808	24.3	2.48	1.233	23.9
2.31	0.872	27.6	2.39	1.308	25.5
* 1.80	0.917	31.5	2.19	1.351	29.3
* 1.50	1.068	32.7	2.02	1.394	32.5
* 1.04	1.133	34.3	1.82	1.463	36.5
			1.68	1.494	39.7
			1.43	1.540	45.7

* A sharp change in grain boundary direction.

Appendix 1-A

Table No. 23

Specimen No. 7 Bi-Crystal

Microstructure Tested: 50 min. age at 155°C and 100 hrs at room temperature.

Test Conditions: Fracture in 0.5M NaCl.

DCB Geometry: Length L 0.7168 in.

Deflection δ 7.30 x 10⁻³ in. Height H 0.2020 in.

Width B 0.0376 in.

Specimen No. 9 Bi-Crystal

Microstructure Tested: 50 min. age at 155°C and 100 hrs at room temperature.

Test Conditions: Fracture in 0.5M NaCl.

DCB Geometry: Length L 0.5820 in.

Deflection δ 5.20 x 10⁻³ in. Height H 0.1880 in.

Width B 0.0372 in.

Force F (lbs)	Crack Length L (cm)	Time t (min.)	Force F (lbs)	Crack Length L (cm)	Time t (min.)
7.40	0.849	0	8.80	0.629	0
5.80	0.992	10.0	6.80	0.850	10.0
3.60	1.259	18.6	4.80	0.884	14.0
3.10	1.386	25.0	4.20	1.020	16.0
			3.54	1.020	19.0
			3.02	1.066	23.0
			2.50	1.066	27.0
			2.04	1.142	29.6

Appendix 1-A

Table No. 24Specimen No. 10 Bi-Crystal

Microstructure Tested: 50 min. age at 155°C and 100 hrs at room temperature.

Test Conditions: Fracture in 0.5M NaCl.

DCB Geometry: Length L 1.0009 in.

Deflection δ 8.10 x 10⁻³ in. Height H 0.1923 in.

Width B 0.0266 in.

Specimen No. 12 Bi-Crystal

Microstructure Tested: 50 min. age at 155°C and 100 hrs at room temperature.

Test Conditions: Fracture in 0.5M NaCl.

DCB Geometry:

Deflection δ 6.20 x 10⁻³ in. Height H 0.2211 in.

Width B 0.0362 in.

Force <u>F</u> (lbs)	Crack Length <u>L</u> (cm)	Time <u>t</u> (min.)	Force <u>F</u> (lbs)	Crack Length <u>L</u> (cm)	Time <u>t</u> (min.)
6.80	0.755	0.0	6.87	0.964	0.0
6.40	0.797	6.0	4.44	1.236	20.0
5.80	0.854	9.6	3.72	1.288	26.0
4.60	0.949	12.0	3.24	1.303	30.2
3.92	1.012	14.0	2.88	1.333	32.6
3.50	1.085	16.4	2.48	1.412	35.0
2.58	1.149	19.4	2.10	1.461	38.6
2.21	1.149	20.4			
1.50	1.296	23.0			
1.01	1.401	25.0			

Appendix 1-A

Table No. 25

Specimen No. 13 Bi-Crystal

Microstructure Tested: 50 min. age at 155°C and 100 hrs at room temperature.

Test Conditions: Fracture in 0.5M NaCl.

DCB Geometry:

Length L 0.7299 in.

Deflection δ 6.83×10^{-3} in. Height H 9.2135 in.

Width B 0.0358 in.

Specimen No. 15 Bi-Crystal

Microstructure Tested: 50 min. age at 155°C and 100 hrs at room temperature.

Test Conditions: Fracture in 0.5M NaCl.

DCB Geometry:

Length L 0.5186 in.

Deflection δ 5.83×10^{-3} in. Height H 0.1639 in.

Width B 0.0378 in.

Force F (lbs)	Crack Length L (cm)	Time t (min.)	Force F (lbs)	Crack Length L (cm)	Time t (min.)
7.16	0.931	0.0	6.52	0.686	0.0
6.26	0.969	8.4	6.15	0.725	8.1
5.68	1.000	13.2	5.20	0.786	18.4
5.02	1.056	18.2	4.95	0.816	20.8
4.31	1.089	21.8	4.12	0.932	28.5
3.41	1.131	26.6			
2.20	1.325	30.6			

Appendix 1-A

Table No. 26Specimen No. 17 Bi-Crystal

Microstructure Tested: 50 min. age at 155°C and 100 hrs at room temperature.

Test Conditions: Fracture in 0.5M NaCl.

DCB Geometry: Length L 0.4839 in.Deflection δ 5.80 × 10⁻³ in. Height H 0.1433 in.Width B 0.0371 in.Specimen No. 18 Bi-Crystal

Microstructure Tested: 50 min. age at 155°C and 100 hrs at room temperature.

Test Conditions: Fracture in 0.5M NaCl.

DCB Geometry:

Length L 0.5286 in.Deflection δ 6.00 × 10⁻³ in. Height H 0.1661 in.Width B 0.0374 in.

Force F (lbs)	Crack Length L (cm)	Time t (min.)	Force F (lbs)	Crack Length L (cm)	Time t (min.)
7.72	0.523	0.0	7.18	0.591	0.0
6.05	0.645	7.5	5.40	0.701	16.0
5.20	0.700	9.0	4.80	0.744	19.0
4.58	0.785	11.5	4.20	0.861	22.0
3.40	0.845	14.0	3.30	0.922	25.4
1.33	1.045	17.5	2.90	0.961	27.6

Appendix 1-A

Table No. 27

Specimen No. 19 Bi-Crystal

Microstructure Tested: 50 min. age at 155°C and 100 hrs at room temperature.

Test Conditions: Fracture in 0.5M NaCl.

DCB Geometry: Length L 0.6397 in.

Deflection δ 5.60 x 10⁻³ in. Height H 0.1752 in.

Width B 0.0371 in.

Specimen No. 20 Bi-Crystal

Microstructure Tested: 50 min. age at 155°C and 100 hrs at room temperature.

Test Conditions: Fracture in 0.5M NaCl.

DCB Geometry: Length L 0.5240 in.

Deflection δ 6.00 x 10⁻³ in. Height H 0.1912 in.

Width B 0.0370 in.

Force F (lbs)	Crack Length L (cm)	Time t (min.)	Force F (lbs)	Crack Length L (cm)	Time t (min.)
6.76	0.706	0.0	7.92	0.645	0.0
6.70	0.706	15.0	6.80	0.699	12.8
5.30	0.808	22.5	6.33	0.741	17.8
4.20	1.032	32.4	5.60	0.823	23.2
3.40	1.086	35.0	4.43	0.909	28.0
2.70	1.132	38.0	3.00	0.998	34.6
1.62	1.193	41.0	2.00	1.065	38.4

Appendix 1-A

Table No. 28

Specimen No. 23 Bi-Crystal

Microstructure Tested: 50 min. age at 155°C and 100 hrs at room temperature.

Test Conditions: Fracture in 0.5M NaCl.

DCB Geometry: Length L 0.5430 in.

Deflection δ 6.40 x 10⁻³ in. Height H 0.1870 in.

Width B 0.0365 in.

Force F (lbs)	Crack Length L (cm)	Time t (min.)	Force F (lbs)	Crack Length L (cm)	Time t (min.)
7.24	0.592	0.0	6.58	0.982	0.0
6.40	0.681	5.0	6.40	0.982	7.0
5.30	0.840	11.0	5.32	1.091	19.4
4.55	0.936	15.0	5.04	1.117	24.2
			4.50	1.173	28.6
			3.70	1.229	32.6
			3.00	1.364	38.8
*	2.70	*	2.40	1.428	41.0
				1.540	43.4

* Grain Boundary Curves Sharply.

Appendix 1-A

Table No. 29

Specimen No. 27 Bi-Crystal

Microstructure Tested: 50 min. age at 155°C and 100 hrs at room temperature.

Test Conditions: Fracture in 0.5M NaCl.

DCB Geometry:
 Deflection 6×10^{-3} in. Height $H 0.1818$ in.
 Width $B 0.0372$ in.

DCB Geometry:
 Length $L 0.5690$ in.
 Deflection 6×10^{-3} in. Height $H 0.1942$ in.
 Width $B 0.0346$ in.

Specimen No. 31 Bi-Crystal

Microstructure Tested: 50 min. age at 155°C and 100 hrs at room temperature.

Test Conditions: Fracture in 0.5M NaCl.

Force F (lbs)	Crack Length L (cm)	Time t (min.)	Force F (lbs)	Crack Length L (cm)	Time t (min.)
9.12	0.785	0.0	11.36	1.082	0.0
5.14	0.938	22.2	10.10	1.161	9.4
4.20	0.988	25.0	9.20	1.225	17.5
3.52	1.038	27.8	8.10	1.285	22.6
2.32	1.076	32.4	7.50	1.315	29.0
1.40	1.182	35.0	6.13	1.394	39.0
			5.30	1.461	42.5

Appendix 1-A

Table No. 30Specimen No. 32 Bi-Crystal

Microstructure Tested: 50 min. age at 155°C and 100 hrs at room temperature.

Test Conditions: Fracture in 0.5M NaCl.

DCB Geometry:

Deflection δ 10.10×10^{-3} in. Height H 0.1956 in.Width B 0.0386 in.Specimen No. _____

Microstructure Tested: 50 min. age at 155°C and 100 hrs at room temperature.

Test Conditions: Fracture in 0.5M NaCl.

DCB Geometry:

Length L 0.8012 in.Deflection δ _____Width B _____

Force F (lbs)	Crack Length L (cm)	Time t (min.)	Force F (lbs)	Crack Length L (cm)	Time t (min.)
11.87	1.077	0.0			
10.50	1.165	15.0			
9.98	1.195	16.2			
9.00	1.242	18.8			
8.38	1.272	21.6			
7.76	1.285	24.4			
7.26	1.326	27.0			
6.70	1.380	30.4			
6.15	1.415	33.6			
5.68	1.446	37.2			
5.16	1.486	42.0			
4.70	1.555	46.0			
4.32	1.596	48.2			

Appendix I-B

Specimen No.	Experimental Elastic Strain Energy Released G (KGMS/cm)	Experimental Fracture Toughness K _C (KGMS/cm ^{3/2})	Calculated Fracture Toughness K _{CC} (KGMS/cm ^{3/2})	DCB Geometric Constant Δ	Average Crack Velocity V(cm/min)
	$G = \delta/2 \cdot B \times dF/dL$	$K_C = \left[\frac{E}{(1 - \nu^2)} \right]^{1/2}$	$K_{CC} = \frac{3 \cdot 46 \times F}{B \times H^{3/2}} [L + 0.7H]$	$\Delta = K_C/K_{CC}$	$V = dL/dt$
1 Polycrystal	11.89 9.56 7.37 6.45 5.37	3090 2760 2435 2275 2075 2075	4900 4325 4030 3500 3150 2880	.63 .64 .61 .65 .65 .72	12.35×10^{-3} 7.63×10^{-3} 3.70×10^{-3} 2.20×10^{-3} 1.35×10^{-3} 1.13×10^{-4}
1 Polycrystal	7.65 6.57 4.71	2480 2300 1940	3600 3440 2850	.69 .67 .68	1.98×10^{-3} 1.27×10^{-3} 0.41×10^{-3}
2 Polycrystal	6.99 6.99 -	2380 2380 -	3370 3130 2800	.71 .76 -	4.19×10^{-3} 1.33×10^{-3} 0.55×10^{-3}

Appendix I-B

Specimen No.	Experimental Elastic Strain Energy Released G (KGMS/cm)	Experimental Fracture Toughness K_c (KGMS/cm ^{3/2})	Calculated Fracture Toughness K_{CC} (KGMS/cm ^{3/2})	DCB Geometric Constant Δ	Average Crack Velocity V(cm/min)
	$G = \delta/2 \times B \times dF/dL$	$K_c = \left[\frac{E(y)}{B \times H^3/2} \right]^{1/2}$	$K_{CC} = \frac{3.46 \times F}{B \times H^3/2} [L + 0.7H]$	$\Delta = K_c/K_{CC}$	$V = dL/dt$
3 Polycrystal	6.70 5.53 4.72 4.21 3.92 3.06	2320 2110 1950 1840 1770 1570	3910 3560 3330 3160 2920 2580	.60 .60 .59 .59 .60 .60	3.96×10^{-3} 3.18×10^{-3} 1.60×10^{-3} 1.21×10^{-3} 0.61×10^{-3} 0.61×10^{-3}
3 Polycrystal	11.85 10.25 8.65 5.55 -	3080 2870 2640 2110 -	4650 4100 3730 3280 2700	.66 .70 .70 .66 -	7.69×10^{-3} 5.27×10^{-3} 3.33×10^{-3} 1.91×10^{-3} 1.03×10^{-3}

Appendix I-B

Specimen No.	Experimental Elastic Strain Energy Released G (KGMS/cm)	Experimental Fracture Toughness K_c (KGMS/cm ^{3/2})	Calculated Fracture Toughness K_{CC} (KGMS/cm ^{3/2})	DCB Geometric Constant Δ	Average Crack Velocity V(cm/min)
	$G = \frac{d}{2} \cdot B \times dF/dL$	$K_c = \left[\frac{E(y)}{1 - \nu^2} \right]^{1/2}$	$K_{CC} = \frac{3 \cdot 4.6 \times F}{B \times H^{3/2}} [L + 0.7H]$	$\Delta = K_c/K_{CC}$	$V = dL/dt$
4 Polycrystal	2.65 1.87 2.00 * 5.15	1460 1225 1265 2040	2165 2020 1825 985	.67 .61 .69 2.07	3.56×10^{-2} 2.31×10^{-2} 1.51×10^{-2} 0.73×10^{-2}
5 Polycrystal	.09 1.09 1.09	900 900 900	1375 1275 1150	.65 .70 .78	1.10×10^{-2} 0.98×10^{-2} 0.65×10^{-2}
6 Polycrystal	2.22 * 1.72	1320 1170	1800 1130	.73 1.04	2.00×10^{-2} 1.00×10^{-2}
6 Polycrystal	0.66	730	1110	.66	0.42×10^{-2}

* End effects of free surface.

Appendix I-B

Specimen No.	Experimental Elastic Strain Energy Released G (KGMS/cm)	Experimental Fracture Toughness K_c (KGMS/cm ^{3/2})	Calculated Fracture Toughness K_{cc} (KGMS/cm ^{3/2})	DCB Geometric Constant Δ	Average Crack Velocity V(cm/min)
	$G = \delta/2 \cdot B \times dF/dL$	$K_c = \left[\frac{E(Y)}{(1-\nu^2)} \right]^{1/2}$	$K_{cc} = \frac{3.46 \times F}{B \times H^{3/2}} [L + 0.7H]$	$\Delta = K_c/K_{cc}$	$V = dL/dt$
7 Polycrystal	4.15 4.15 3.16 3.16 2.54 1.85	1835 1835 1600 1600 1425 1220	3350 3210 2825 2750 2540 2230	.55 .57 .57 .58 .57 .55	1.40×10^{-2} 1.07×10^{-2} 0.82×10^{-2} 0.60×10^{-2} 0.43×10^{-2} 0.32×10^{-2}
7 Polycrystal	6.22 6.22 4.75	2240 2240 1950	3890 3645 3400	.58 .62 .57	2.23×10^{-2} 1.50×10^{-2} 1.35×10^{-2}
8 Polycrystal	9.5 -	2750 -	4100 4000	.67 -	0.60×10^{-3} 0.60×10^{-3}

Appendix I-B

Specimen No.	Experimental Elastic Strain Energy Released G (KGMS/cm)	Experimental Fracture Toughness K_C (KGMS/cm ^{3/2})	Calculated Fracture Toughness K_{CC} (KGMS/cm ^{3/2})	DCB Geometric Constant Δ	Average Crack Velocity V(cm/min)
	$G = \delta/2 \times B \times dF/cL$	$K_C = \left[\frac{E(Y)}{(1-\nu^2)} \right]^{1/2}$	$K_{CC} = \frac{3 \cdot 46 \times F}{B \times H^{3/2}} [L + 0.7H]$	$\Delta = K_C/K_{CC}$	$V = dL/dt$
9 Polycrystal	12.12 9.55 7.85 6.31 6.31 4.99	3110 2760 2500 2225 2225 2000	4500 4060 3620 3400 3190 2970	.70 .68 .69 .66 .70 .67	7.85×10^{-4} 6.66×10^{-4} 5.20×10^{-4} 3.81×10^{-4} 2.75×10^{-4} 0.68×10^{-4}
9 Polycrystal	15.10 11.45 7.39 6.03	3480 3030 2440 2200	5060 4540 4060 3800	.68 .67 .60 .58	15.10×10^{-4} 11.90×10^{-4} 8.00×10^{-4} 3.45×10^{-4}
10 Polycrystal	-	-	1870	-	0.0

Appendix I-B

Specimen No.	Experimental Elastic Strain Energy Released G (KGMS/cm)	Experimental Fracture Toughness K _C (KGMS/cm ^{3/2})	Calculated Fracture Toughness K _{CC} (KGMS/cm ^{3/2})	DCE Geometric Constant Δ	Average Crack Velocity V(cm/min)
	$G = \delta/2 \times B \times dF/dL$	$K_C = \left[\frac{E(y)}{(1-\nu^2)} \right]^{1/2}$	$K_{CC} = \frac{3 \cdot 4.6 \times F}{B \times H^{3/2}} [L + 0 \cdot 7H]$	$\Delta = K_C/K_{CC}$	$V = dL/dt$
11 Polycrystal	12.80 9.40	3200 2750	3150 2720	1.02 1.00	4.65×10^{-3} 1.00×10^{-3}
11 Polycrystal	12.70	3180	3100	1.03	3.08×10^{-3}
12 Polycrystal	5.18 5.18 2.48	2030 2030 1410	3290 3050 2280	.62 .67 .62	5.08×10^{-2} 4.00×10^{-2} 2.40×10^{-2}
12 Polycrystal	1.95 1.80	1250 1200	2190 2025	.57 .59	1.70×10^{-2} 1.20×10^{-2}

Appendix I-B

Specimen No.	Experimental Elastic Strain Energy Released G (KGMS/cm)	Experimental Fracture Toughness K _C (KGMS/cm ^{3/2})	Calculated Fracture Toughness K _{CC} (KGMS/cm ^{3/2})	DCB Geometric Constant Δ	Average Crack Velocity V(cm/min)
	$G = \delta/2 \cdot B \times dF/dL$	$K_C = \left[\frac{E(Y)}{(1-\nu^2)} \right]^{1/2}$	$K_{CC} = \frac{3.46 \times F}{B \times H^{3/2}} [L + 0.7H]$	$\Delta = K_C/K_{CC}$	$V = dL/dt$
13 Polycrystal	10.90 8.71 7.05 6.05 6.05 4.93 3.78	2950 2650 2370 2200 2200 1990 1740	4510 4160 3750 3380 3030 2730 2360	.66 .64 .63 .65 .72 .73 .73	1.82×10^{-2} 1.15×10^{-2} 0.63×10^{-2} 0.36×10^{-2} 0.19×10^{-2} 0.14×10^{-2} 0.10×10^{-2}

Appendix I-C

Bi-Crystal No.	Average Elastic Strain Energy Released G (KGMS/cm)	Average Crack Velocity V (cm/min)	Bi-Crystal Orientation Characterized by 5 Degrees of Freedom (See Figure 15)					
	$G = \delta/2B \times dF/dL$	$V = dL/dt$	α_{100}	β_{100}	γ_{111}	Δ	ϵ	
1	0.45	2.86×10^{-2}	24	28	10	173	90	
2	0.27	2.00×10^{-2}	59	2	35	68	0	
4	0.33	1.60×10^{-2}	73	0	11	4	94	
7	0.41	2.00×10^{-2}	7	56	31	82	62	
9	0.42	2.17×10^{-2}	42	0	27	35	107	
12	0.38	1.25×10^{-2}	8	46	8	94	21	
15	0.36	2.60×10^{-2}	26	3	10	84	14	
17	REGION A	0.44	2.80×10^{-2}	19	2	23	117	2
18		0.42	2.10×10^{-2}	83	0	60	91	89
19		0.34	1.90×10^{-2}	26	27	25	86	16
20		0.50	1.45×10^{-2}	24	13	4	76	16
24		0.49	1.50×10^{-2}	35	15	20	65	3
23		0.31	2.50×10^{-2}	12	11	14	83	4
3	REGION B	0.83	1.23×10^{-2}	31	0	7	32	110
10		0.76	2.70×10^{-2}	62	13	116	134	94
13		0.81	0.64×10^{-2}	26	11	33	83	15
27		1.07	1.06×10^{-2}	55	2	43	60	12
32		0.94	1.18×10^{-2}	27	21	45	89	15
31	REGION C	1.39	1.00×10^{-2}	6	4	10	90	0

Appendix I-D

Sample Calculations

$$1. \quad G_L = \frac{\delta}{2 \times B} \times \left(\frac{dF}{dL} \right)_L = 4.15 \text{ kgs/cm}$$

$$\delta = 6.72 \times 10^{-2} \text{ cm.} \quad B = 0.42 \text{ cm.}$$

$$\left(\frac{dF}{dL} \right)_L \approx \left(\frac{\Delta F}{\Delta L} \right)_L = (52 \text{ kgs/cm})_{3.43 \text{ cm.}}$$

$$L = 3.43 \text{ cm.} \quad F = 290.5 \text{ lbs.}$$

$$2. \quad K_C = \left[\frac{E(y) \times G_L}{(1 - \nu^2)} \right]^{1/2} = 1835 \text{ kgs/cm}^{3/2}$$

$$E(y) = 7.10 \text{ kgs/cm}^2 \quad \nu = 0.33$$

$$3. \quad K_{CC} = \frac{3.46 \times F}{B \times H^{3/2}} [L + 0.7H] = 3350 \text{ kgs/cm}^{3/2}$$

$$L = 3.43 \text{ cm.} \quad F = 290.5 \text{ lbs} \quad H = 1.27 \text{ cm.}$$

$$4. \quad \Delta = K_C / K_{CC} = .55$$

*The average Δ determined from all the DCB tests is: $0.64 \pm .08$

$$5. \quad K'_{CC} = K_C = \frac{2.22 \times F}{B \times H^{3/2}} [L + 0.7H]$$

$$6. \quad V = \left(\frac{dL}{dt} \right)_L = 1.40 \times 10^{-2} \text{ cm/min.}$$

$$\left(\frac{dL}{dt} \right)_L \approx \left(\frac{\Delta L}{\Delta t} \right)_L = 1.40 \times 10^{-2} \text{ cm/min.}$$

Appendix II-A

Each individual dislocation in a linear array is assumed to obey a velocity (V) - stress (τ) relation of the form:

$$V_i = V_o \times \left(\frac{\tau_{\text{Effective}}}{\tau_o} \right)^m, \quad (\text{A.1})$$

where τ_o is the shear stress necessary to move a dislocation at $V = 1 \text{ cm/sec.}$, and m is a constant characteristic of the material. $\tau_{\text{Effective}}$ is the applied stress minus the back stress of dislocations in the linear array and neglects any internal stress of the microstructure. If the above relation is valid, then the following calculations for describing the time dependence of linear pile-ups can be carried out.

Consider individual dislocations travelling different distances, X , on an active slip plane and eventually forming a linear array over a distance d_N from the blocking obstacle; see Figure (43). Let $X_{(i)}$ be the distance from the active source on the slip plane to the stable position of the i^{th} dislocation in the linear array, d_N . Then the time to build up a linear array over a distance d_N is the sum of the time increments for each individual dislocation in the array in travelling $X_{(i)}$, $X_{(i+1)}$, $X_{(i+2)}$, etc.

This summation of time increments implies that each dislocation emitted from the source must wait until the preceding dislocation has assumed its place in the blocked array before it can move down the slip plane. For each individual dislocation in the schematic we can write $t_{(i)} = \frac{X_{(i)}}{V_{(i)}}$ where $t_{(i)}$ is the time required for the i^{th} dislocation to reach its stable position in the linear array,

and a summation over N dislocations yields:

$$t_{(N)} = \sum_{i=1}^{N-1} \frac{X_{(i)}}{V_{(i)}} \quad (A.2)$$

where $t_{(N)}$ is the time required to build up an array of N dislocations. The distance $X_{(i)}$ for the i^{th} dislocation to move is $[R_c - d_{(i-1)}]$ and $d_{(i-1)}$ is the extent of $(i-1)$ dislocations in the pile-up.

The velocity, V_i , in Eq. (A.2) can be evaluated by expressing the effective shear stress on the i^{th} dislocation in terms of the applied stress and the back stress due to $(i-1)$ dislocations. $\tau_{(\text{back stress})}$ is the cumulative effect of N positive edge dislocations in the linear array on the source dislocation.

Since like dislocations repel each other, $\tau_{\text{back stress}}$ opposes τ_{applied} and the back stress can be evaluated by replacing N dislocations in a linear array by a single large dislocation located at the stress field centroid of the linear array.

The distance of the stress field centroid, \bar{R} , of a linear array of dislocations acting on the active source dislocation can be approximated as $\bar{R} \approx R_c$ for $d_{(N)}/R_c \approx 0$. As $d_{(N)}$ increases $\bar{R} \approx [R_c - d_{(N)}/4]$ for $0.2 \leq d_{(N)}/R_c \leq 0.8$. These approximations are based on calculations involving the sums of the elastic stress field distribution of N dislocations in an array can be replaced by a single large dislocation with a Burger's vector equal to N b and located at approximately a distance of $R_c - d_{(N)}/4$ from the source dislocation. Using this equivalent stress field, the back stress can be evaluated as:

$$\tau_{\text{back stress}} = N \times \sigma_{r,\varphi} \quad (A.3)$$

where $\sigma_{r,\phi}$ (single edge dislocation) = $\frac{\mu \cdot b}{2\pi(1-\nu)} \times \frac{\cos \phi}{R}$. For dislocations on the same slip plane $\cos \phi = 1$, and \bar{R} is the distance between the stress field centroid of (i-1) piled-up dislocations and the moving i^{th} dislocation. To facilitate calculations involving $\tau_{\text{back stress}}$, a constant distance of $\bar{R} = [R_c - d_{(i-1)}/4]$ was chosen. This approximate value of \bar{R} generally represents the maximum distance between the stress field centroid of the pile-up and the moving dislocation when compared to the exact solution of \bar{R} . The choice of \bar{R} leads to a minimum $\tau_{\text{back stress}}$ and a maximum in the velocity of the i^{th} dislocation (see Eq. (A.1)) which relates $v_{(i)}$ to $\tau_{\text{back stress}}$.

For a given applied shear stress, τ_{applied} , and a given number of dislocations in the linear array, N ; $d_{(i-1)}$, $\tau_{\text{back stress}}$, and $t_{(N)}$ can be calculated:

$$t_{(N)} = \frac{\tau_o}{v_o} \sum_{i=1}^N \frac{[R_c - d_{(i-1)}]}{[\tau_{\text{applied}} - \tau_{\text{back stress}}]^m} \quad (\text{A.4})$$

$$d_{(i-1)} = (i-1) \mu b / \pi (1-\nu) \tau_{\text{applied}}$$

$$\tau_{\text{back stress}} = \left\{ \left[(i-1) \times \mu \times b \right] / 2\pi(1-\nu) \left[R_c - \frac{d_{(i-1)}}{4} \right] \right\}.$$

Appendix II-B

Material and Microstructural Constants Used in Computer Program to Simulate Intergranular Fracture in Air

$R_c = 10^{-1}$ cm. (measured grain size of polycrystal specimens)

$\mu = 2.6 \times 10^{11}$ dynes/cm² (shear modulus for aluminum alloys)

$\nu = 0.33$ (Poisson's Ratio for aluminum alloys)

$b = 2 \times 10^{-8}$ cm (Estimated Burger's vector)

$\sigma_{\text{fracture}} = 2.04 \times 10^{11}$ dynes/cm² (Theoretical cohesive strength)

$S = 10^{-4}$ cm. (Measured for Microstructure No. I)

$\tau_o = 10^9 \sim 10^8$ dynes/cm²

$m = 2$

$V_o = 1$ cm/sec

} (see discussion in section VII.E)

Appendix II-B

Computer Program For Calculating the time, t, required for fracture over a crack length, S, and under a changing stress intensity factor, K. The geometry of No. 3 Polycrystal (Appendix I-A and Table 4) and the constants in Appendix II-B were used to simulate fracture.

```

0000100  REAL *4 MULT
0000150  KELT? (6.1002)
0000200  READ(6,1003) FACTOR
0000225  WRITE(6,1005)
0000250  READ(6,1003) SSFACT
0000300  LEFACT=FACT*FACT
0000400  IKK=0
0000500  TIME=1.2
0000600  FK=2.55E09
0000700  A=4.3
0000800  MULT=SSFACT*FACTOR
0000900  KELT? (6.1004) MULT
0001000  WRITE(9,1004) MULT
0001100  AF=5.95
0001200  N1P=(AF-A)/MULT
0001300  WRITE(6,1005)
0001400  WRITE(9,1000)
0001500  DC 122 I=1,MIT
0001600  A=A+MULT
0001700  Q=A-MULT/2
0001800  DELK=(-4.28E2.8+1.273E6)*SSFACT*FACTOR
0001900  FK=K+DELK
0002000  FNDISL=((12.34*1.0E39-0.8)*FK)/37.0)*2)/FK
0002100  NDISL=FNDISL
0002200  CCRSK=.3C02*FK
0002300  SJ4=0.0
0002400  DO 200 J=1,NDISL
0002500  FJ=FL0AT(J)
0002600  SJ4=SJ4+(.157*FK-3.14E3*(FJ-1.))/(CONSK-3.* (FJ-1.))/ (CONSK-(FJ-1.)))**2
0002700  200 CONTINUE

```

Appendix II-B

```

2002800  DELT=99.636E13/2K**3
0002200  TIT=TITLE+FACTO1+DELT
3003500  IAK=IAK+1
0003100  IX=IXA*FACT
2003300  IF(IX.GE.1000) GO TO 1
0003400  GO TO 100
2003500  1 IFIX=1*FACT
3003600  WRITE(6,1001) TIT,TA,TIT,NDISI,PK
0003700  WRITE(9,1001) TIT,TA,TIT,NDISI,PK
5003800  IAK=,
0003900  100  CONTINUE
500400  ITIT=1*FACT
0004100  WRITE(6,1001) TIT,TA,TIT,NDISI,PK
5004200  WRITE(3,1001) TIT,TA,TIT,NDISI,PK
0004300  1000  FORMAT(1X,VS15D,SY5,9X,V15THY,9X,VNUMBER,9X,VSTRESS//)
5004400  1001  FORMAT(1H,TS,2Y,F13.5,X,G13.6,2Y,I11,2X,I13.6,1X)
0004500  1002  FORMAT(V15BT,FACTR9)
0004600  1003  FORMAT(9X,F7.0)
5004700  1004  FORMAT(V15BT,V15BT,INCEMENT = 9,57.5)
0004750  1005  FORMAT(V15BT,SSPAC9)
5004800  STOP
0004900  END

```

B.3

DISCLAIMER NOTICE

THIS DOCUMENT IS THE BEST
QUALITY AVAILABLE.

COPY FURNISHED CONTAINED
A SIGNIFICANT NUMBER OF
PAGES WHICH DO NOT
REPRODUCE LEGIBLY.

BLANK PAGE

Unclassified

Security Classification

DOCUMENT CONTROL DATA - R&D

(Security classification of title, body of abstract and indexing annotation must be entered when the overall report is classified)

1. ORIGINATING ACTIVITY (Corporate author)		2a. REPORT SECURITY CLASSIFICATION	
Dept. of Metallurgy and Materials Science Carnegie-Mellon University Pittsburgh, Pa. 15213		Unclassified	
2b. GROUP			
3. REPORT TITLE			
Intergranular Fracture in an Al-15wt. % Zn Alloy			
4. DESCRIPTIVE NOTES (Type of report and inclusive dates)			
Final Technical Report			
5. AUTHOR(S) (Last name, first name, initial)			
Kovacs, W. J. and Low, J. R., Jr.			
6. REPORT DATE		7a. TOTAL NO. OF PAGES	7b. NO. OF REFS
February 1970		230	105
8a. CONTRACT OR GRANT NO.		9a. ORIGINATOR'S REPORT NUMBER(S)	
Nonr-760(31)			
b. PROJECT NO.			
C-7			
c.			
d.		9b. OTHER REPORT NO(S) (Any other numbers that may be assigned this report)	
10. AVAILABILITY/LIMITATION NOTICES			
Distribution of this document is unlimited and reproduction in whole or in part is permitted for any purpose of the U. S. Government			
11. SUPPLEMENTARY NOTES		12. SPONSORING MILITARY ACTIVITY	
		Advanced Research Projects Agency Washington, D. C.	
13. ABSTRACT Cracking kinetics involved in the intergranular fracture of an Al-15wt% Zn alloy tested in air, distilled H_2O , and 0.5M NaCl have been studied by means of the elastic strain energy released during crack propagation in a double cantilever beam specimen. This technique has been applied to two different types of specimens: polycrystals with equi-axed grains and bi-crystals with crack propagation confined to the grain boundary. By varying the microstructure through selective aging treatments, a wide range of cracking susceptibility has been observed. The results show that the fracture toughness of this alloy increases with a decreasing volume fraction of G. P. zones in the matrix. A similar trend in the stress-corrosion cracking tests in 0.5M NaCl is noted, and the susceptibility to fracture increases as the volume fraction of G. P. zones in the matrix increases. The microstructure highly susceptible to fracture exhibits planar slip traces while the more resistant microstructures show a dispersed type surface slip pattern. The dependence of cracking rates on the microstructure is explained in terms of inhomogeneous plastic flow in the matrix being blocked by grain boundaries and leading to severe stress concentrations at the boundaries. The bi-crystal tests substantiate these results and show that orientations favoring partial continuity of slip bands across grain boundaries are less susceptible to stress corrosion cracking than arbitrarily oriented boundaries with no slip continuity.			

Unclassified

Security Classification

14.	KEY WORDS	LINK A		LINK B		LINK C	
		ROLE	WT	ROLE	WT	ROLE	WT
	Al-Zn Alloy Intergranular Fracture Stress-Corrosion Heat Treatment Microstructure Bi-Crystal Grain Boundary Misorientation Deformation						

INSTRUCTIONS

1. ORIGINATING ACTIVITY: Enter the name and address of the contractor, subcontractor, grantee, Department of Defense activity or other organization (corporate author) issuing the report.

2a. REPORT SECURITY CLASSIFICATION: Enter the overall security classification of the report. Indicate whether "Restricted Data" is included. Marking is to be in accordance with appropriate security regulations.

2b. GROUP: Automatic downgrading is specified in DoD Directive 5200.10 and Armed Forces Industrial Manual. Enter the group number. Also, when applicable, show that optional markings have been used for Group 3 and Group 4 as authorized.

3. REPORT TITLE: Enter the complete report title in all capital letters. Titles in all cases should be unclassified. If a meaningful title cannot be selected without classification, show title classification in all capitals in parenthesis immediately following the title.

4. DESCRIPTIVE NOTES: If appropriate, enter the type of report, e.g., interim, progress, summary, annual, or final. Give the inclusive dates when a specific reporting period is covered.

5. AUTHOR(S): Enter the name(s) of author(s) as shown on or in the report. Enter last name, first name, middle initial. If military, show rank and branch of service. The name of the principal author is an absolute minimum requirement.

6. REPORT DATE: Enter the date of the report as day, month, year, or month, year. If more than one date appears on the report, use date of publication.

7a. TOTAL NUMBER OF PAGES: The total page count should follow normal pagination procedures, i.e., enter the number of pages containing information.

7b. NUMBER OF REFERENCES: Enter the total number of references cited in the report.

8a. CONTRACT OR GRANT NUMBER: If appropriate, enter the applicable number of the contract or grant under which the report was written.

8b, 8c, & 8d. PROJECT NUMBER: Enter the appropriate military department identification, such as project number, subproject number, system numbers, task number, etc.

9a. ORIGINATOR'S REPORT NUMBER(S): Enter the official report number by which the document will be identified and controlled by the originating activity. This number must be unique to this report.

9b. OTHER REPORT NUMBER(S): If the report has been assigned any other report numbers (either by the originator or by the sponsor), also enter this number(s).

10. AVAILABILITY/LIMITATION NOTICES: Enter any limitations on further dissemination of the report, other than those

imposed by security classification, using standard statements such as:

- (1) "Qualified requesters may obtain copies of this report from DDC."
- (2) "Foreign announcement and dissemination of this report by DDC is not authorized."
- (3) "U. S. Government agencies may obtain copies of this report directly from DDC. Other qualified DDC users shall request through _____."
- (4) "U. S. military agencies may obtain copies of this report directly from DDC. Other qualified users shall request through _____."
- (5) "All distribution of this report is controlled. Qualified DDC users shall request through _____."

If the report has been furnished to the Office of Technical Services, Department of Commerce, for sale to the public, indicate this fact and enter the price, if known.

11. SUPPLEMENTARY NOTES: Use for additional explanatory notes.

12. SPONSORING MILITARY ACTIVITY: Enter the name of the departmental project office or laboratory sponsoring (paying for) the research and development. Include address.

13. ABSTRACT: Enter an abstract giving a brief and factual summary of the document indicative of the report, even though it may also appear elsewhere in the body of the technical report. If additional space is required, a continuation sheet shall be attached.

It is highly desirable that the abstract of classified reports be unclassified. Each paragraph of the abstract shall end with an indication of the military security classification of the information in the paragraph, represented as (TS), (S), (C), or (U).

There is no limitation on the length of the abstract. However, the suggested length is from 150 to 225 words.

14. KEY WORDS: Key words are technically meaningful terms or short phrases that characterize a report and may be used as index entries for cataloging the report. Key words must be selected so that no security classification is required. Identifiers, such as equipment model designation, trade name, military project code name, geographic location, may be used as key words but will be followed by an indication of technical context. The assignment of links, roles, and weights is optional.